MICROBOONE-NOTE-1100-PUB

MEASUREMENT OF CHARGED-CURRENT ν_μ AND ν_e INTERACTIONS TOWARDS A SEARCH FOR LOW ENERGY ν_E EVENTS USING WIRE-CELL IN MICROBOONE

The MicroBooNE collaboration
microboone_info@fnal.gov

August 13, 2021

Abstract

This technote summarizes the existing work in searching for ν_e low-energy excess (eLEE) in MicroBooNE Booster Neutrino Beam (BNB) data stream based on the Wire-Cell event reconstruction paradigm. The charged-current ν_μ and ν_e events are selected from the 5.3e19 POT open data from the BNB beam, 6.37e20 POT far sideband from the BNB beam data, and 2.10e20 POT data from Neutrinos at the Main Injector (NuMI) beam. The charged-current ν_e selection results from the BNB data that are sensitive to the eLEE search are not included. Various comparisons between data and Monte Carlo predictions are performed to validate the overall model and demonstrate the power of the analysis techniques. Physics sensitivities in terms of the exclusion and the discovery potential are presented.

Contents

1 Introduction **3**

2 Wire-Cell Pattern Recognition **6**
2.1 Neutrino Energy Reconstruction 8

3 Charged-Current ν_μ Selection **12**
3.1 Charged-Current/Neutral-Current π^0 Selection 15

4 Charged-Current ν_e Event Selection **16**

5 Systematic Uncertainties **22**

6 Analysis of BNB Open Data at 5.3e19 POT **26**

7 Analysis of NuMI Data at 2.10e20 POT **36**

8 Analysis of BNB Far sideband Data at 6.37e20 POT **42**
8.1 Validation of π^0 mass reconstruction 43
8.2 Validation of reconstruction of neutrino vertex 44
8.3 Validation of ν_μCC muon kinematics distributions 45
8.3.1 Validation of ν_eCC far sideband event selection 47
8.4 ν_μCC 0p Np separation 49
8.4.1 Validation of the Overall Model with Goodness-of-Fit Tests 56
8.5 Validations of neutrino energy reconstruction 60

9 eLEE Sensitivities **71**

10 Summary **72**

A Glossary of various final states **72**

1 INTRODUCTION

This technote summarizes some foundational work for a low-energy ν_e excess (eLEE) in MicroBooNE [1] using the Wire-Cell event reconstruction paradigm. The starting point of this analysis is the generic neutrino detection [2, 3, 4], in which the cosmic-ray backgrounds are largely rejected resulting an overall contamination level below 15%. After the generic neutrino selection, the efficiencies for selecting charged-current ν_μ (ν_μCC) and ν_e (ν_eCC) events are about 80% and 90%, respectively. The signal-to-background ratios for ν_μCC and ν_eCC are about 2:1 and 1:190, respectively, and are further improved with the techniques described in this technote. The event selections in this analysis are designed to be as general as possible (i.e. inclusive ν_eCC and ν_μCC event selections), so that more freedom is available at later stages of the analysis if an excess is observed.

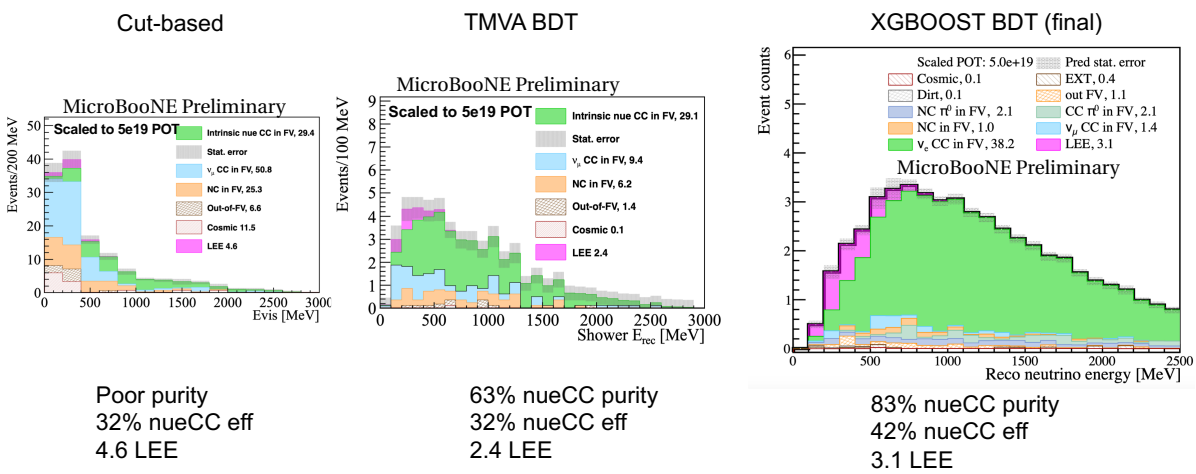

Figure 1: Evolution of the ν_eCC event selection from human learning/engineering to machine learning. The combination of generic features selected by human engineering and high statistics simulation events evaluated by the machine learning yields a robust and high-performance ν_eCC event selection.

As shown in Fig. 1, the development of the ν_eCC event selection (or tagger) naturally follows a transition from human learning/engineering to machine learning. During the human learning stage, hand scan techniques are used to identify generic features that can be used to perform event selection. The features are intended to be robust against the detailed simulation/data differences. Although the hand scan is efficient in selecting generic features, it is clearly limited by the capacity of a human being. For example, a person can generally study only about 20 events in details per day. While this capability is enough for a task with a reasonable initial signal-to-background ratio (i.e. ν_μCC at 2:1), it is not sufficient for a task with a poor initial signal-to-background ratio (i.e. ν_eCC at 1:190). For the latter, machine

learning techniques are necessary, since hundreds of thousands of simulated events can be studied by a computer at once. In particular, we use a boosted decision tree (BDT) trained on the generic features that were engineered by the hand scan to maximize the efficiency and purity of final ν_eCC and ν_μCC event selections. A purity of 83% (93%) and an efficiency of 42% (64%) are achieved for ν_eCC (ν_μCC) event selection. Together with the evolution of ν_eCC event selection, the energy reconstruction also evolves from the visible energy to the EM shower energy, and then to the reconstructed neutrino energy, which has the best resolution and capability to distinguish signal and background events.

Test Statistics based on Covariance Matrix

$$\chi^2 = (M-P)^T \, Cov(M,P)^{-1} \, (M-P)$$

M: measurement vector
P: prediction vector

	Nested Likelihood Ratio	Simple-vs-simple Likelihood ratio	Goodness-of-fit
Test statistics	$\Delta\chi^2_{nested} = \chi^2(x=x_0) - \chi^2_{\min}(x_{\min})$	$\Delta\chi^2_{nested} = \chi^2_{SM} - \chi^2_{LEEx=1}$	χ^2_{SM}
Chi-square	CNP	CNP	Pearson
Motivation	Rejection/compatibility of the null hypothesis, construction of confidence interval	Compatibility of the null hypothesis, rejection of new-physics hypothesis	Compatibility of the null hypothesis
Special features	Non-negative x, Feldman-Cousins approach	Frequentist approach for p-value calculation	Conditional covariance matrix for selected channels

CNP: Combine-Neyman-Pearson Chisquare, NIMA 961, P163677
Feldman-Cousins: Phys.Rev.D57:3873-3889
Conditional Covariance Matrix: Eaton, Morris L. (1983)

Figure 2: Summary of test statistics used in this analysis.

The search for an LEE signal is equivalent to testing the null hypothesis defined as the Standard Model (SM) prediction without an LEE signal. The SM prediction is formed based on state-of-art understanding of the Booster Neutrino Beam flux [5], the neutrino-argon interaction cross section [6], detector simulation [7, 8, 9], and signal processing [7, 10, 11, 12]. The alternative hypothesis is formed based on a model of a potential anomalous enhancement in the rate of intrinsic ν_eCC events at true neutrino energies less than 800 MeV with a fixed spectral shape. The model is obtained by unfolding the observed excess of electron-like events in MiniBooNE [13] to true neutrino energy under a charged-current quasi-elastic (CCQE) hypothesis and applying that prediction directly to the rate of intrinsic ν_eCC events expected in MicroBooNE [14]. In the alternative hypothesis, we allow the normalization of this low energy excess model to float and define a signal strength parameter x, such that $x = 0$ corresponds to no anomalous enhancement in the expected rate of intrinsic ν_eCC events

(the SM case) and $x = 1$ corresponds to an anomalous enhancement in the expected rate of intrinsic ν_eCC events of equal magnitude to that obtained from the unfolded MiniBooNE measurement (or $eLEEx = 1$).

We fit this model to our data by minimizing a χ^2 test statistic that incorporates our knowledge of experimental uncertainties and their correlations into a covariance matrix and obtain a best fit value of $x = x_{min}$. We compute the $\Delta\chi^2_{nested}$ for our data for each value of the signal strength x, relative to this best fit point, and obtain frequentist confidence intervals for the signal strength x following the Feldman-Cousins unified approach [15]. This test is essentially a nested likelihood ratio (LR) hypothesis test. In addition to the primary nested LR test statistics ($\Delta\chi^2_{nested}$), several other test statistics are used to provide supplemental information. They are i) goodness-of-fit (GoF) based on a Pearson χ^2; and ii) a simple-vs-simple likelihood ratio test ($\Delta\chi^2_{simple} = \chi^2_{SM} - \chi^2_{eLEEx=1}$), which provides additional information regarding the tests against the null hypothesis. Figure 2 summarizes the various test statistics used in this analysis.

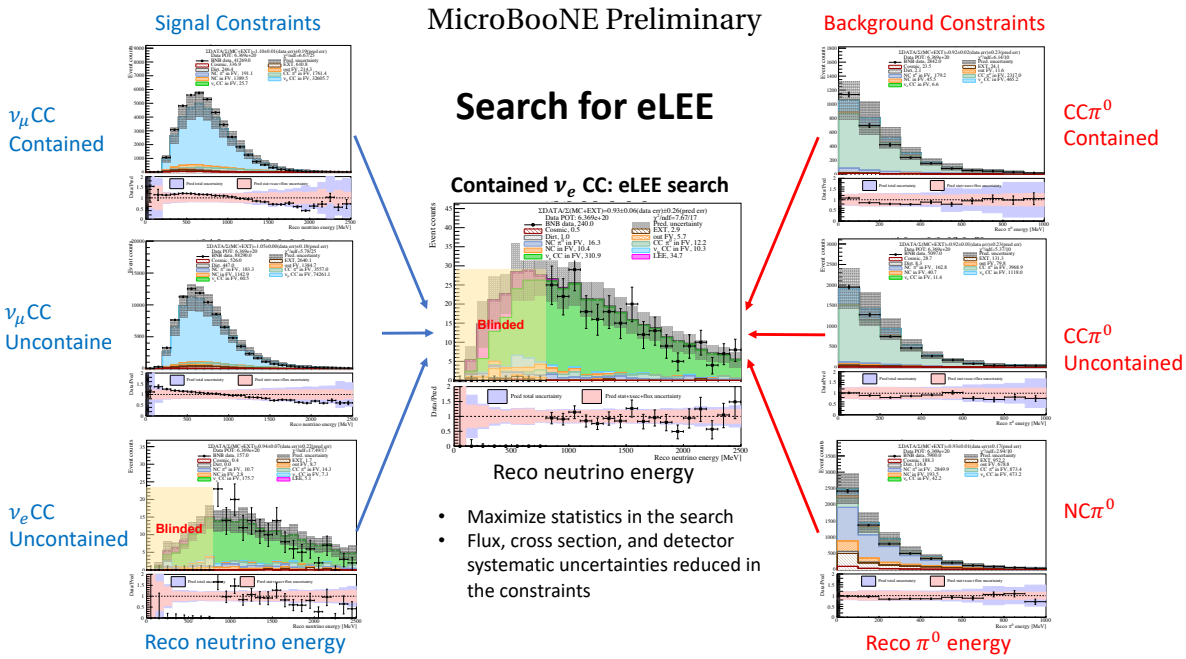

Figure 3: Illustration of the 7-channel fit in searching for eLEE. All plots can be found in Sec. 8. Data points for ν_e CC in the low energy region are not available.

To maximize the physics sensitivity of this search, a 7-channel fit strategy to both signal and constraint samples is adopted as shown in Fig. 3. The seven channels are i) fully contained (FC) ν_eCC, ii) partially contained (PC) ν_eCC, iii) fully contained ν_μCC, iv) partially contained ν_μCC, v) fully contained CCπ^0, vi) partially contained CCπ^0, and vii) NCπ^0. The primary

channel that is sensitive to the LEE search is the FC ν_eCC. Three channels — PC ν_eCC, FC ν_μCC, and PC ν_μCC — are used to provide constraints to the signal prediction using MicroBooNE data (e.g. neutrino flux, cross section, and detector systematics). The other three channels — FC CCπ^0, PC CCπ^0, and NCπ^0 — are used to improve the background prediction using MicroBooNE data, since π^0's are one of the backgrounds of ν_eCC events. To ensure these seven channels are statistically independent, the event selections are designed to be exclusive from each other. For example, the CCπ^0 event selection excludes the ν_eCC candidates. Similarly, the ν_μCC event selection excludes ν_eCC and CCπ^0 candidates. In the 7-channel selection plots shown in this note, the categories "ν_μCC" and "NC" exclude ν_eCC and π^0 events.

In this analysis, we consider the various sources of systematic uncertainties from i) neutrino flux of the Booster Neutrino Beam, ii) the neutrino-argon interaction model based on the GENIE event generator, iii) detector performance, iv) finite statistics from Monte Carlo simulation, and v) additional uncertainties associated with background sources originating outside the detector volume. Different sources of systematic uncertainties have different impacts on the predicted event distributions. The systematic uncertainties associated with the neutrino flux would change the distribution of events by providing different weights for events with different true neutrino energy and flavor. The systematic uncertainties of cross section and detector performance can impact the efficiency (for both signal and background) as well as the reconstruction of kinematic variables. The uncertainty because of the limited statistics of Monte Carlo simulation is particularly important for rare event searches (e.g. ν_eCC). Additional uncertainties are necessary for estimating systematics for the background contributions from neutrino interactions originating outside the cryostat (subsequently referred to as DIRT events).

2 Wire-Cell Pattern Recognition

This section summarizes the development of the pattern recognition techniques in Wire-Cell, which are the foundation of the high-performance ν_eCC and ν_μCC event selections. Some of the basic tools—the track trajectory and dQ/dx fitting used to reject stopped muons, for example—are improved versions of techniques developed for the generic neutrino detection [16]. This fitting algorithm was expanded to fit multiple tracks with vertices connecting them rather than fitting a single track. Figure 4 shows the overall flow of the Wire-Cell pattern recognition. We summarize the pattern recognition strategy briefly here. First, vertices are defined by searching for kinks and splits in the reconstructed 3D images. With vertices

determined, segments between vertices are defined. A 3D vertex fitting technique is then used to refine the position of the 3D event vertex. Particle identification (PID) is subsequently performed on segments using dQ/dx and event topology information. Event topology information is primarily targeted toward electromagnetic (EM) shower identification (i.e. track/shower separation). Using particle identification information, the direction of the particles can be determined in many cases, which is very useful in determining the primary neutrino interaction vertex. In parallel, we also use deep learning techniques to determine the primary neutrino vertex. With the neutrino interaction vertex reconstructed, one can then fully cluster EM showers, which often encompass several separated sub-clusters. Finally, one can reconstruct π^0s from EM showers.

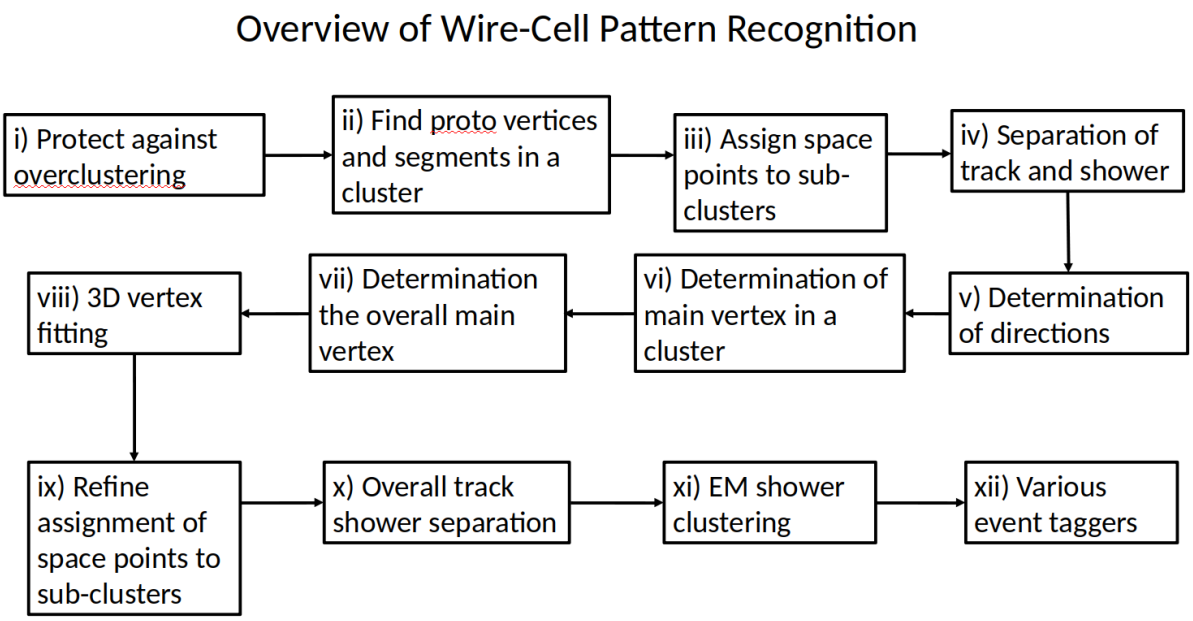

Figure 4: Overview of the Wire-Cell pattern recognition procedure. More details can be found in the text.

Figure 5 illustrates the results of the pattern recognition at different stages. dQ/dx information is especially important for particle identification and determining the direction of the particle trajectory. The current labels (e^-, μ^-, π^+) are only temporary and include their respective counterparts (e^+, μ^+, π^-) as well. In the event shown in Fig. 5, the EM shower connecting to the primary proton is produced by a gamma instead of by an electron with high dQ/dx at the beginning of the EM shower. However, it is still displayed as an electron as a proxy for EM showers before a detailed e/gamma separation.

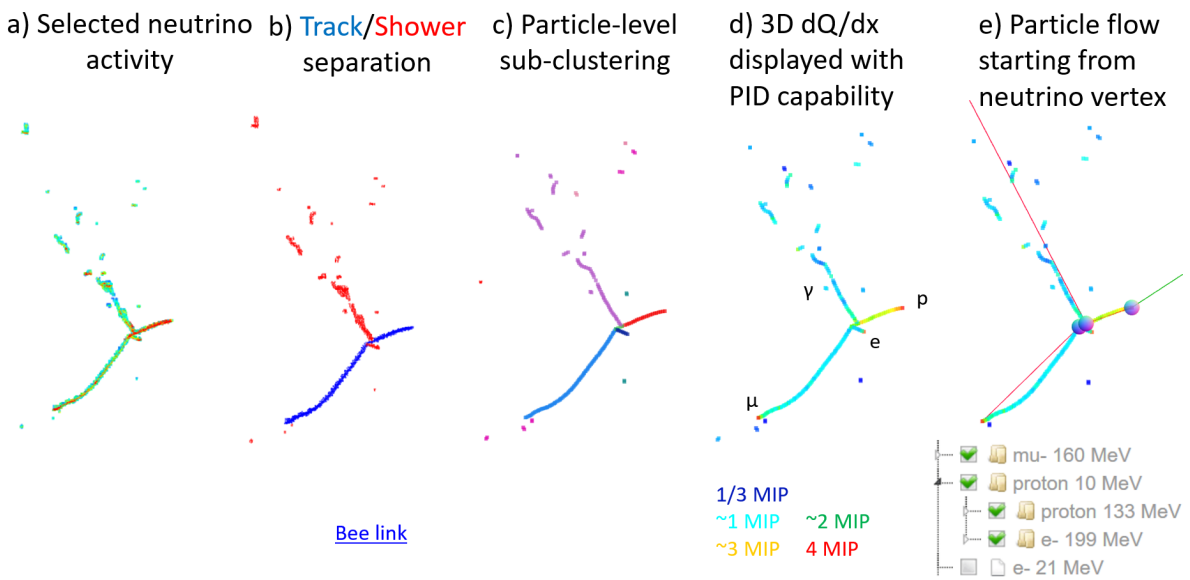

Figure 5: Results of the Wire-Cell pattern recognition are displayed at different stages. The candidate neutrino activity selected by the generic neutrino detection step is shown in Fig. 5a, in which the color represents the reconstructed charge in 3D. The identified tracks and EM shower are displayed in blue and red, respectively, in Fig. 5b. The different identified particles (or segments) are displayed in different colors in Fig. 5c. The determined 3D dQ/dx information with the multi-track trajectory and dQ/dx fitting algorithm is shown in Fig. 5d. The blue, cyan, green, yellow, and red colors roughly represent 1/3, 1, 2, 3, and 4 times of dQ/dx of a minimal ionizing particle (MIP), respectively. Finally, the particle flow information starting from the determined primary neutrino interaction vertex is shown in Fig. 5e. The original BEE weblink is `https://www.phy.bnl.gov/twister/bee/set/uboone/reco/2021-01/pr-1/event/3/`.

2.1 Neutrino Energy Reconstruction

For the eLEE search, the reconstruction of neutrino energy is particularly important. Three methods are used to calculate the energy of the reconstructed particles:

- Range: the travel range of a track-like object can be used to calculate the energy of the particle if it stops inside detector. The NIST PSTAR database [17] is used to derive the relation between the range and the kinetic energy of each particle type (different particle mass).

- dQ/dx corrected by the recombination effect: the ionization charge per unit length dQ/dx is connected to the energy loss per unit length dE/dx through the recombination model. Therefore, by performing a charge recombination correction, we can convert the measured dQ/dx to dE/dx, which can be used to derive the energy of the particle. We use the recombination model published in Ref. [9] to perform such

a correction. This method can be used for both stopped particles as well as particles exiting the detector.

- Charge scaling: while the above two methods are reliable for estimating the energy of track-like objects, they are not suitable for EM showers because of the difficulties in deriving dQ/dx or range. For EM showers, the energy is estimated calorimetrically by scaling the total charge information: $Q/0.4$. This factor is derived from MC study including the bias in the reconstructed charge [18] and the average recombination factor (≈0.5) of an EM shower.

For a stopped track longer than 4 cm, range is used to estimate energy. For short stopped tracks (< 4 cm), the dQ/dx with recombination correction is used to estimate energy. For EM showers, charge scaling is used to estimate energy. In addition, an average 8.6 MeV binding energy is added for each identified proton in the reconstructed particle flow. These protons may be produced at the primary neutrino interaction or via secondary interactions (e.g. produced by a neutron). For each muon, charged pion, or electron, its mass is added to the energy reconstruction. Fig. 6 illustrates the performance of the neutrino energy reconstruction. The reconstructed neutrino energy resolution is 10%-15% for ν_eCC events across the entire energy region. Typically, the reconstructed neutrino energy resolution is 15% at a true mean neutrino energy of 800 MeV. In comparison, the reconstructed EM shower energy resolutions are 14%, 13%, 12% for true EM shower energies of 200 MeV, 400 MeV, and 800 MeV, respectively.

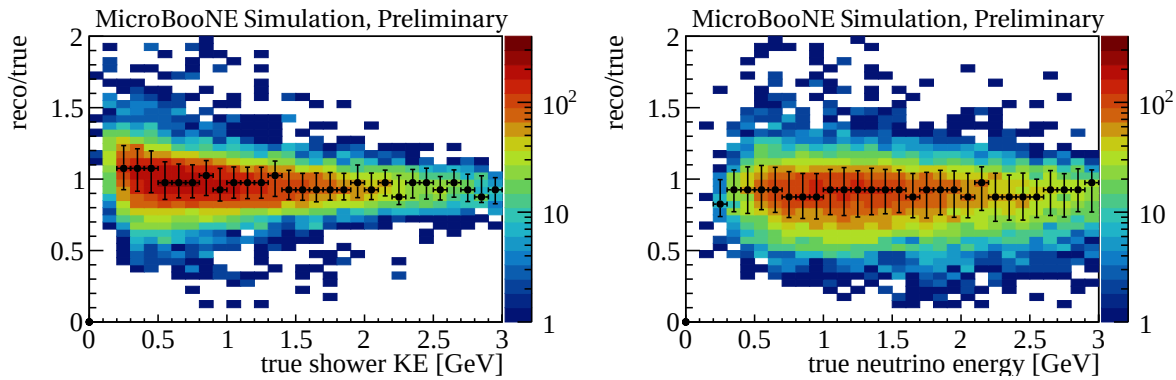

Figure 6: Ratio of reconstructed shower or neutrino energy to truth for fully contained ν_e CC candidates with actual BDT selection (Sec. 4). The peak values and the corresponding resolutions (asymmetric, 68.27% quantile from the peak value on either side) for each true energy bin are plotted as well. Overall, the energy resolutions of reconstructed shower and neutrino reco energies are about 12% and 15%, respectively.

Dedicated studied are carried out to validate the reconstruction of neutrino energy. The dQ/dx with recombination correction method is validated by comparing the dQ/dx vs.

residual range for the stopped muons and protons between data and Monte Carlo (see Fig. 33). The energy reconstruction of EM showers is validated by comparing the reconstructed π^0 mass between data and Monte Carlo (see Fig. 34). The accuracy of the reconstructed neutrino energy also depends on the the modeling of the neutrino-argon interaction, which is validated in Sec. 8.5. In addition to the reconstructed neutrino energy (E_ν^{rec}), we also introduce a few useful intermediate kinematics variables:

- E_μ^{rec}: total reconstructed energy of the primary muon including the muon mass. The reconstruction of this energy is based on the reconstructed kinetic energy of the muon K_μ^{rec}. E_μ^{rec} is directly linked to the true muon energy E_μ.
- θ_μ^{rec}: reconstructed polar angle of the primary muon with respect to the incident neutrino beam direction. θ_μ^{rec} is derived from the reconstructed direction of the primary muon. This variable is directly linked to the true muon polar angle θ_μ.
- E_{had}^{rec}: total reconstructed energy of the hadronic energy system, which is essentially the difference between E_ν^{rec} and E_μ^{rec}. This variable is linked to the energy transfer to the Argon system $\nu = E_\nu - E_\mu$.

These definitions are crucial to validate the reconstruction of neutrino energy in Sec. 8.5.

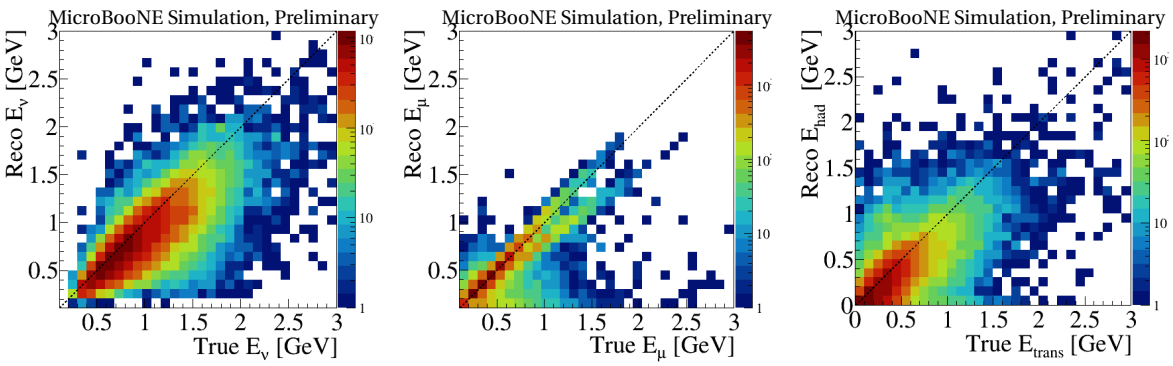

Figure 7: Fully contained ν_μCC candidates: (left) true neutrino energy vs. reconstructed neutrino energy, (middle) true muon energy vs. reconstructed muon energy, (right) true transferred energy to the Ar system vs. reconstructed hadronic energy.

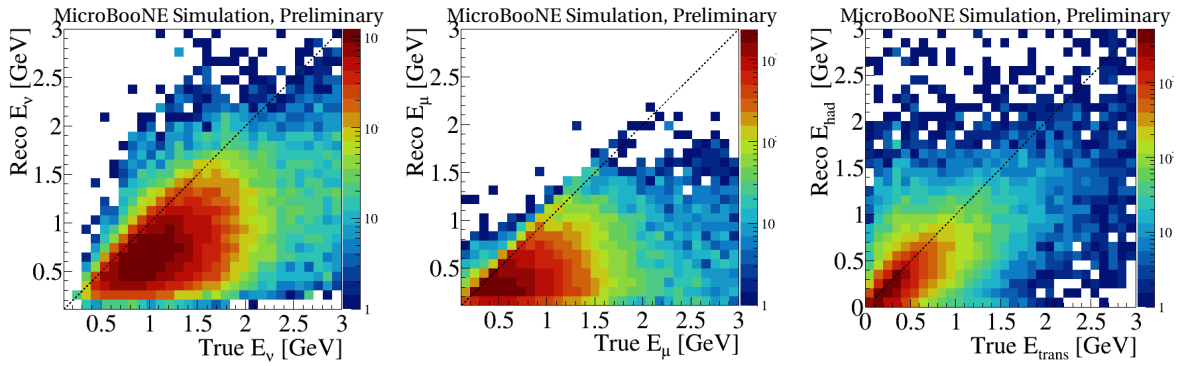

Figure 8: Similar as in Fig. 7 but is for partially contained candidates. The reconstructed energy for the partially contained events are typically underestimated.

Figure 7 shows the reconstruction performance for various energies for the FC ν_μCC candidates. Long muons are vulnerable to delta-ray radiation and multiple scattering, and therefore, are more easily to be broken and segmented into several clusters in the pattern recognition, in which we estimate muon energy with a dedicated recombination model. However, this model predicts 20% less energy than that measured in both data and MC. As a result, a bias in the reconstructed muon energy can be observed, as shown in Figure 7 (middle). This can be improved in the next round of data production. Figure 9 shows the corresponding bias and resolution below 3 GeV. Figure 8 and Fig. 10 show the similar results for PC ν_μCC candidates. The overall resolution for the reconstructed neutrino energy for the ν_μCC selection is about 20%.

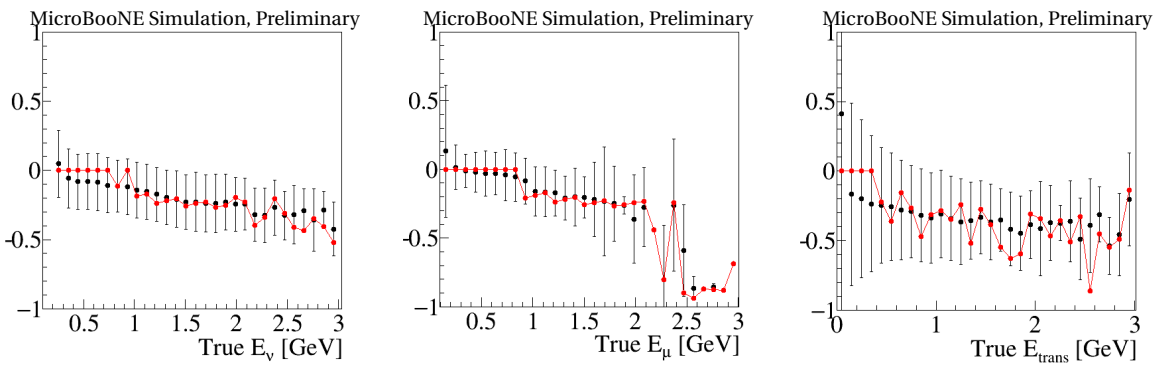

Figure 9: Fully contained ν_μCC candidates: relative bias of the reconstructed energy below 3 GeV for (left) neutrino energy, (middle) muon energy and (right) hadronic energy. The black points indicate the relative bias derived from the 50% quantile, and the associated error bars is combined from the 16% and 84% quantiles. The red points are the relative biases independently calculated from the maximum bin of the reconstructed energy distribution, and is used as a cross check. The two metrics for bias are mostly consistent.

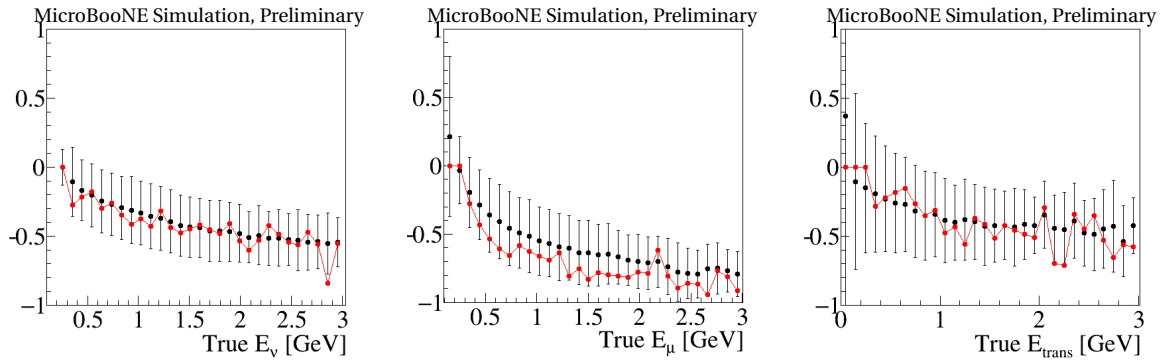

Figure 10: Similar as in Fig. 9 but is for partially contained candidates.

3 Charged-Current ν_μ Selection

When performing a ν_μCC event selection in MicroBooNE, a surface-operating LArTPC, the primary challenge is the removal of cosmic-ray muons. Wire-Cell generic neutrino detection [16, 2, 3, 4] does a significant portion of the work to remove cosmic background events. Figure 11a shows the result after generic neutrino detection, of which ~65% are ν_μCC events with an efficiency of roughly 80%. Cosmic-ray muons are reduced to below 15% of the remaining events. With additional pattern recognition techniques developed in Wire-Cell, an improved ν_μCC selection with a purity of ~90% and efficiency of ~65% are achieved (see Fig. 11b) by further rejecting neutral-current events through requiring a reconstructed muon to be longer than 5 cm and removing the residual cosmic-muon backgrounds. Figure 12 shows various residual backgrounds entering the detector from outside. Figure 13 shows example mistakes where a muon is misidentified as a charged pion. In Fig. 13a, the muon was misidentified because of the overlap with an EM shower. In Fig. 13b, the muon has several large-angle scatterings. Figure 14 shows examples where NC events are misidentified as ν_μCC interactions. In both cases, a charged pion behaves like a muon (e.g. no rescattering).

We further developed a ν_μCC event selection based on the modern Boosted Decision Tree (BDT) library: XGBoost [19]. Along with other improvements in vertex finding and energy reconstruction, ~93% purity and ~64% efficiency were achieved. Figure 15 shows the final BDT ν_μCC selections, scaled to 5E19 POT, for fully contained and partially contained samples. Figure 16 shows the selection efficiency for ν_μCC interactions in the active TPC volume as functions of true neutrino energy (E_ν), true muon energy (E_μ), and true transferred energy to the argon nucleus ($E_\nu - E_\mu$), respectively.

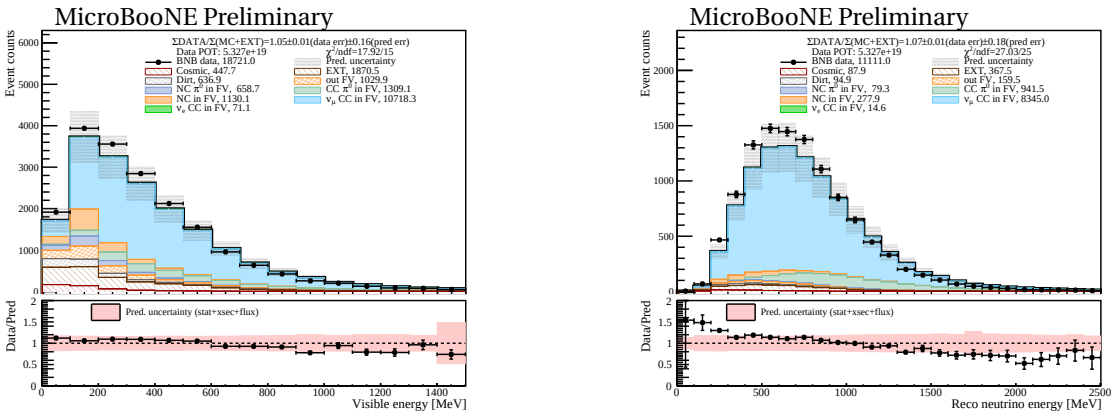

(a) **(b)**

Figure 11: Cut-based ν_μCC selection. The left panel shows the result after generic neutrino detection where ~ 2/3 of the events are already ν_μCC with an efficiency of about 80%. The right panel shows the cut-based ν_μCC selection where 90% of the events are ν_μCC with an efficiency of about 65%.

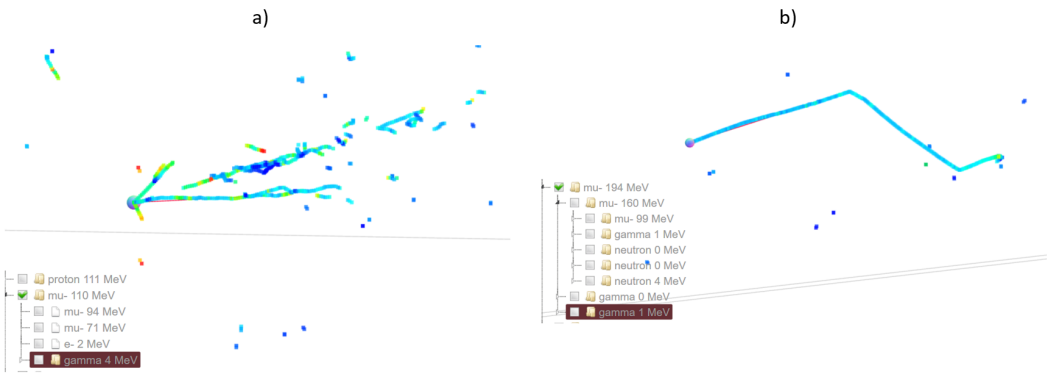

Figure 13: ν_μCC events misidentified as NC backgrounds. (Left) the charged muon is misidentified as a charged pion because of its overlap with an EM shower. (Right) the charged muon is misidentified as a charged pion because of several large-angle deflections. The grey box represents the MicroBooNE active TPC volume, which is 2.56 m in the drift direction (X), 2.3 m high (Y), and 10.56 m along the beam axis (Z).

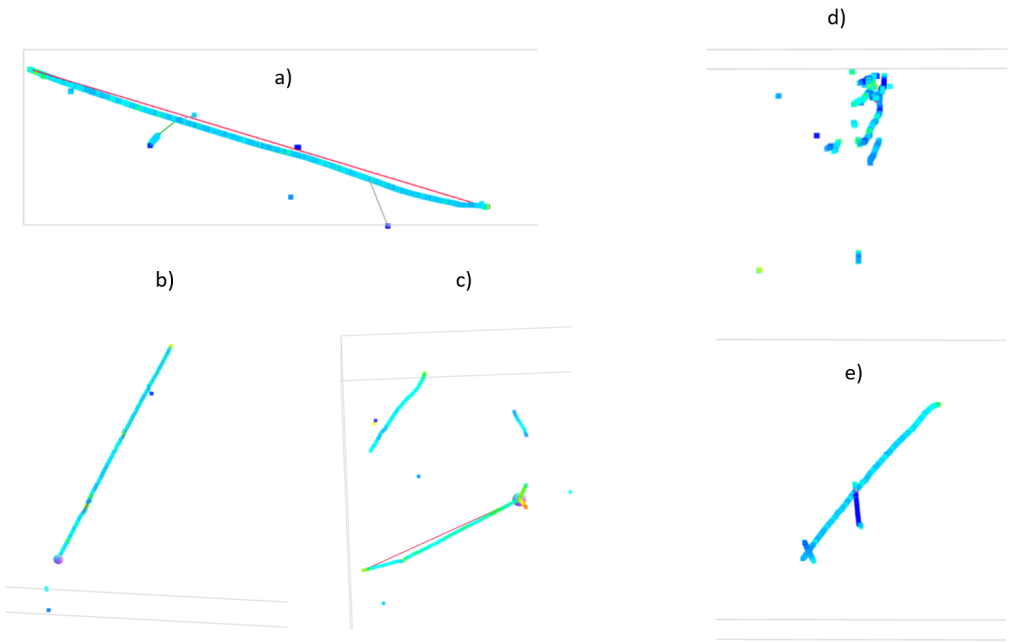

Figure 12: Various backgrounds for the ν_μCC selection (both comsic and neutrino-induced) originating from outside the detector fiducial volume: a) reconstructed neutrino vertex is outside the fiducial volume; b) a single muon with an incorrect matched light signal, which can be confused as a single muon going out of the detector; c) part of a neutrino interaction going into the detector from the upstream; d) only part of a EM shower can be seen at the top of the detector; e) a single muon with some ghosts tracks (part of Michel electron identification). The grey box represents the MicroBooNE active TPC volume, which is 2.56 m in the drift direction (X), 2.3 m high (Y), and 10.56 m along the beam axis (Z).

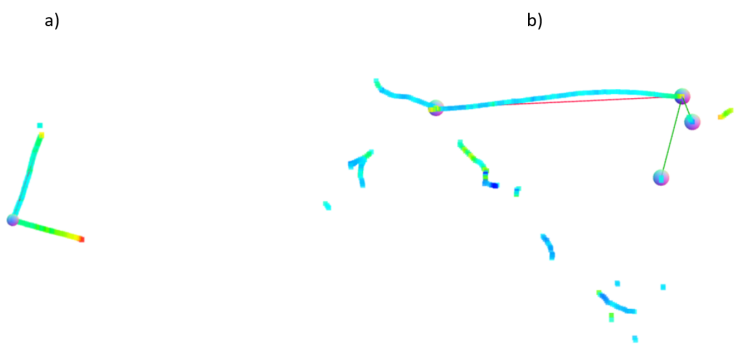

Figure 14: NC events misidentified as ν_μCC. In both cases, the charged pion behaves like a muon.

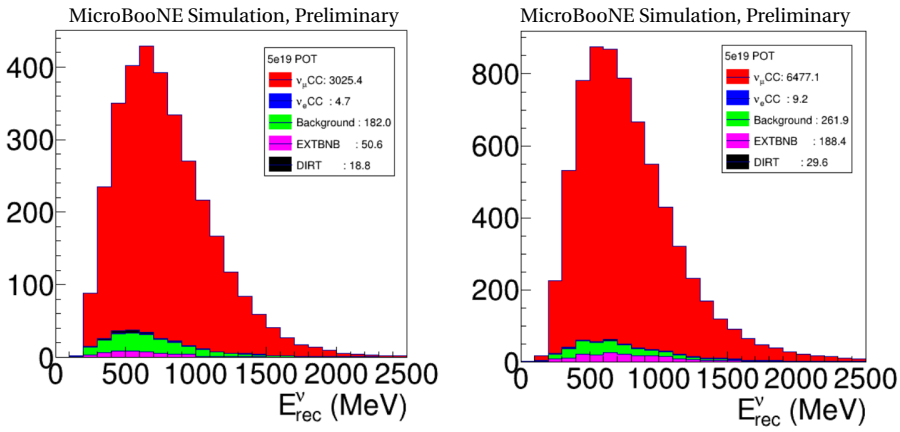

Figure 15: The final BDT ν_μCC selections, scaled to 5E19 POT, for fully contained and partially contained samples.

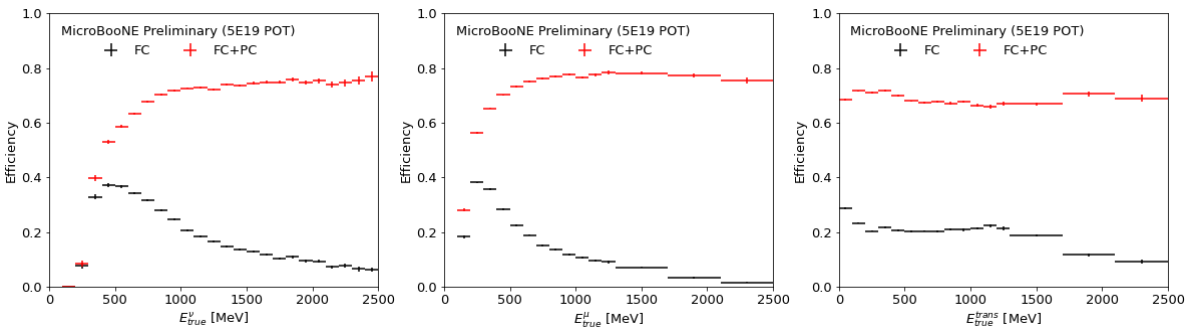

Figure 16: Efficiency of the ν_μCC selection in the active TPC volume as functions of true neutrino energy, true muon energy and true transferred energy to Ar, respectively. Both FC and FC+PC event selections are shown in the figures.

3.1 Charged-Current/Neutral-Current π^0 Selection

The charged-current ν_μ selection described above can be used to create a charged-current π^0 selection to be used as a data-driven constraint of the charged-current π^0 backgrounds to the ν_eCC event selection. Additionally, a neutral-current π^0 selection can be achieved by considering only events not selected by the charged-current ν_μ selection described above. The photon pair with the highest energies that point back to the same vertex are chosen for the reconstruction of the π^0. The primary π^0 is ensured by placing a distance cut between the neutrino vertex and π^0 vertex. Further selection cuts use the γ energies and distances from the neutrino vertex, as well as the angle between the two γ's, and the reconstructed π^0 invariant mass. The comparison between data and MC on the reconstructed π^0 mass can be found in Fig. 34.

4 CHARGED-CURRENT ν_e EVENT SELECTION

Compared to ν_μCC interactions, the selection of ν_eCC interactions is much more challenging. While the signal-to-background ratio of ν_μCC selection is approximately 2:1 after the generic neutrino detection [16], the signal-to-background ratio of ν_eCC selection is about 1:190. In the ν_μCC selection, the application of pattern recognition techniques enhances the signal-to-background ratio by a factor of 4.5, leading to 9:1. To reach a similar level, the background acceptance of ν_eCC is required to be at least below the 0.06% level. A tiny background leakage can be devastating for the ν_eCC selection.

The development of the ν_eCC selection happens in two stages. The first stage is the development of cut-based background taggers, which are again based on hand scans of background events. This effort suffers from the limited learning rate of a human being. About O(1000) events were examined in a two month time scale. Figure 1 (far left) shows the signal-to-background ratio after applying background tagger cuts. While the resulting signal-to-background ratio is not satisfactory, the main motivation of this work is to extract various features (i.e. variables) that can be used to reject backgrounds is achieved. The second stage of the development is to apply machine learning techniques, particularly BDTs with large statistics of Monte Carlo samples. Based on features (or variables) extracted during the first stage, a machine learning method based on BDTs is applied on large Monte Carlo events. The resulting ν_eCC selection is shown in Fig. 1 (far right).

The basic selection of inclusive ν_eCC events requires an EM shower with a reconstructed energy higher than ~60 MeV connecting to the primary neutrino vertex. The energy threshold is placed to exclude Michel electrons. When there are multiple reconstructed EM showers connecting to the neutrino vertex, the EM shower with the highest energy is passed to the background tagger for further examination. Background taggers were developed by extracting features from a hand-scan effort. Figure 17 shows the rejection matrix of these background taggers. There are roughly five groups of background taggers. The first group focuses on the primary electron identification, including the examination of dQ/dx at the beginning (stem) of the shower and the identification of a gap between the shower and the neutrino vertex. The second group focuses on cases with multiple EM showers (e.g. π^0). The third group focuses on cases of muon-related misidentification. The fourth group focuses on background rejection with kinematics information (e.g. energy comparison between electron candidate and muon candidate, energy and angle of electron candidate, etc.). The last group focuses on cases with unreliable pattern recognition. Note that there are multiple different failure modes leading to incorrect pattern recognition. Each failure mode would require a dedicated

background tagger.

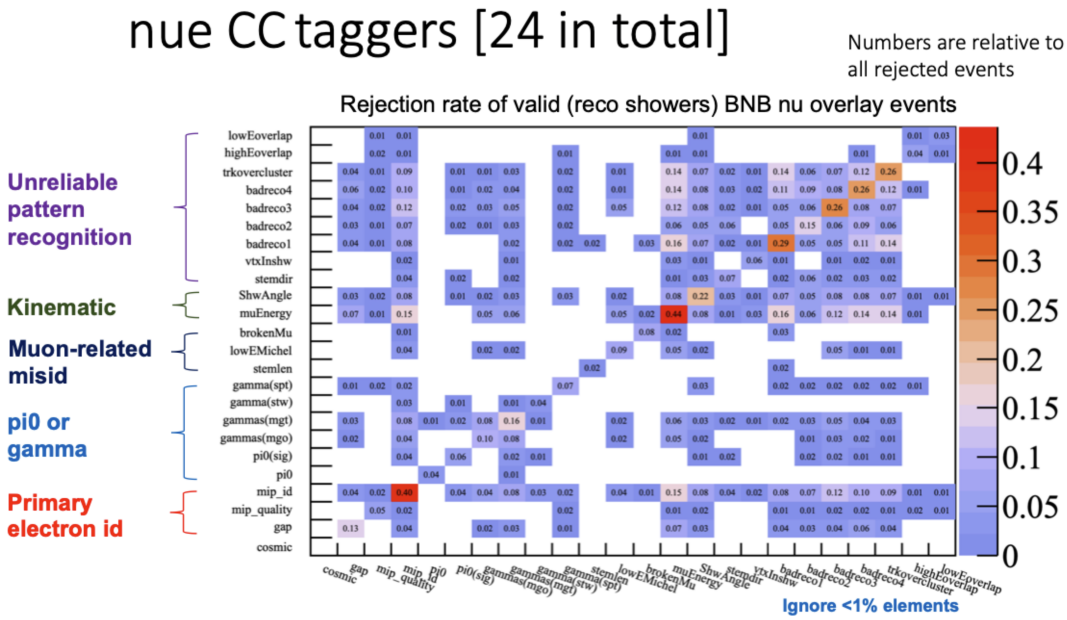

Figure 17: Rejection matrix of various background taggers. The diagonal term shows the amount of background events rejected by the selected background tagger. The off-diagonal term shows the amount of background events simultaneously rejected by two background taggers.

The primary electron identification includes:

- Gap cut: the beginning of the EM shower in each 2D projection view is examined to search for a gap. Figure 18 shows an example.
- MIP quality cut to remove backgrounds: the beginning of the shower is examined to ensure the quality of the shower stem. The checks include examinations of i) potential track overlap at the beginning of EM shower, ii) possible track splitting at the beginning of EM shower (i.e. the pair produced electron and positron are split instead of traveling in the same direction).
- MIP dQ/dx cut: we examine the dQ/dx at the beginning of the EM shower to ensure a MIP (electron-like) event. Instead of a likelihood approach, we calculate the length of the MIP-like track below a MIP threshold cut (i.e. 1.3 times of a MIP dQ/dx). The calculation of the length also considers the possibility of delta ray (i.e. a single sample with high dQ/dx). In addition, the high dQ/dx at the vertex must be taken into account. Figure 19 shows a signal and a background event.

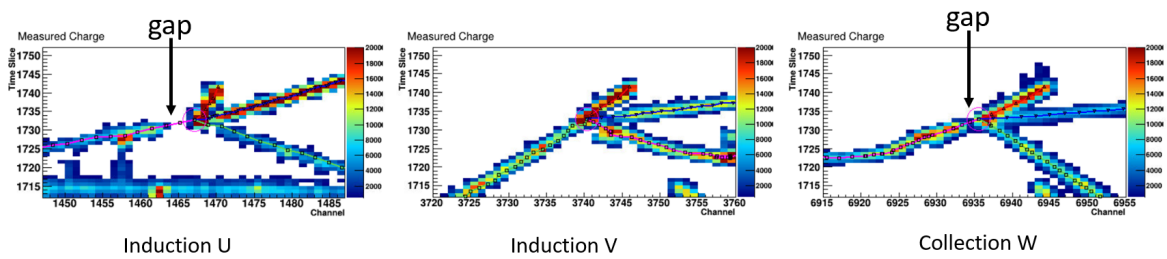

Figure 18: Illustration of gap identification for an EM shower. Magenta circle in the images indicates the neutrino vertex.

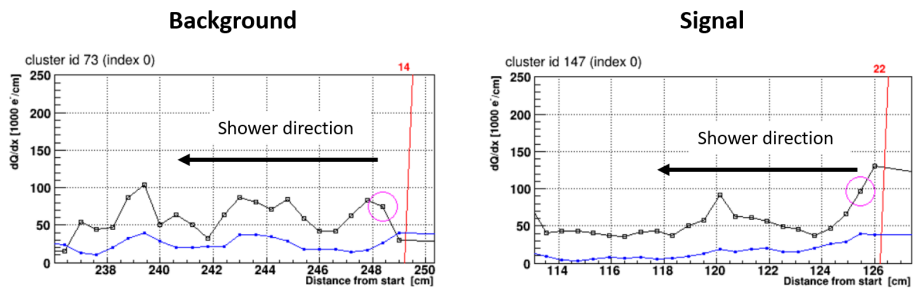

Figure 19: Illustration of MIP identification for EM showers. (Left) A background event. The MIP dQ/dx is expected to be around 45k electrons/cm. (Right) A signal event with a high dQ/dx at the neutrino interaction vertex. The blue lines give a measure of the fit quality. The red line with a number is used to separate the different track segments. The identified neutrino vertices happen to be at larger distance from the start for these two examples.

Figure 20 shows examples of gamma backgrounds from π^0 decay. Figure 21 shows examples of muon-related backgrounds. Figure 22 shows examples of backgrounds that can be rejected by kinematic information. Figure 23 and Fig. 24 shows the examples of backgrounds because of unreliable pattern recognition.

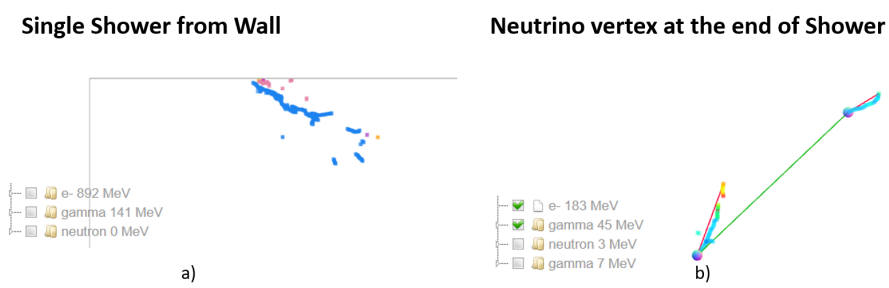

Figure 20: Illustration of single EM showers. (Left) An EM shower close to the top of the detector. (Right) The neutrino vertex is misidentified to be at the end of EM shower. The grey box represents the MicroBooNE active TPC volume, which is 2.56 m in the drift direction (X), 2.3 m high (Y), and 10.56 m along the beam axis (Z).

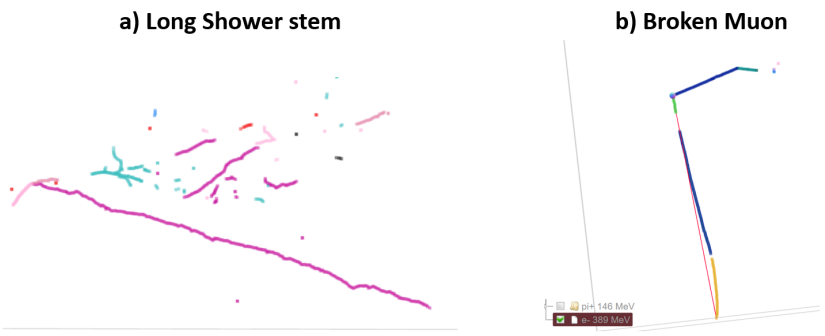

Figure 21: (Left) The identified EM shower has a long stem, which indicates an over-clustering situation (e.g. with a muon). (Right) A long muon is broken into pieces, which leads to a misidentification. The grey box represents the MicroBooNE active TPC volume, which is 2.56 m in the drift direction (X), 2.3 m high (Y), and 10.56 m along the beam axis (Z).

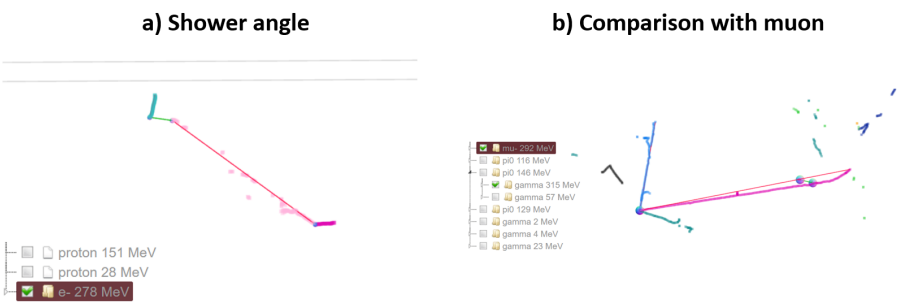

Figure 22: (Left) An EM shower going backward with respect to the neutrino beam direction. (Right) A long muon is found in addition to the electron candidate. The grey box represents the MicroBooNE active TPC volume, which is 2.56 m in the drift direction (X), 2.3 m high (Y), and 10.56 m along the beam axis (Z).

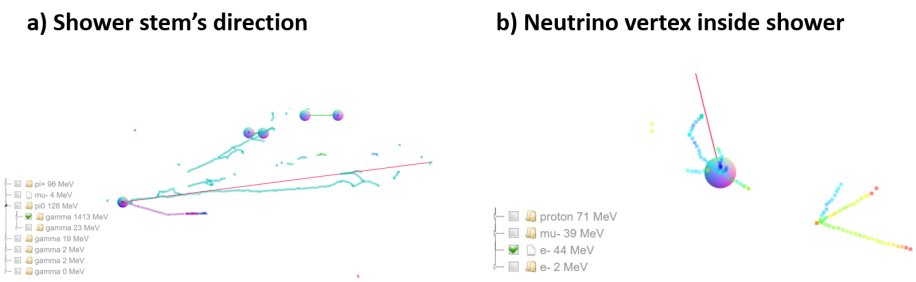

Figure 23: (Left) An example event where the shower stem's direction is not consistent with the shower's direction indicating an overclustering situation. (Right) The neutrino vertex is identified inside an EM shower.

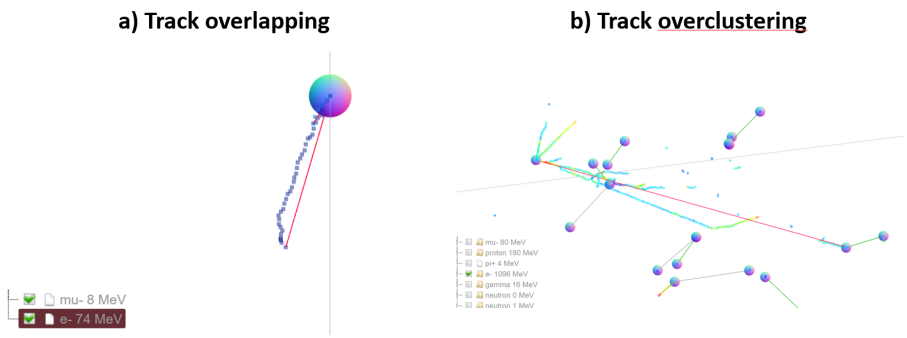

Figure 24: (Left) An overlapping situation at the beginning of EM shower's stem region. (Right) An example of track overclustering situation. One of the tracks clearly shows the Bragg's peak. The grey box represents the MicroBooNE active TPC volume, which is 2.56 m in the drift direction (X), 2.3 m high (Y), and 10.56 m along the beam axis (Z).

With the human-engineered features selected, we apply BDT techniques to high-statistics Monte Carlo simulation samples to finalize the ν_eCC selection. The usage of machine learning techniques mitigates the limitation of human learning when processing a large amount of events. From among different machine learning tools, the BDT technique is chosen because it is more robust and approachable for general users. The BDT package XGBoost [19], which provides fast and robust training through a parallel tree boosting, is used. XGBoost also improves the model generalization and overcomes the issues of overfitting in gradient boosting, enabling the use of a large pool of variables in the model.

This BDT model achieves 83% ν_eCC purity (without LEE) and 42% efficiency combining both fully contained and partially contained events. Scaled to 5E+19 POT, we expect 39 ν_eCC events and 3.1 LEE events ($eLEEx = 1$ hypothesis). The selected LEE signals are mostly fully contained ν_eCC events with energy less than 800 MeV. Figure 25 shows the energy spectra for fully contained events and partially contained events. The 200 - 300 MeV peak in the partially contained figure is understood and due to a ν_μCC event with a large GENIE weight (8.9).

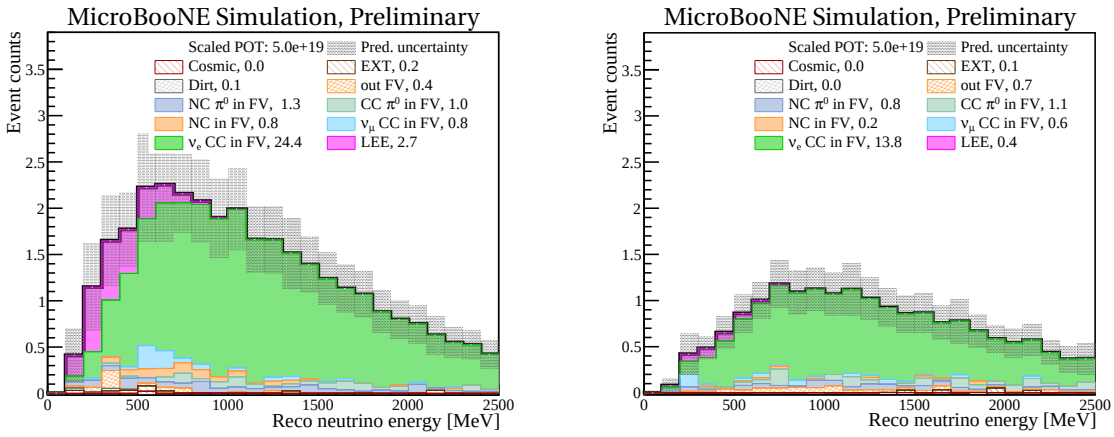

Figure 25: ν_eCC BDT selection at 5e19 POT. Left: fully contained events. Right: partially contained events. The gray area represents the total uncertainty of Monte-Carlo prediction, which includes statistical, cross section, and flux uncertainties (see Sec. 5).

The efficiency and purity for fully contained intrinsic ν_eCC and LEE events are shown in Fig. 26. For fully contained ν_eCC events, the overall selection efficiency and purity of intrinsic ν_eCC (without LEE) events are 26% and 84%, respectively. The efficiency of LEE signals is about 17%.

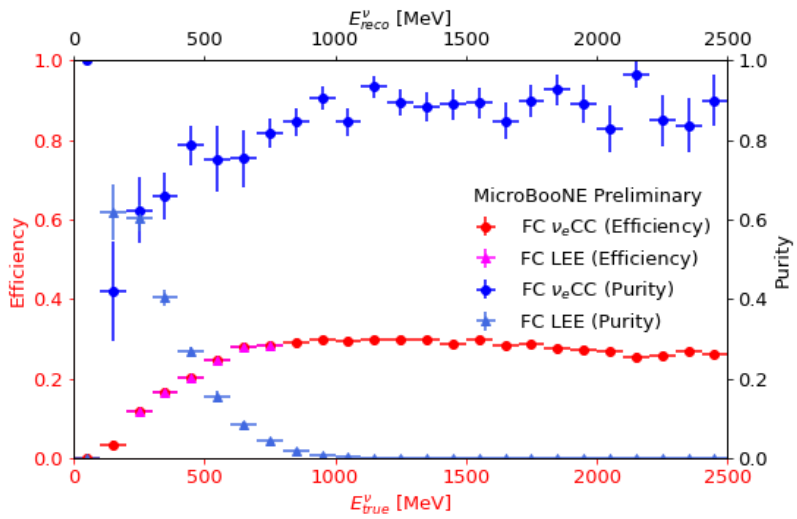

Figure 26: Efficiency and purity of selected fully contained ν_eCC events. Efficiency is calculated as a function of true neutrino energy. Purity is calculated as a function of reconstructed neutrino energy. "ν_eCC" and "LEE" have identical efficiencies in the LEE region. "ν_eCC" purity does not consider "LEE" signals, while "LEE" purity considers 'ν_eCC" events intrinsic in the beam as background.

5 SYSTEMATIC UNCERTAINTIES

There are in total five sources of systematic uncertainties considered in this analysis. This list includes uncertainties due to i) Monte Carlo statistics, ii) the neutrino flux, iii) neutrino-argon interactions, iv) detector effects, and v) backgrounds originating from outside the cryostat.

The estimation of uncertainties due to Monte Carlo statistics is performed based on a Bayesian approach [20]. The details regarding the model of neutrino flux and neutrino-argon interaction cross sections (Xs) can be found in Ref. [5] and Ref. [6], respectively. The details on MicroBooNE's approach to estimate the detector systematic uncertainties can be found in Ref. [21]. These uncertainties impact the event distribution through both the normalization of distributions and the reconstruction of kinematic variables.

The associated uncertainties of flux [22] and Xs [23] (i.e. the covariance matrices) are estimated using the common event-by-event reweighting tools. Two additional tuning parameters focusing the second-class currents that contribute to ν_e/ν_μCC cross section differences are added (Xs). The uncertainty associated with the beam flux (flux) is based on previous work in MiniBooNE [24]. Additional sources of uncertainties related to hadrons interacting with argon nuclei while in transit through the detector are estimated by varying re-interaction cross sections in GEANT4 [25].

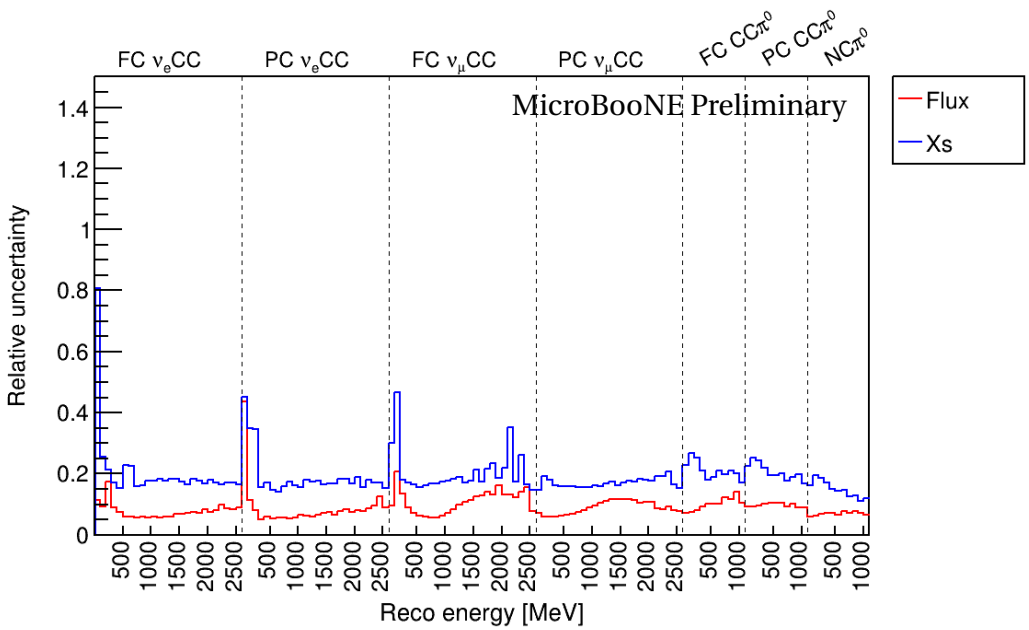

Figure 27: Relative uncertainties ($\frac{\text{absolute error}}{\text{central value}}$) of flux and cross section systematics for the seven channels as a function of reconstructed neutrino energy.

Figure 27 shows the relative uncertainties of flux and cross section systematics for the

seven channels. The information regarding the binning can be found in Sec. 6. The spikes of the cross section systematics are because of the low statistics, particularly of background, in the simulation. Left panel of Fig. 28 shows the correlations of flux systematics for the seven channels. There are strong correlations between i) ν_e low energy range and ν_μ low energy range, ii) ν_e high energy range and ν_μ high energy range, iii) ν_e high energy range and π^0s entire energy range. Right panel of Fig. 28 shows the correlations of cross section systematics for the seven channels. There are strong correlations between ν_e and ν_μ in the entire energy range.

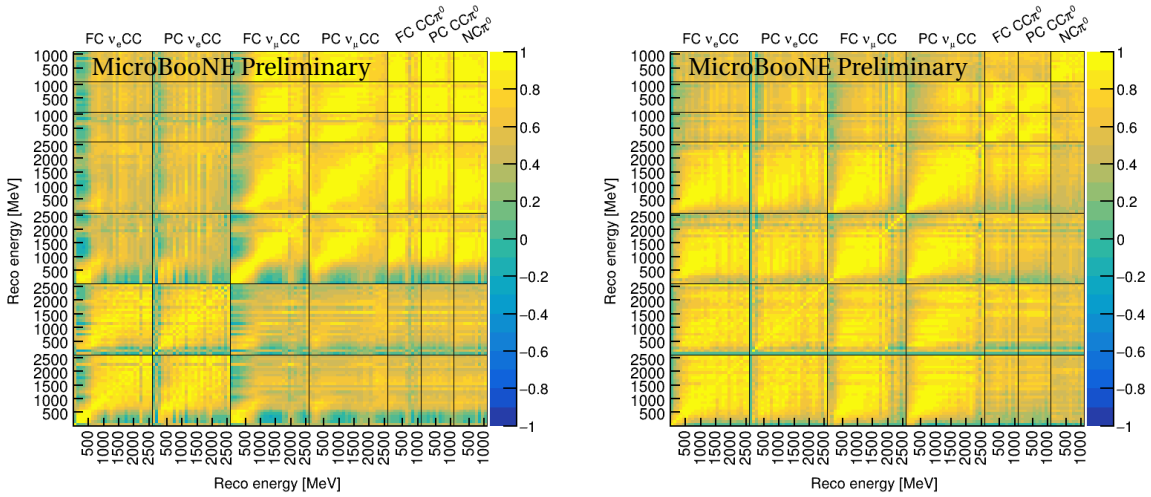

Figure 28: (Left) Correlations of flux systematics for the seven channels. (Right) Correlations of cross section systematics for the seven channels.

For detector systematic uncertainties, there are four major categories of detector systematic uncertainties: i) variations in the TPC waveform, ii) variations related to the light yield (LY) and propagation simulation, iii) variation in the space charge effect, and iv) variation in the recombination model (Recomb2). The variations in the TPC waveform includes the effect as a function of x, y/z, θ_{xz}, and θ_{yz} and are constructed by comparing the waveform between data and simulation. The light response variation includes a i) 25% uniform reduction in LY, ii) 120 cm Rayleigh scattering length (instead of the default number 60 cm), and iii) 8 meter light attenuation length to account for distance-dependent mismodeling. A separate E-field map is used to estimate the uncertainties of the space charge effect. A different recombination model, which provides slightly better agreement to the data, is used to estimate the data/MC difference in the dE/dx to dQ/dx conversion.

For each source of detector systematics, a given (same) MC event is re-simulated with a charge to the detector modeling parameter. The comparison of the new and old simulation in

terms of efficiency and reconstructed kinematic variables is used to estimate the systematic uncertainties. The change of each detector modeling parameter is treated as 1σ, meaning that there is in principle only one degree of freedom in constructing each detector covariance matrix after factoring in statistical uncertainties. The usage of the same set of events in the old and new detector simulation aims to reduce the statistical fluctuations. We utilized the bootstrapping method to estimate the statistical and the correlated systematic uncertainties. At this current stage, the statistical uncertainties are still significant in the current estimation of detector systematic uncertainties. Figure 29 shows correlations of total detector systematic uncertainties for the seven channels.

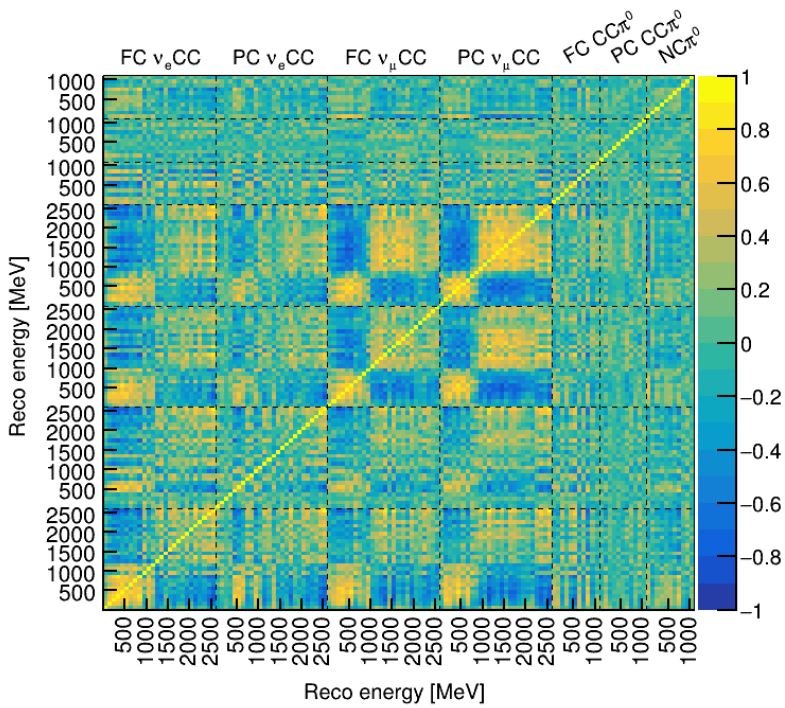

Figure 29: Correlations between the detector uncertainties for the seven channels as a function of reconstructed neutrino energy.

The DIRT events are neutrino interactions originating from outside the cryostat. The largest uncertainty associated with the DIRT events are the modeling of the outside materials. In addition to the systematic uncertainties associated with flux/Xs, we assign a conservative relative 50% bin-to-bin (uncorrelated) uncertainty to DIRT events.

Figure 31 shows correlations of total systematics for the seven channels. Figure 30 summarizes the relative uncertainties of total systematics for the seven channels. Figure 32 summarizes the contributions to the relative (fractional) uncertainties for the seven channels. For ν_eCC channels, the estimation of backgrounds (i.e. EXTBNB and DIRT) suffers the most

from the limited Monte Carlo statistics. For the ν_μCC and π^0 channels, the estimation of detector systematics suffers the most from the limited Monte Carlo statistics.

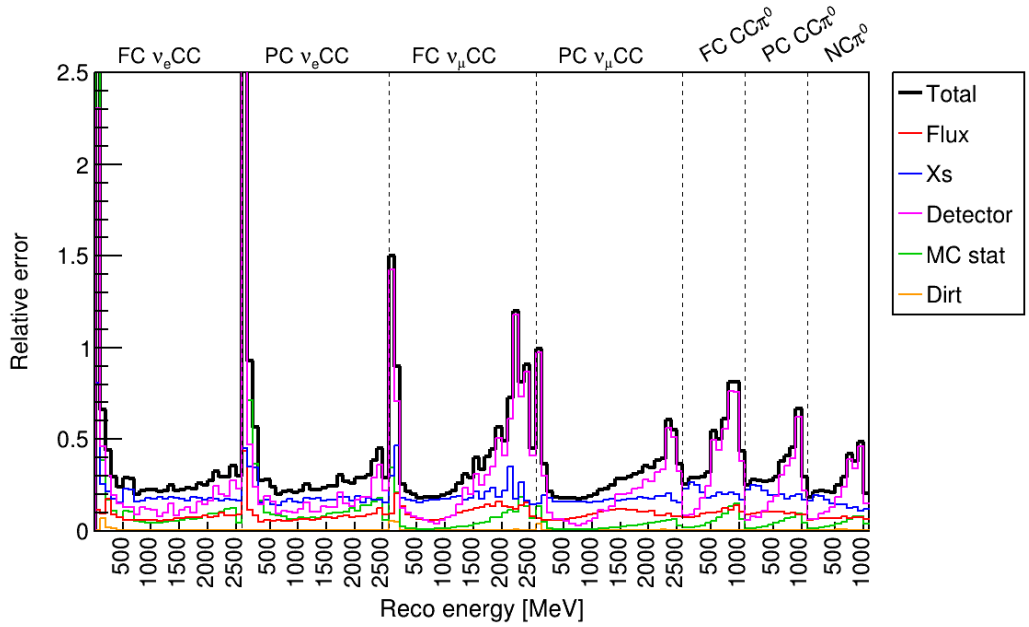

Figure 30: Summary of relative uncertainties ($\frac{\text{absolute error}}{\text{central value}}$) of total systematics for the seven channels.

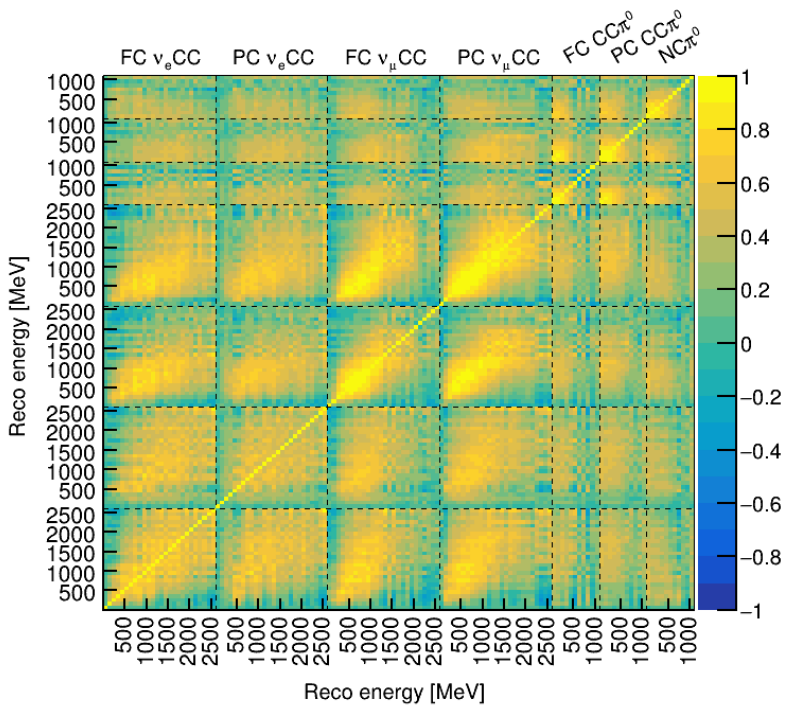

Figure 31: Correlations of total systematics for the seven channels.

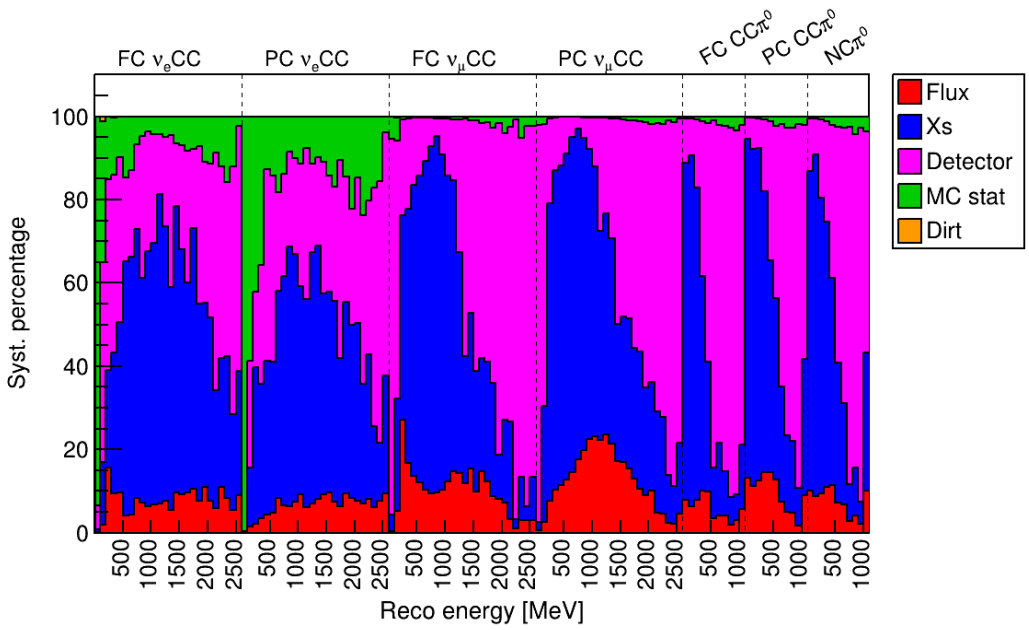

Figure 32: Summary of fraction ($\frac{\sigma_i^2}{\sigma_{\text{total}}^2} \times 100$) of uncertainties of total systematics for the seven channels.

6 Analysis of BNB Open Data [1] at 5.3e19 POT

Before proceeding to the full eLEE analysis, validation of the neutrino energy reconstruction is performed and shown in this section. Validation on ν_eCC event selection using NuMI data is presented in Sec. 7, e.g. the ν_e BDT score distribution in Fig. 39. Validation on the ν_μCC and ν_eCC event selection using BNB far sideband data[2] at 6.37e+20 POT is presented in Sec. 8.

As discussed in Sec. 2.1, three methods are used to reconstruct the neutrino energy: i) travel range, ii) recombination model by converting dQ/dx to dE/dx, and iii) EM shower energy reconstruction based on the ionization charge. The simulation of the travel range for various particle relies on a GEANT4 simulation. The recombination model used to convert dQ/dx to dE/dx is taken from Ref. [9]. A dedicated validation was done by comparing reconstructed dQ/dx as a function of the residual range between data and simulation in Fig. 33. While a difference is observed between the data and the simulation central value, the agreement is clearly improved between data and the detector variation sample ("Recomb2"), which is used to estimate the detector-related systematics.

For the EM shower energy reconstruction, the most stringent validation comes from the

[1] 5.3e19 POT of BNB data collected in MicroBooNE (3% of the total data) is openly available for validation purposes and is not blind to analyzers.

[2] Data pre-defined in a neutrino energy range outside of where a MiniBooNE-like signal is expected is available for validation purposes and is not blind to analyzers.

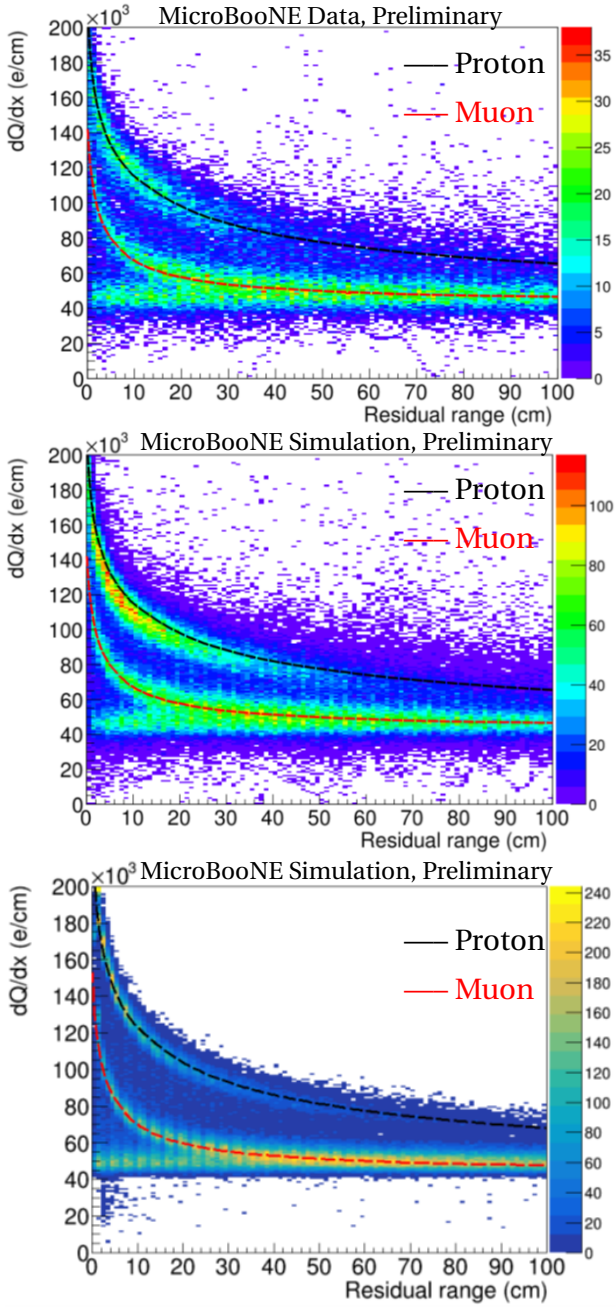

Figure 33: Comparison of data and simulation for the dQ/dx as a function of residual range: (top) data, (middle) simulation central value, and (bottom) simulation with "recomb2" detector variation. The black and red dashed lines are representing the predictions of the recombination model for protons and muons, respectively. They are the same in all three plots.

comparison of the reconstructed π^0 mass in data and Monte Carlo. Figure 34 shows the consistency between the data and simulation in all three π^0 channels. For the π^0 kinetic energy, only the EM shower energy reconstruction is involved. For the 7-channel fit, we measure the FC ν_eCC, PC ν_eCC, FC ν_μCC, and PC ν_μCC channels using reconstructed neutrino energy as described in Sec. 2.1. We chose to use 100 MeV bins from 0 to 2500 MeV, plus the overflow bin for 26 bins in total. For the FC CCπ^0, PC CCπ^0, and NCπ^0 selections, we use the kinetic energy of the π^0 after constraining the π^0 mass (M_{π^0}):

$$T_{\pi^0} = M_{\pi^0} \times \left(\sqrt{\frac{2}{\left(1-\alpha^2\right)\cdot(1-\cos\theta)}} - 1 \right), \tag{1}$$

with the asymmetry of the gamma energies defined by: $\alpha = \left(E_{\gamma\,1} - E_{\gamma\,2}\right) / \left(E_{\gamma\,1} + E_{\gamma\,2}\right)$ and angle between the two photons in the lab frame given by θ. We chose to use 100 MeV/c^2 bins from 0 to 1000 MeV/c^2, plus the overflow bin for 11 bins in total. For the π^0 channels, we chose the π^0 kinetic energy instead of the reconstructed neutrino energy, since it is expected to better reflect π^0 uncertainties in argon and is therefore expected to provide a better constraint to backgrounds to the ν_eCC event selection.

We adopted the covariance matrix formalism to construct the χ^2 test statistics:

$$\chi^2 = (M-P)^T \times Cov^{-1}_{full}(M,P) \times (M-P), \tag{2}$$

where M and P are vectors of measurement and prediction, respectively. For the 7-channel fit, the length of M (also P) is 137 = 26×4 + 11×3. The $Cov\,(M,P)$ is the full covariance matrix:

$$Cov = Cov^{stat}_{CNP} + Cov^{stat}_{MC} + R^T \times \left(Cov^{sys}_{xs} + Cov^{sys}_{flux} + Cov^{sys}_{det} + Cov^{sys}_{add} \right) \times R, \tag{3}$$

where Cov^{stat}_{CNP} is the diagonal covariance matrix constructed based on the combined-Neyman-Pearson (CNP) method [26] with the statistical uncertainty square being $3/\left(1/M_i + 2/P_i\right)$ for the ith bin. The Cov^{stat}_{MC} is the diagonal covariance matrix containing the statistical uncertainties corresponding to the finite statistics from Monte Carlo simulations. The other four covariance matrices Cov^{sys}_{xs}, Cov^{sys}_{flux}, Cov^{sys}_{det}, Cov^{sys}_{add}, are the covariance matrices corresponding to uncertainties from neutrino cross section, neutrino flux, detector performance, and DIRT, respectively. The dimensions of these four covariance matrices are larger than the final covariance matrix. There are i) FC LEE ν_eCC (26 bins), ii) PC LEE ν_eCC (26 bins), iii) nominal 7-channels excluding the contribution of EXTBNB (137 bins), and iv) 7-channels from EXTBNB (another 137 bins). Here, the two LEE ν_eCC channels are separated out from the intrinsic ν_eCC channels, since the LEE strength is expected to change. In addition, the

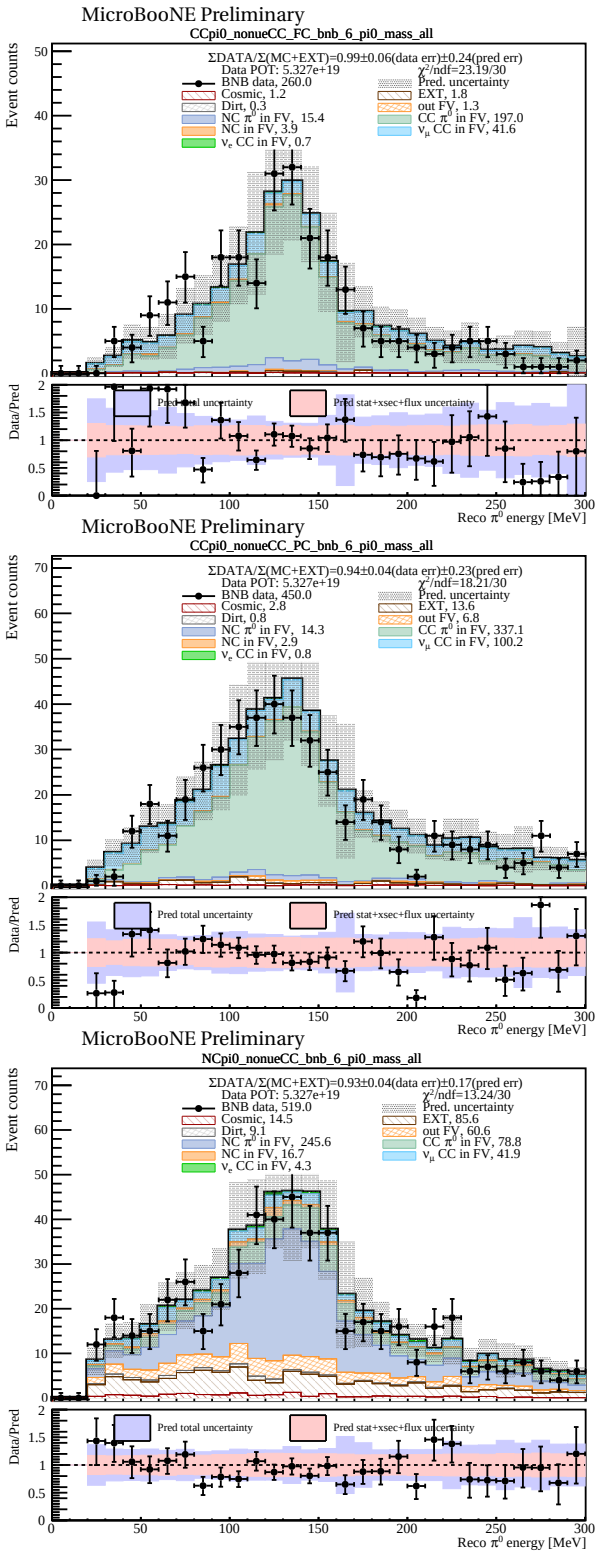

Figure 34: Comparison of the reconstructed π^0 mass between data and simulation: (top left) FC CCπ^0, (top right) PC CCπ^0, and (bottom) NCπ^0. A consistency is observed between the data and simulation validating the energy scale reconstruction for EM showers.

EXTBNB contributions to the 7 channels are also separated out, since they are not subject to various systematics (i.e. direct background measurements). R is a matrix collapsing the full covariance matrix (dimension of 26 + 26 + 137 + 137 = 326) to the final covariance matrix (dimension of 137). LEE ν_e channels are added to the corresponding ν_eCC channels. EXTBNB background contributions are also added to the corresponding channels. Except for Cov^{sys}_{add}, all covariance matrices depend on the LEE strength x.

Given the χ^2 definition in the previous section, we can perform a goodness-of-fit test. Following the recommendation of Ref. [27], we adopt the Pearson chisquare construction (instead of the CNP construction) for the statistical term for data:

$$Cov = Cov^{stat}_{Pearson} + Cov^{stat}_{MC} + R^T \times \left(Cov^{sys}_{xs} + Cov^{sys}_{flux} + Cov^{sys}_{det} + Cov^{sys}_{add}\right) \times R, \qquad (4)$$

with the statistical uncertainty being the square root of P_i for the ith bin. Given the null hypothesis (i.e. standard model), the chisquare value can be used to perform the goodness-of-fit test by comparing with the chisquare distribution with 137 degrees of freedom (dof), which is the total number of bins in the 7-channel analysis.

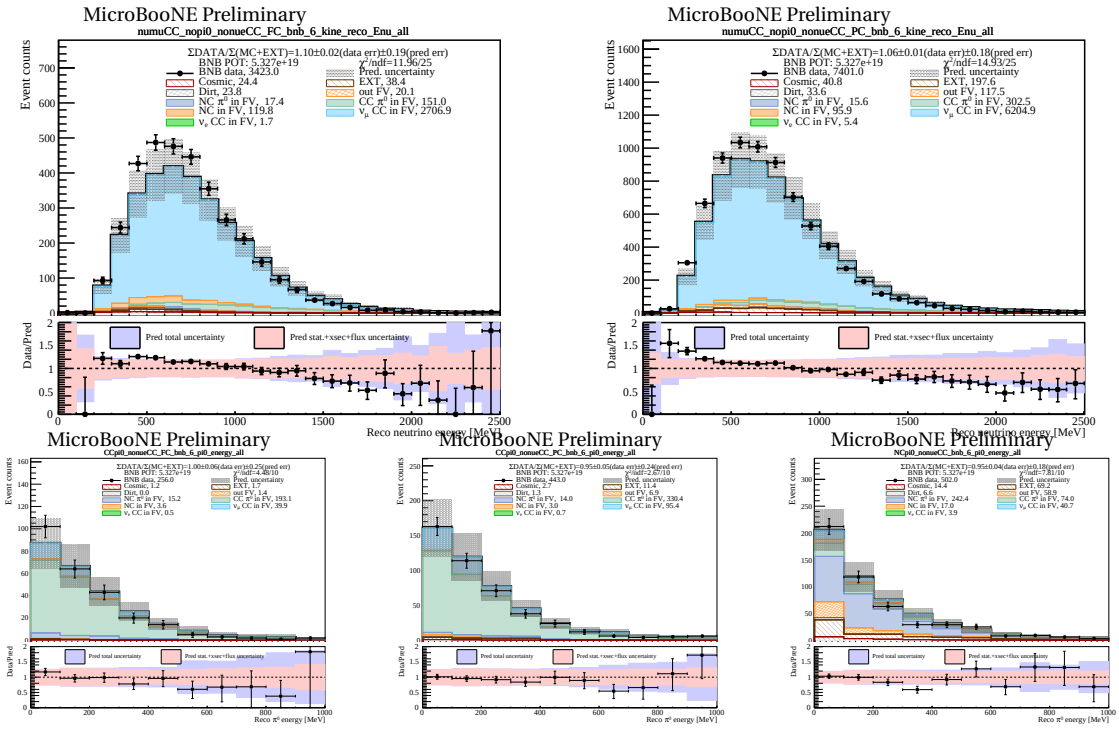

Figure 35: Distribution of 7-channel selection results from open data: (from left to right, top to bottom) fully contained ν_μ CC, partially contained ν_μ CC, fully contained CC π^0, partially contained CC π^0, and NC π^0. The available open data result is overlaid and the pink band in the bottom panel presents the systematic uncertainty of the prediction. ν_eCC results (FC and PC channels) are omitted following the blinding requirement.

The above goodness-of-fit test provides an overall evaluation of the model and the null hypothesis compatibility with the data. This evaluation can be broken into different parts of the model using the conditional covariance matrix formalism [28, 29]. For example, given the full covariance (stat + sys) containing two channels (X, Y):

$$\Sigma = \begin{pmatrix} \Sigma^{XX} & \Sigma^{XY} \\ \Sigma^{YX} & \Sigma^{YY} \end{pmatrix}, \quad n: \text{measurement}, \quad \mu: \text{ prediction}, \tag{5}$$

we can derive the prediction on X given the constraints on Y:

$$\mu^{X,constrained} = \mu^X + \Sigma^{XY} \cdot \left(\Sigma^{YY}\right)^{-1} \cdot \left(n^Y - \mu^Y\right), \tag{6}$$

$$\Sigma^{XX,constrained} = \Sigma^{XX} - \Sigma^{XY} \cdot \left(\Sigma^{YY}\right)^{-1} \cdot \Sigma^{YX}. \tag{7}$$

Thus, a goodness-of-fit test can be performed on Y first, and then performed on X after the constraints of Y. This allows the examination of the model compatibility with X and Y individually.

Given the χ^2 definition and its relation to the log likelihood, we can form a simple-vs-simple likelihood ratio test statistics:

$$\Delta\chi^2_{simple} = \chi^2_{SM} - \chi^2_{LEEx=1}, \tag{8}$$

comparing two simple hypotheses: standard model (SM) and LEE hypothesis with the LEE strength x fixed to unity. This test statistics allows one to calculate p-values with a full frequentist approach (i.e. with pseudo data) assuming the SM is true. This is effectively another way to perform the "goodness-of-fit" test (i.e. test the compatibility between the data and the SM hypothesis).

The primary test statistics used in this analysis is a nested Likelihood ratio:

$$\Delta\chi^2_{nested} = \chi^2(x = x_0) - \chi^2_{min}(x = x_{min}), \quad x_{min} \geq 0, \tag{9}$$

where the value of x_0 defines the null hypothesis. For example $x_0 = 0$ represents the standard model (SM), and $x_0 = 1$ is the $LEEx = 1$ hypothesis. x_{min} is the best-fit x value in the allowed physics region ($x_{min} \geq 0$) after minimizing $\chi^2(x)$. The minimal χ^2 at $x = x_{min}$ is labeled as χ^2_{min}. This test statistics compared two hypotheses: i) null hypothesis $x = x_0$ and ii) an alternative hypothesis that x can be anything within the allowed physics region. Since the null hypothesis is part of the alternative hypothesis, this test is referred to as nested hypothesis testing.

Given the test statistics defined in Eq. 9, we can perform the full Frequentist approach to derive the p-value against the null hypothesis (i.e. the Feldman-Cousins approach [15]). At large statistics, one may also rely on the Wilks' theorem to estimate the p-value. Compared to GoF test with only χ^2, this nested likelihood ratio test is more powerful following the guidance of the Neyman-Pearson lemma [30], which states that for a fixed probability of rejecting the null hypothesis when it is true (level), the probability for rejecting the null hypothesis when the alternative is true (power) is maximized with the likelihood ratio test statistic. Compared to the simple-vs-simple likelihood ratio test, this nested likelihood ratio test is more powerful given that the alternative hypothesis covers many more new physics possibilities. Therefore, this test statistics and its associated hypothesis testing is our primary discriminant in quantifying the search for eLEE.

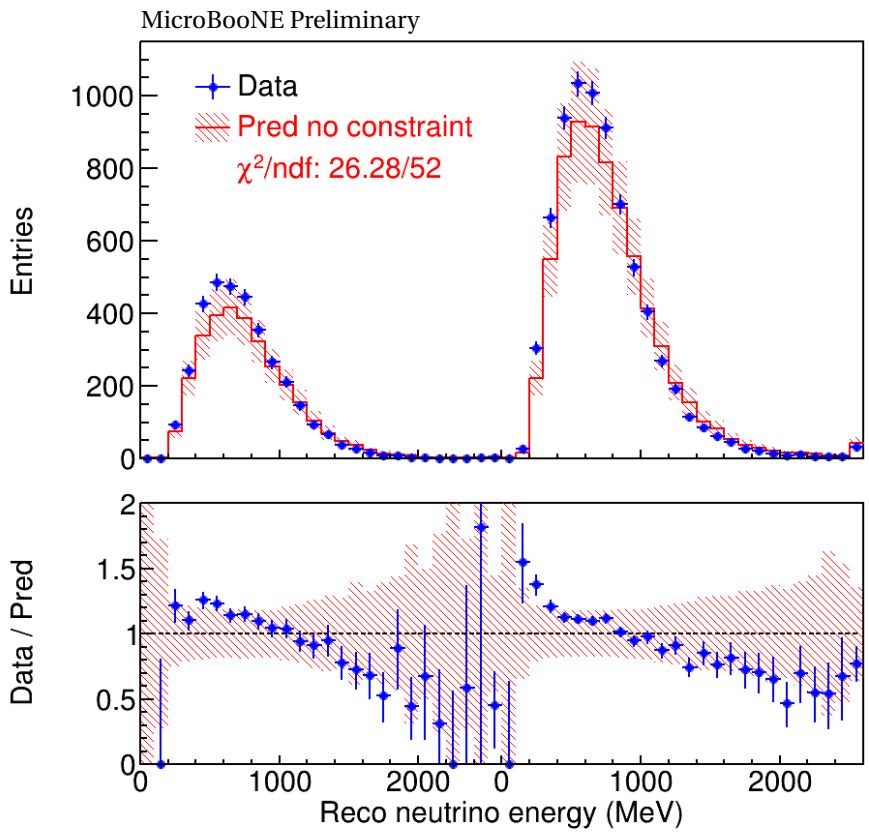

Figure 36: Comparison between data and prediction for ν_μCC channels. The first (second) 26 bins represent the FC (PC) channel. The error band represents the total systematic uncertainty. The last bin represents the overflow bin for reconstructed neutrino energy higher than 2500 MeV.

With the aforementioned techniques and selection criteria, the 7-channel selection results

from the initial open 5.3e19 POT of BNB data are presented. Figure 35 shows the stacked histograms of each component of the signal and background events from the Monte Carlo prediction with the data displayed with full systematic errors. Figure 36 shows the comparison between data and prediction with systematic uncertainties. At low (high) energies, the data is higher (lower) compared to the central values of the Monte-Carlo prediction. The goodness-of-fit combining both ν_μCC channels is $\chi^2/NDF = 26.28/52$ and the data/MC differences is within the systematic uncertainties.

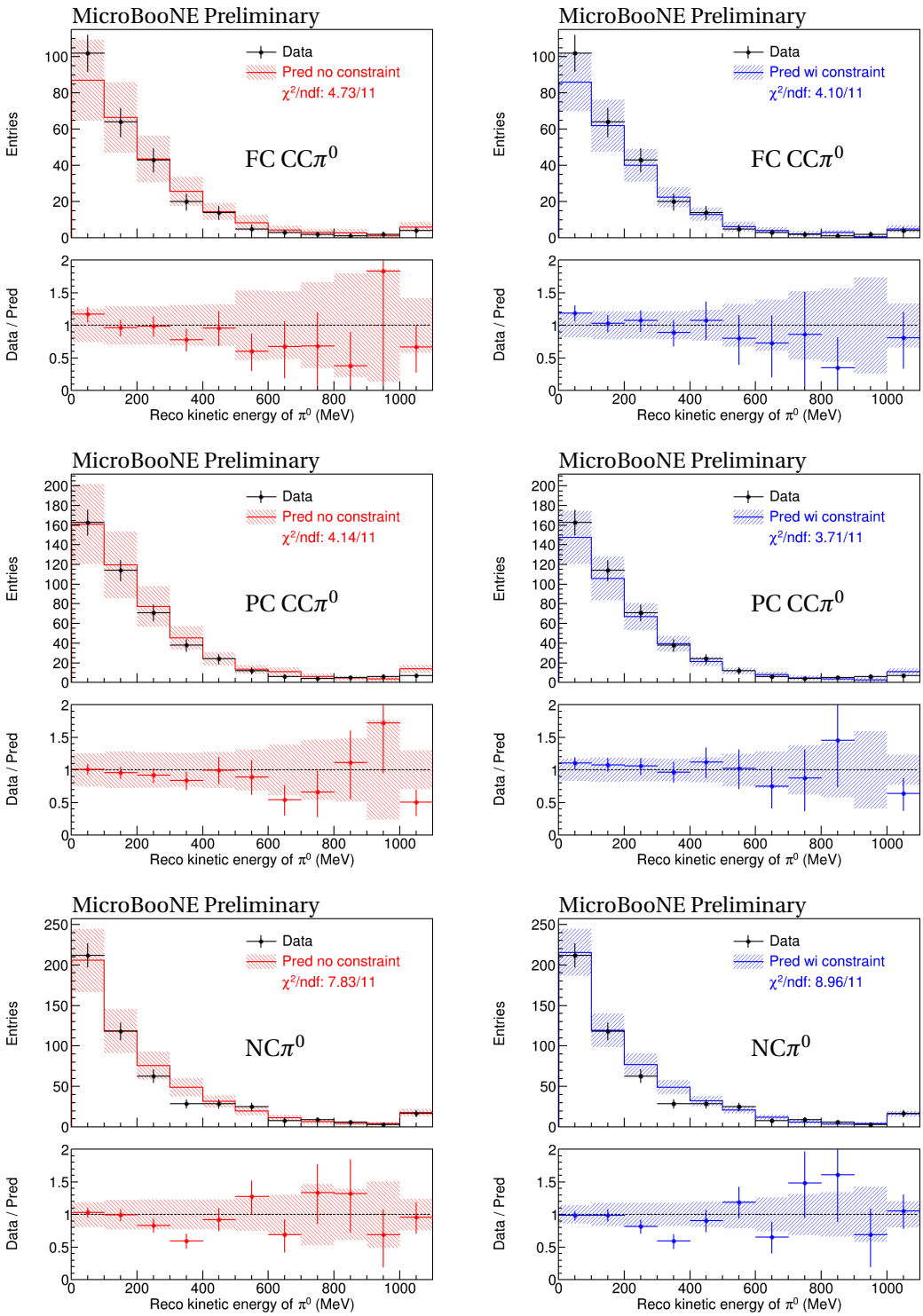

Figure 37: Comparison between data and prediction for three π^0 channels: (top) FC CCπ^0, (middle) PC CCπ^0, (bottom) NCπ^0. Left (right) panels show the result before (after) applying the ν_μCC constraints. The error band shows the total systematic uncertainty. The bin index represents the bin number in the reconstructed kinetic energy of π^0 from 0 to 1000 MeV at a bin width of 100 MeV. The 11th bin represents the overflow bin.

Figure 37 shows the three π^0 channels before and after applying constraints from the ν_μCC channels. After applying the data-based constraints, the CCπ^0 prediction is reduced as a result of the data measurement at higher energies in the ν_μCC sample. For the NCπ^0, with the larger data-MC difference after the constraints and systematic uncertainties getting smaller after the constraints, it leads to slightly worse GoF values after applying the constraints. The GoF of all tests are still very good, indicating the difference between the data and predictions are well within the total statistical and systematic uncertainties.

7 ANALYSIS OF NUMI DATA AT 2.10E20 POT

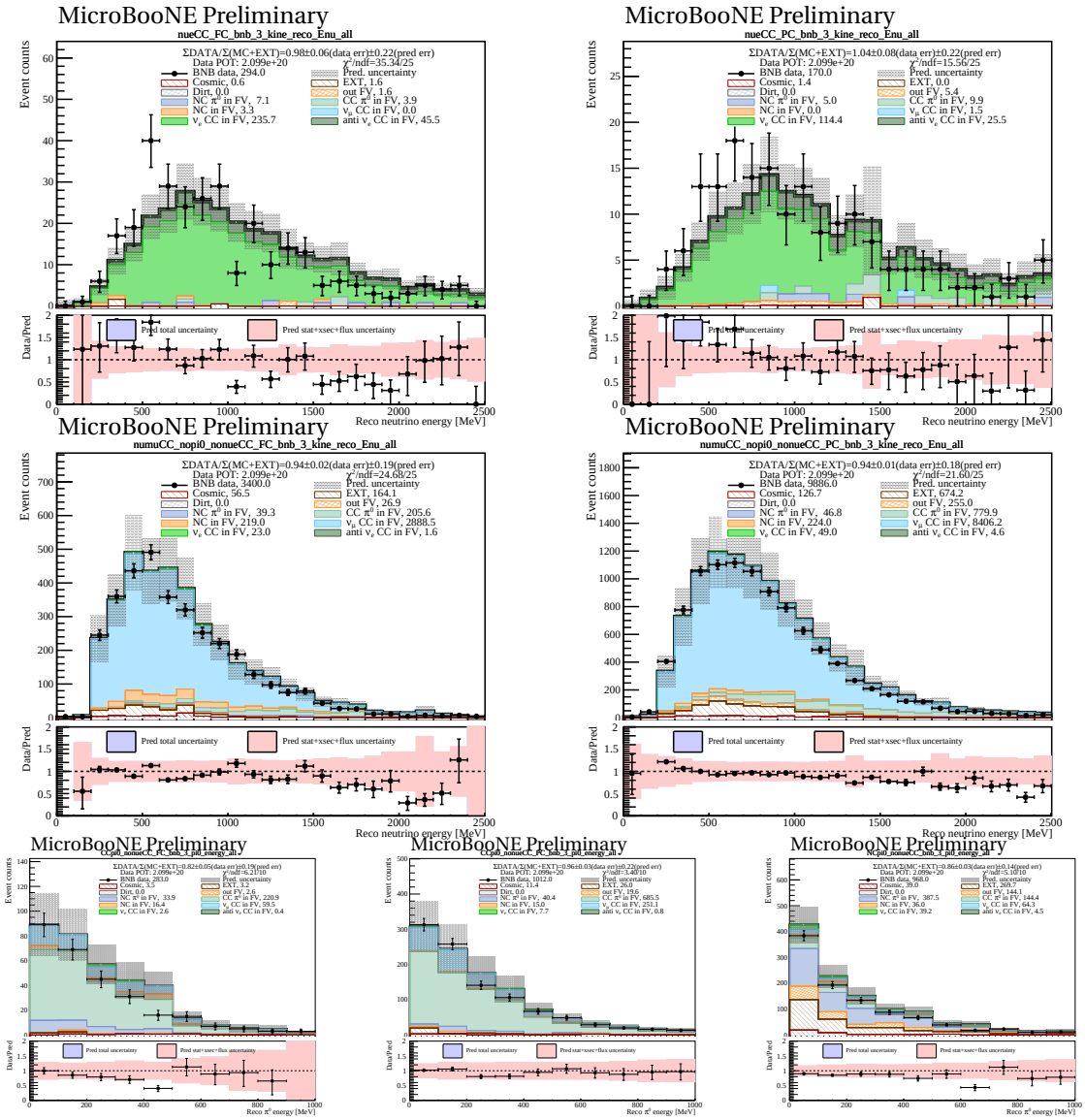

Figure 38: Distribution of 7-channel selection results from NuMI run1 data: (from left to right, top to bottom) fully contained ν_e CC, partially contained ν_e CC, fully contained ν_μ CC, partially contained ν_μ CC, fully contained CC π^0, partially contained CC π^0, and NC π^0. MC statistics, flux & cross-section uncertainty are included in the final uncertainty, shown in the red band in the panels below.

The current open data of the BNB data stream (~5.3e+19 POT) is limited by statistics, especially for FC ν_eCC channel at low-energy region. At the same POT, the NuMI data stream has about three times more ν_eCC events than that of BNB data stream in the low-energy region. The analysis of this channel is thus expected to provide useful information regarding the ν_eCC event selection. Figure 38 shows the result from the selections, for all the 7 channels.

The same event reconstruction and event selections are applied to the NuMI data as for BNB data. The only change is the coincidence window between the PMT flash with the trigger time (9 μs instead of 1.6 μs of BNB). The data/MC are consistent within systematic uncertainties. The distribution of nue BDT scores of NuMI events is presented in Fig. 39. It also shows a good agreement between data and Monte-Carlo, indicating the validity of the BNB ν_eCC BDT selection. Currently, the "Dirt" sample is not yet included, but given the purity of the selection on available Monte-Carlo samples, we expect its impact to be minimal. Nevertheless, future iterations of the analysis will include the study of this sample.

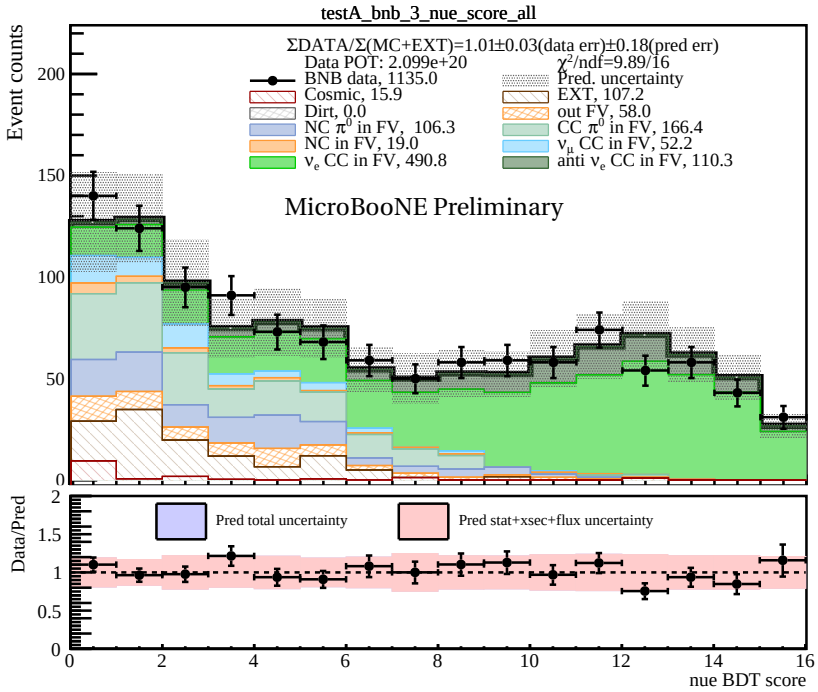

Figure 39: ν_e BDT score (greater than 0) distribution for both fully contained and partially contained event candidates. The NuMI data result is overlaid and the bottom panel presents the systematic uncertainty of the prediction, including MC statistic, cross section and flux uncertainties.

To demonstrate the similarity in the ν_eCC event selection, Fig. 40 shows the ν_e selection efficiency comparison between the BNB and NuMI data streams, as a function of true neutrino energy. The efficiency is comparable between two data streams, both in fully contained and combined samples, but slightly lower with NuMI FC sample compared to that of BNB. The data/MC consistency in the ν_eCC event selection in NuMI data validates the ν_eCC event selection strategy, and further validates the ability of the Wire-Cell reconstruction and selection to identify a sample of data-based low energy electron neutrino events.

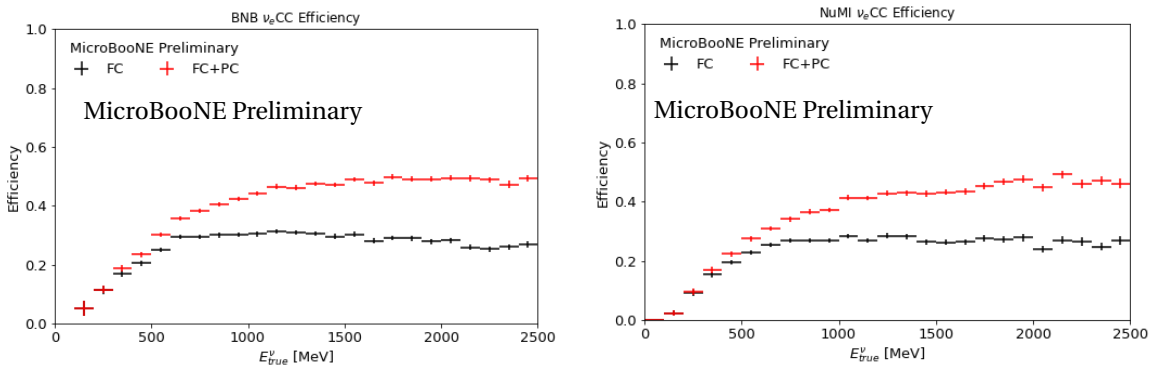

Figure 40: Selection efficiency of ν_eCC between BNB and NuMI data stream, as a function of true neutrino energy. The efficiency of NuMI data stream is slightly lower because the BDT was trained by BNB samples and directly applied on NuMI data.

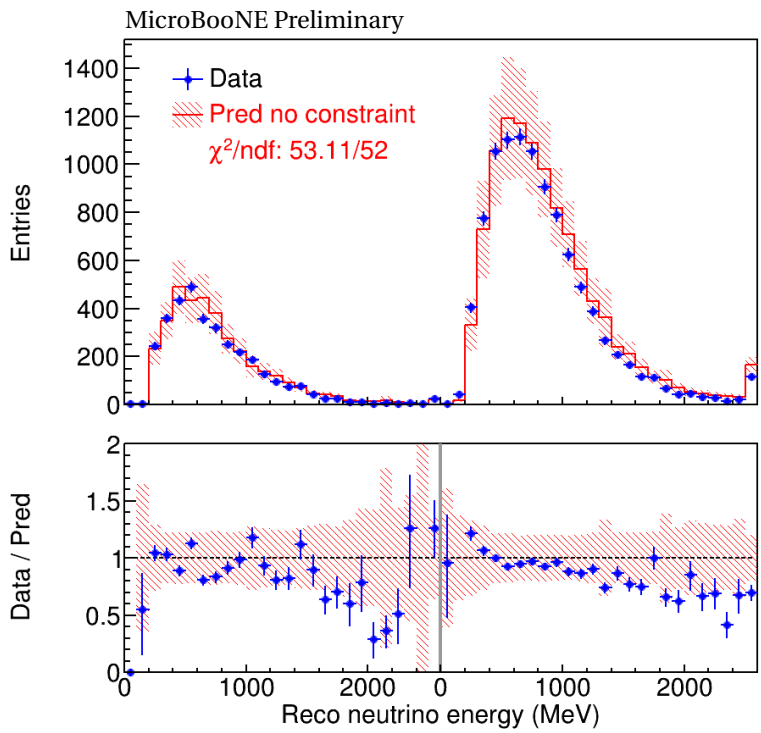

Figure 41: Comparison between data and prediction for ν_μCC channels. The first (second) 26 bins represents the FC (PC) channel. The error band represents the systematic uncertainties without the detector systematics. The bin index represents the bin number in reconstructed neutrino energy spanning from 0 to 2500 MeV at a bin width of 100 MeV. The 26th bin represents the overflow bin for reconstructed neutrino energy higher than 2500 MeV.

We further test the data/MC consistency with the existing systematics (no detector sys-

tematics at this moment). Figure 41 shows the data/MC comparison for the NuMI ν_μCC events for both the fully contained (FC) and partially contained (PC) samples. The overall goodness-of-fit (GoF: χ^2/NDF) shows that the data is consistent with the overall model with its uncertainties for both FC and PC samples.

Figure 42 shows the three π° channels before and after applying the constraints from the ν_μCC channels. After applying constraints, the prediction for the CCπ° channels is decreased. The GoF of all tests are very good, indicating the difference between the data and predictions are well within the total statistical and current systematic uncertainties. The GoF after applying constraints are slightly worse than that before applying the constraints, which is the result of reduced uncertainties and/or larger difference between data and prediction. After the constraints of the ν_μCC, there is an improvement between data and MC in terms of the overall normalization for the NCπ° channel.

Figure 43 shows the comparison of data and prediction for FC ν_eCC (top) PC ν_eCC (bottom) before (left) and after (right) applying constraints from ν_μCC and π^0 channels. For ν_eCC FC channel, the GoF after constraints gives $\chi^2/NDF = 38.11/26$ corresponding to a p-value of 0.059. Note, there is no detector systematic uncertainties included currently. There is a hint of a slight excess at low energy and small deficit of at high-energy for ν_eCC FC sample.

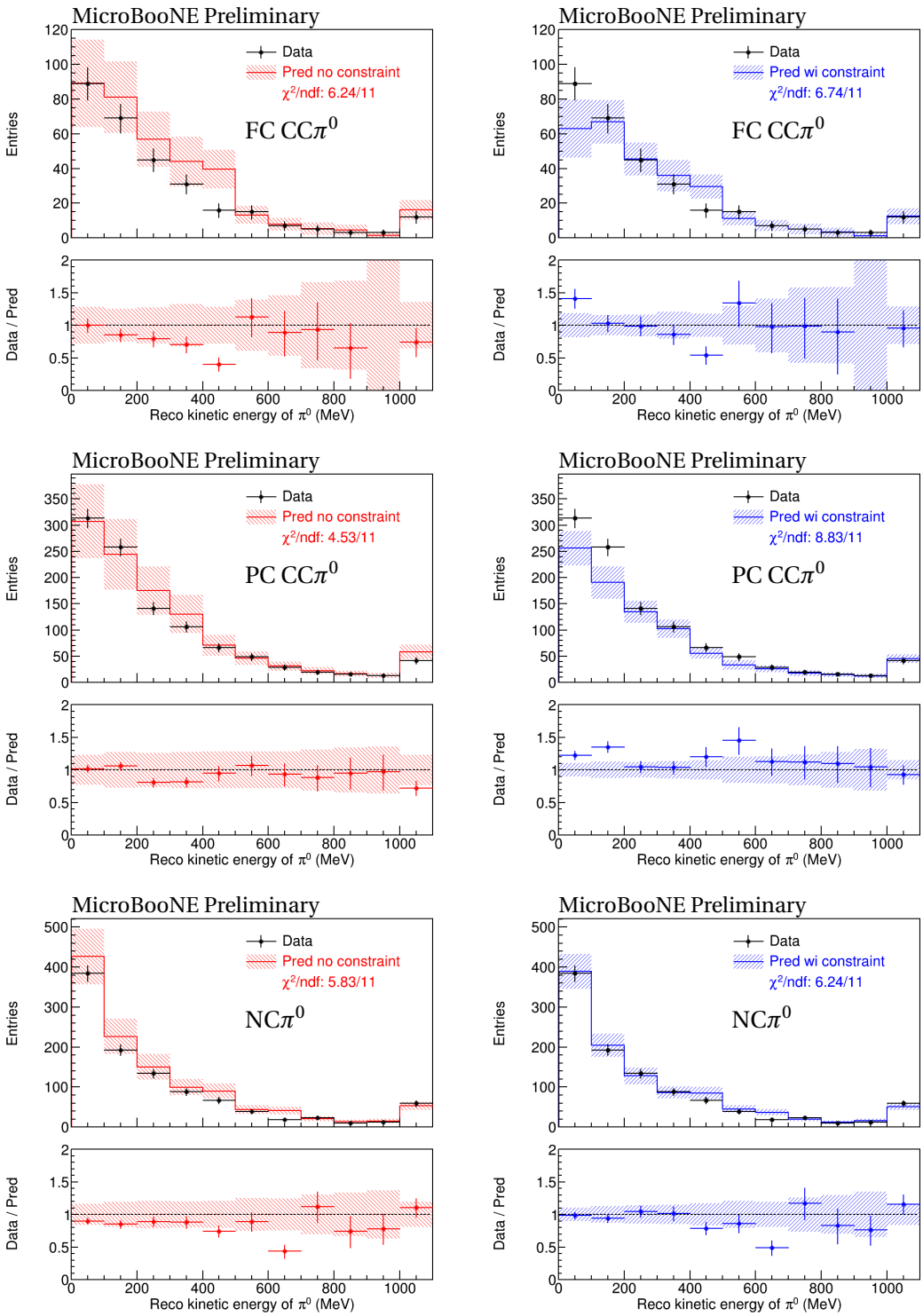

Figure 42: Comparison between data and prediction for three π^0 channels: (top) FC CCπ^0, (middle) PC CCπ^0, (bottom) NCπ^0. Left (right) panels show the result before (after) applying the ν_μCC constraints. The error band shows the current systematic uncertainties. The bin index represents the bin number in the reconstructed kinetic energy of π^0 from 0 to 1000 MeV at a bin width of 100 MeV. The 11th bin represents the overflow bin.

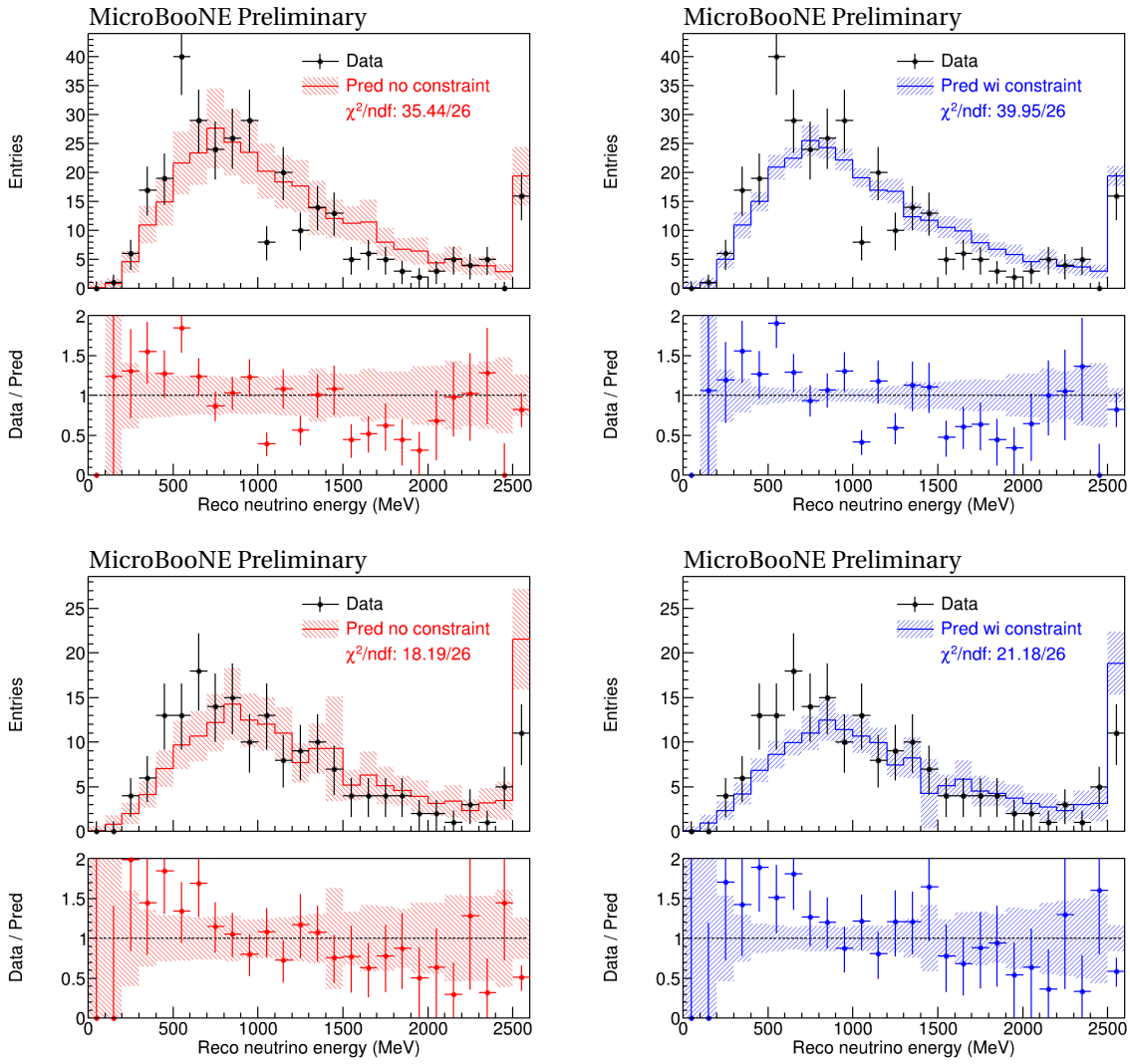

Figure 43: Comparison of data and prediction for FC ν_eCC (top) PC ν_eCC (bottom) before (left) and after (right) applying constraints from ν_μCC and π^0 channels. The error bands show the current systematic uncertainties. For data points, the error bars represent the Bayesian 68% credible intervals. The bin index represents the bin number in the reconstructed neutrino energy from 0 to 2500 MeV with a bin width of 100 MeV. The last bin is the overflow bin.

In the end, to shed light on the slight excess of ν_eCC candidates around 600 MeV region, we hand scan the 400 - 800 MeV data events from the ν_eCC FC channel and ν_eCC PC channel in BEE display with a sub-sample, which corresponds to 2.10e20 POT NuMI data. None of the selected events show unexpected features. The links to the FC and PC channels are `https://www.phy.bnl.gov/twister/bee/set/uboone/reco/2021-01/numi-nue-fc-400-800-mev/event/list/` and `https://www.phy.bnl.gov/twister/bee/set/uboone/reco/2021-01/numi-nue-pc-400-800-mev/event/list/` respectively. An

example ν_eCC candidate is shown below.

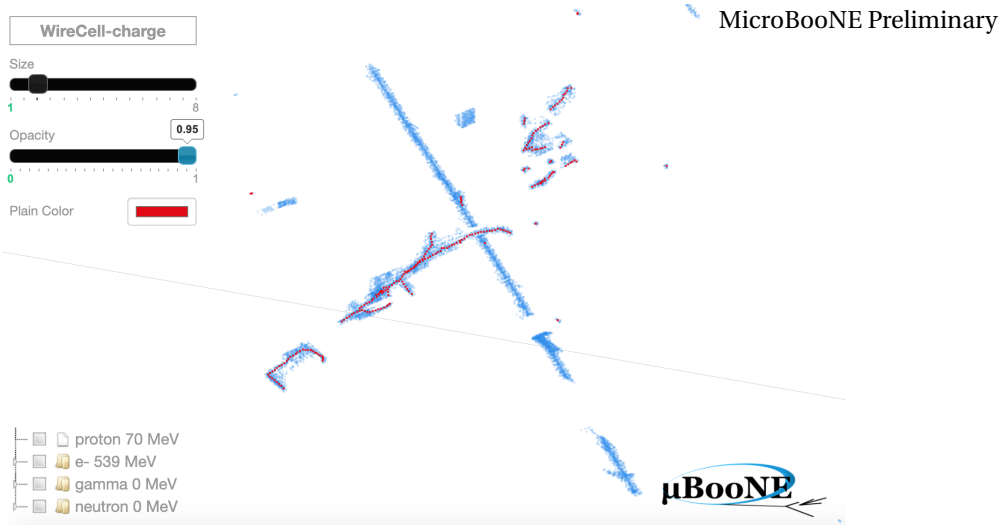

Figure 44: 1e1p FC ν_eCC. The blue space points are reconstructed clusters, and the red space points are fitted trajectory of the selected neutrino cluster. (`https://www.phy.bnl.gov/twister/bee/set/uboone/reco/2021-01/numi-nue-fc-400-800-mev/event/0/`)

8 Analysis of BNB Far Sideband Data at 6.37e20 POT

The definition of the Wire-Cell far and near sidebands is shown in Fig. 45. More details can be found in Ref. [31].

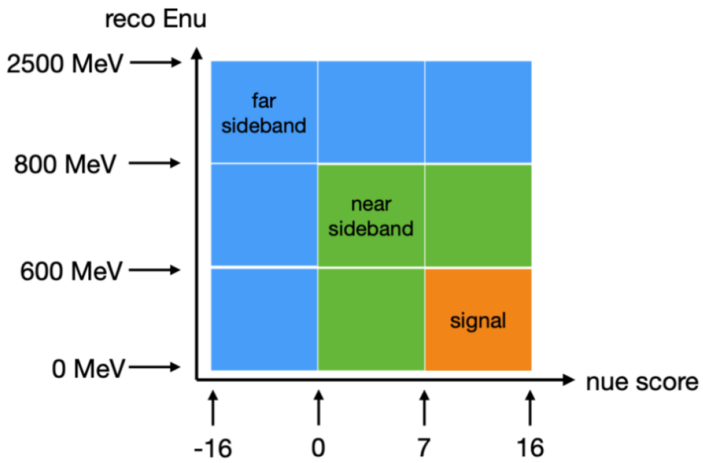

Figure 45: Definition of Wire-Cell far and near sidebands.

8.1 Validation of π^0 mass reconstruction

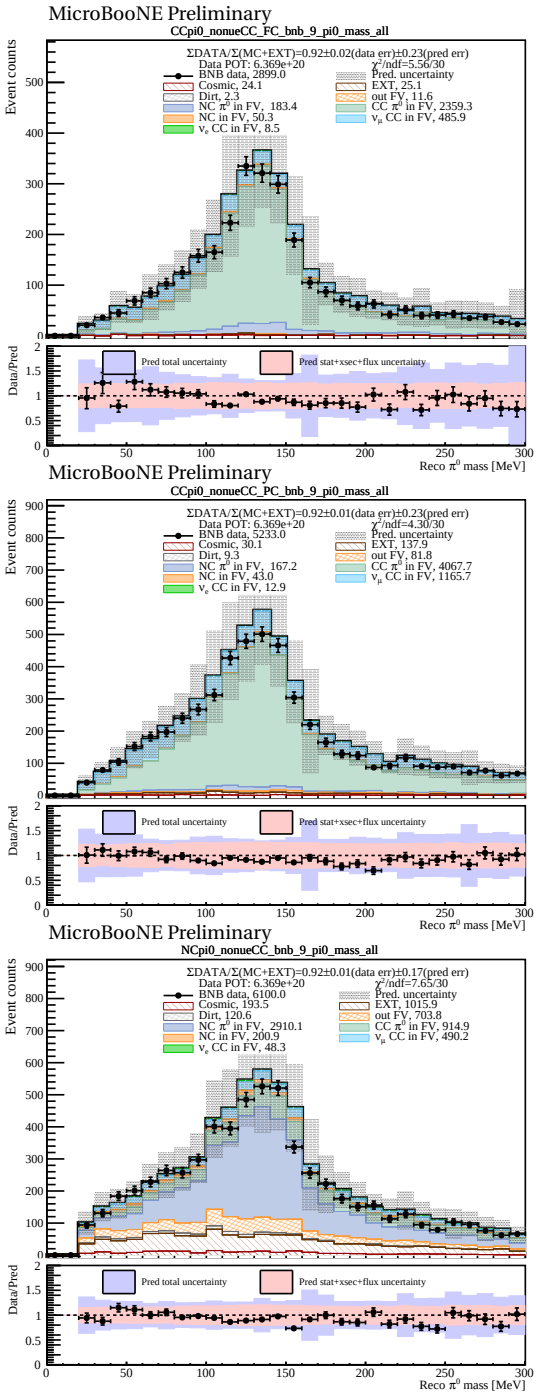

Figure 46: Distribution of the reconstructed π^0 mass from far sideband: (from top to bottom) fully contained π^0 CC, partially contained π^0 CC, and NC π^0. The bottom panels in each sub-figure present the data/MC ratios.

The scale of EM shower energy reconstruction is checked with the reconstructed neutral pion mass peak. The data/MC comparisons of the reconstructed π^0 mass peak are shown in Fig. 46 for three π^0 channels. The alignments of the reconstructed π^0 mass peaks between data and MC are good, which are also indicated by the GoF values.

8.2 Validation of reconstruction of neutrino vertex

Figure 47 shows the data/MC comparison of the reconstructed neutrino vertex Z position. The data is consistent with MC prediction within uncertainties indicated by the good GoF values.

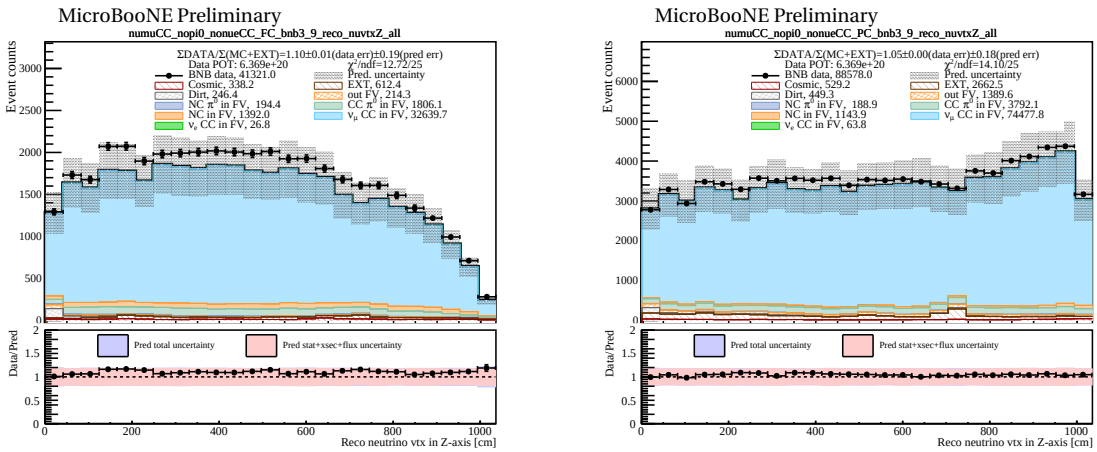

Figure 47: Distribution of the neutrino vertex along the beam direction for ν_μ CC data in MicroBooNE Runs 1-3 corresponding to 6.37e20 POT: fully contained ν_μ CC (left) and partially contained ν_μ CC (right). The bottom panels in each sub-figure present the ratio of data/Monte Carlo.

Figure 48 shows the data/MC comparison of the reconstructed neutrino vertex X position combining all three run periods. In the PC channel, there are hints of small data deficit at small vertex X position (near anode, likely related to the scintillation light simulation, since PMTs are all located at the anode plane side), and excess in the middle of the detector (likely related to the kinematics of final state particles as well as the scintillation light simulation). Nevertheless, the data is shown to be consistent with MC prediction within uncertainties indicated by the good GoF values.

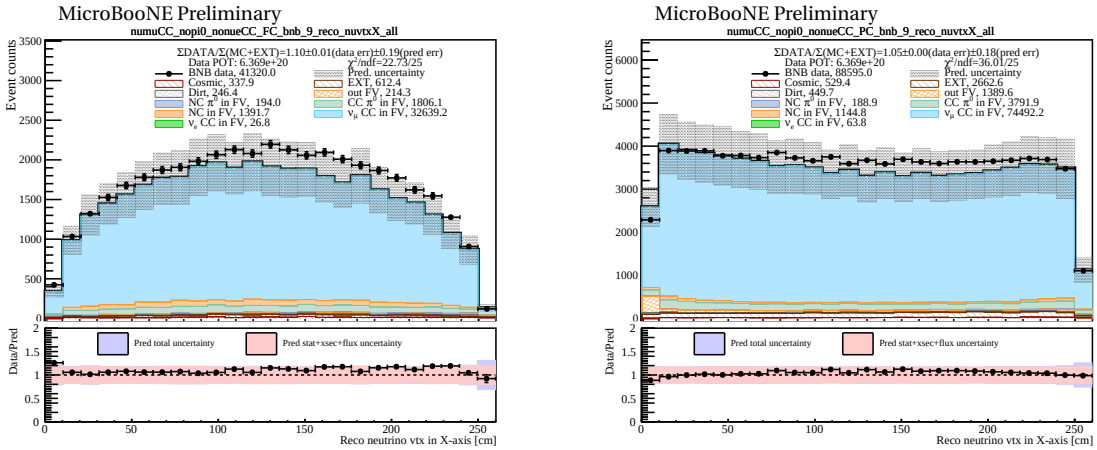

Figure 48: Distribution of the neutrino vertex X position for ν_μ CC data in MicroBooNE Runs 1-3 corresponding to 6.37e20 POT: fully contained ν_μ CC (left) and partially contained ν_μ CC (right). The bottom panels in each sub-figure present the data/pred ratios.

Figure 49 shows the data/MC comparison of the reconstructed neutrino vertex Y position after combining all run periods. The data is shown to be consistent with uncertainties indicated with good GoF values.

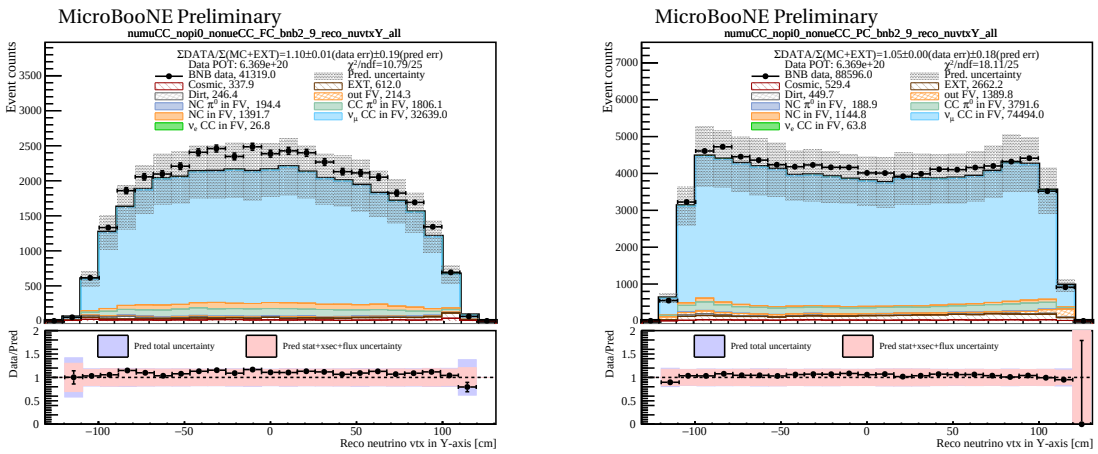

Figure 49: Distribution of the neutrino vertex Y position for ν_μ CC data in MicroBooNE Runs 1-3 corresponding to 6.37e20 POT: fully contained ν_μ CC (left) and partially contained ν_μ CC (right). The bottom panels in each sub-figure present the data/pred ratios.

8.3 Validation of ν_μCC muon kinematics distributions

Figure 50 shows the ν_μ BDT score distribution. Figure 51, figure 52, and figure 53 show the data/MC comparison of the reconstructed muon kinematic energy, $cos\theta$ (polar angle), and ϕ (azimuthal angle), respectively. The data is consistent with MC prediction within uncertainties as indicated by the good GoF values. Note that we see an overall larger rate in

the data than in MC, which is covered with reported uncertainties.

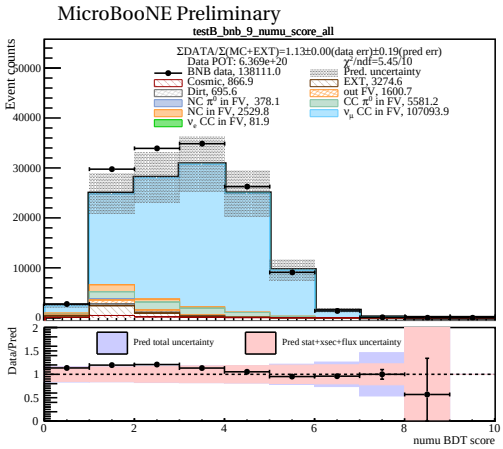

Figure 50: Distribution of the ν_μBDT score distribution for ν_μ CC data in MicroBooNE Runs 1-3 corresponding to 6.37e20 POT.

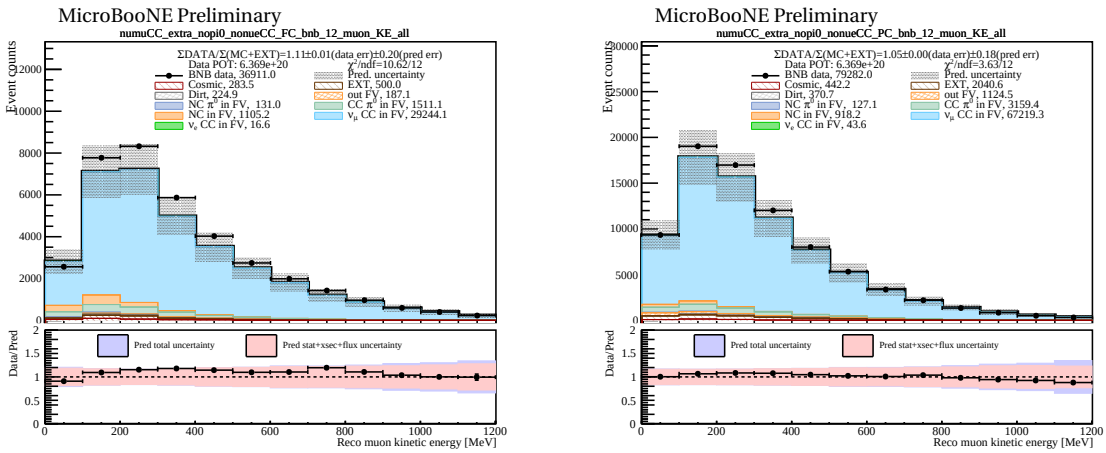

Figure 51: Distribution of the reconstructed muon kinematic energy for ν_μ CC data in MicroBooNE Runs 1-3 corresponding to 6.37e20 POT: fully contained ν_μ CC (left) and partially contained ν_μ CC (right). The bottom panels in each sub-figure present the data/pred ratios and their systematic uncertainties.

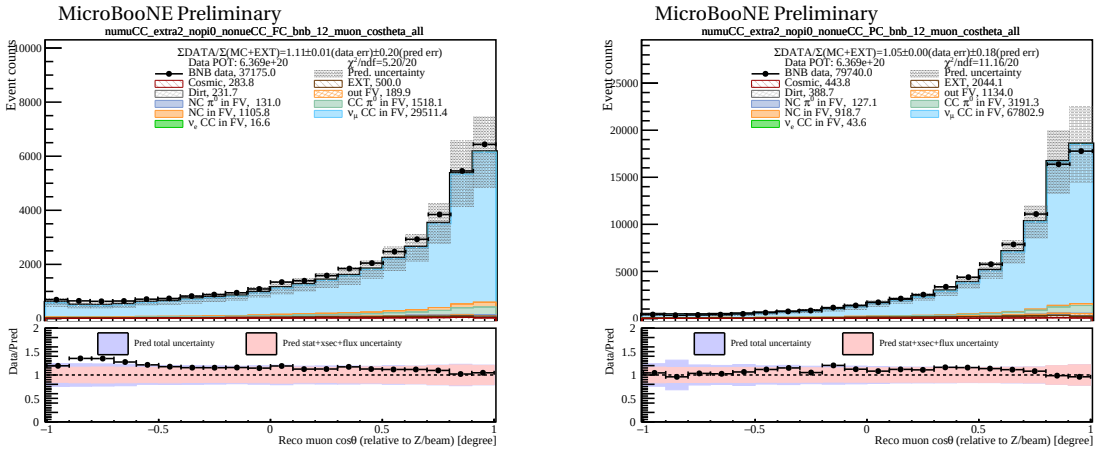

Figure 52: Distribution of the reconstructed muon $cos\theta$ for ν_μ CC data in MicroBooNE Runs 1-3 corresponding to 6.37e20 POT: fully contained ν_μ CC (left) and partially contained ν_μ CC (right). The bottom panels in each sub-figure present the data/pred ratios and their systematic uncertainties.

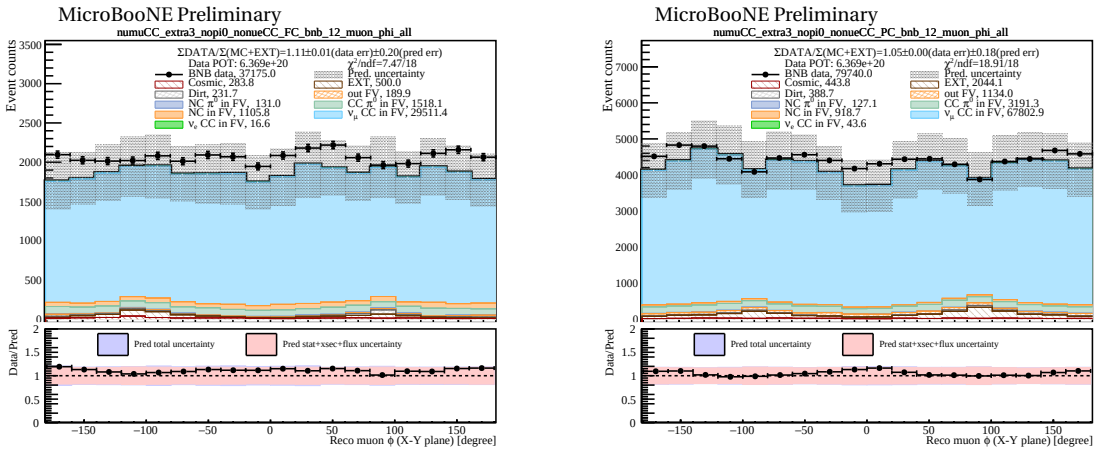

Figure 53: Distribution of the reconstructed muon ϕ angle for ν_μ CC data in MicroBooNE Runs 1-3 corresponding to 6.37e20 POT: fully contained ν_μ CC (left) and partially contained ν_μ CC (right). The bottom panels in each sub-figure present the data/pred ratios and their systematic uncertainties.

8.3.1 Validation of ν_eCC far sideband event selection

Figure 54 shows the data/MC comparison for the ν_eCC BDT score distributions. The data is consistent with MC prediction within its uncertainties indicated by good GoF values. Figure 55 shows the data/MC comparison as a function of the reconstructed neutrino energy for the far sideband (ν_eCC BDT score larger than zero). The data are consistent with MC prediction within its uncertainties indicated by the good GoF values. Across these figures, the data is consistent with the MC prediction indicated by the good GoF values. In some

regions where CC or NC π^0 events are considerable, a slight deficit would be expected in data as indicated by the π^0 selection in Fig. 64.

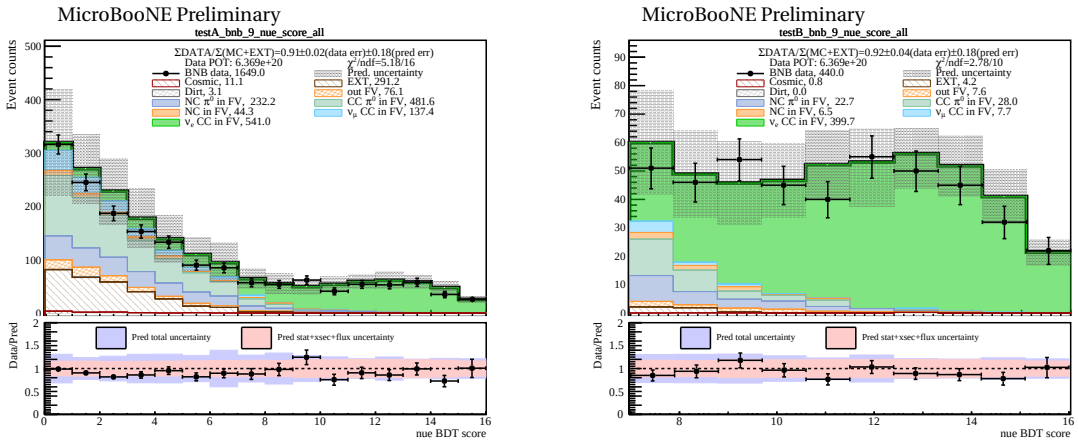

Figure 54: ν_eCC BDT score distribution for ν_μ CC data in MicroBooNE Runs 1-3 corresponding to 6.37e20 POT. Left: BDT score>0, Right: BDT score>7 (current ν_eCC selection). The bottom panels in each sub-figure present the data/pred ratios and the systematic uncertainties. The pink band represents the MC stat, flux, and cross section uncertainties, and the purple band represents an addition of detector systematic uncertainty.

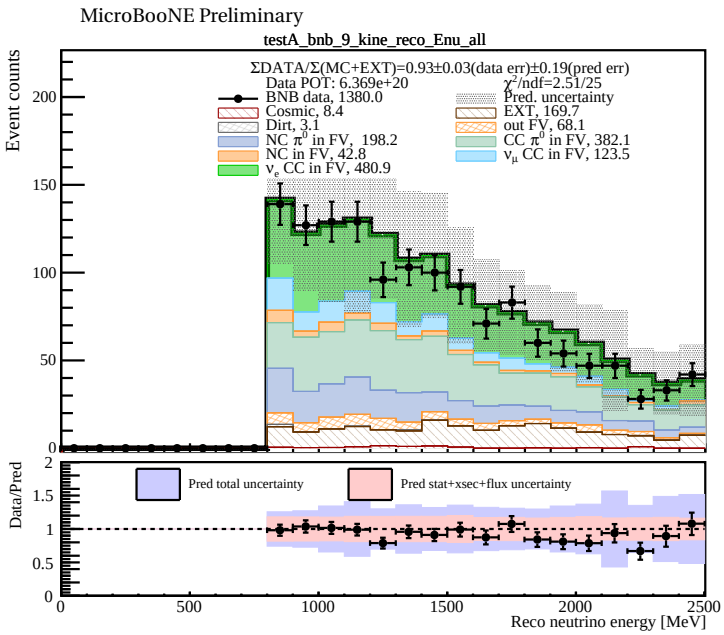

Figure 55: Selected ν_eCC events with loose ν_e selection (BDT score>0). ν_eCC data events below 800 MeV are blinded.The bottom panels in each sub-figure present the data/pred ratios and the systematic uncertainties. The pink band represents the MC stat, flux, and cross section uncertainties, and the purple band represents an addition of detector systematic uncertainty.

8.4 ν_μCC 0p Np separation

In this section, ν_μCC $0p$ vs. Np separation is presented for far sideband data. Here, $0p$ means there's no proton in the final state, where Np means one or more protons in the final state. More detailed description of these different final states can be found on a glossary **??**. As shown in Fig. 56, we observed an obvious enhancement of ν_μCC events in the $0p$ channel in data, which decomposes the "slope" of data/pred ratio we observed in the regular ν_μCC selection shown in Fig. 64 into two separate channels. Protons here are from Wire-Cell pattern recognition and include both primary protons and isolated protons (e.g. from neutron scattering) with kinetic energy greater than 35 MeV. $0p$ channel only shows excess except for the very high energy region, and Np channel only shows deficit in very high energy region.

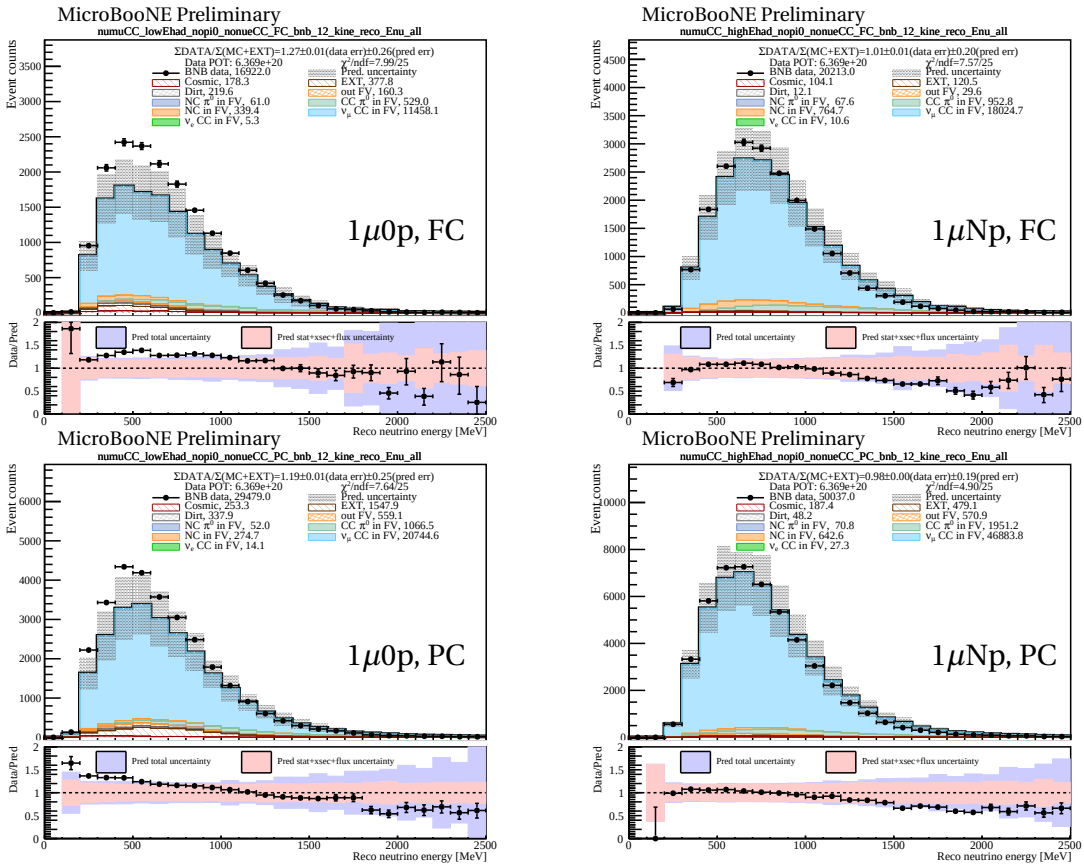

Figure 56: Distribution of reconstructed neutrino energy for ν_μ CC events. Left: without protons. Right: with one or more protons. Top: fully contained events. Bottom: partially contained events. The bottom panels in each sub-figure present the data/pred ratios and the systematic uncertainties. The pink band represents the MC stat, flux, and cross section uncertainties, and the purple band represents an addition of detector systematic uncertainty.

More investigations were performed to verify the $0p$ enhancement. Figure 57 presents

the number of all track-like particles including primary muons, protons, or charged pions. A proton track requires a kinematic energy > 35 MeV, i.e. track length > 1cm, and a charged pion requiring kinematic energy > 10 MeV. This figure confirms the excess is mostly in the 1-track bin where there are only primary muons in each event.

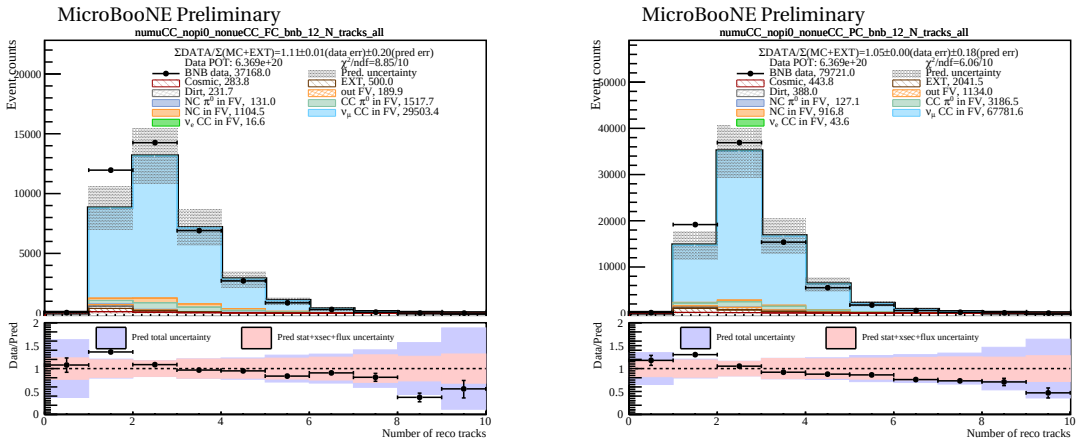

Figure 57: Distribution of the number of track-like particles for ν_μ CC candidate events. Each event must have a primary muon track and other tracks like protons (requiring kinematic energy > 35 MeV, i.e. track length > 1cm) or charged pions (requiring kinematic energy > 10 MeV). Left: fully contained events. Right: partially contained events.

Various plots about the prominent kinematic variables (muon energy and angles, 4-momentum transfer Q^2, and Bjorken variable x_{bj}) are shown in Fig. 58, Fig. 59, Fig. 60, Fig. 61, and Fig. 62, respectively. The hotspot of the excess or deficit in $0p$ or Np channels is in the low Q^2 region which corresponds to forward-going muons. For the Np channels, the deficit in data for the most forward-going muons has also been observed in the MicroBooNE cross section measurements [32, 33, 34].

Figure 63 shows the reconstructed hadronic energy (energy transfer/difference between incoming neutrino energy and outgoing muon energy) distribution for ν_μ CC candidate events. As is seen in data sets from other experiments [35, 36], an excess can be seen in the low hadronic energy region and this is consistent with the observation of $0p$ excess. More validations on energy reconstruction can be found in Sec. 8.5.

As a sanity check, dedicated hand-scans on $0p$ events were conducted on both BNB data and Monte-Carlo samples. We scanned 73 data events and 50 Monte Carlo events which have roughly equal POTs. We found about 12 events in each sample which appeared to have one or more >35 MeV protons in the reconstructed view, verifying that the observed excess comes from the $0p$ events that have no proton visible by eye. Bee display of these BNB events can be found in `https://www.phy.bnl.gov/twister/bee/set/6ca94583-0910-4a6f-90a8-ace1236edf07/event/list/` (data) and `https://www.phy.`

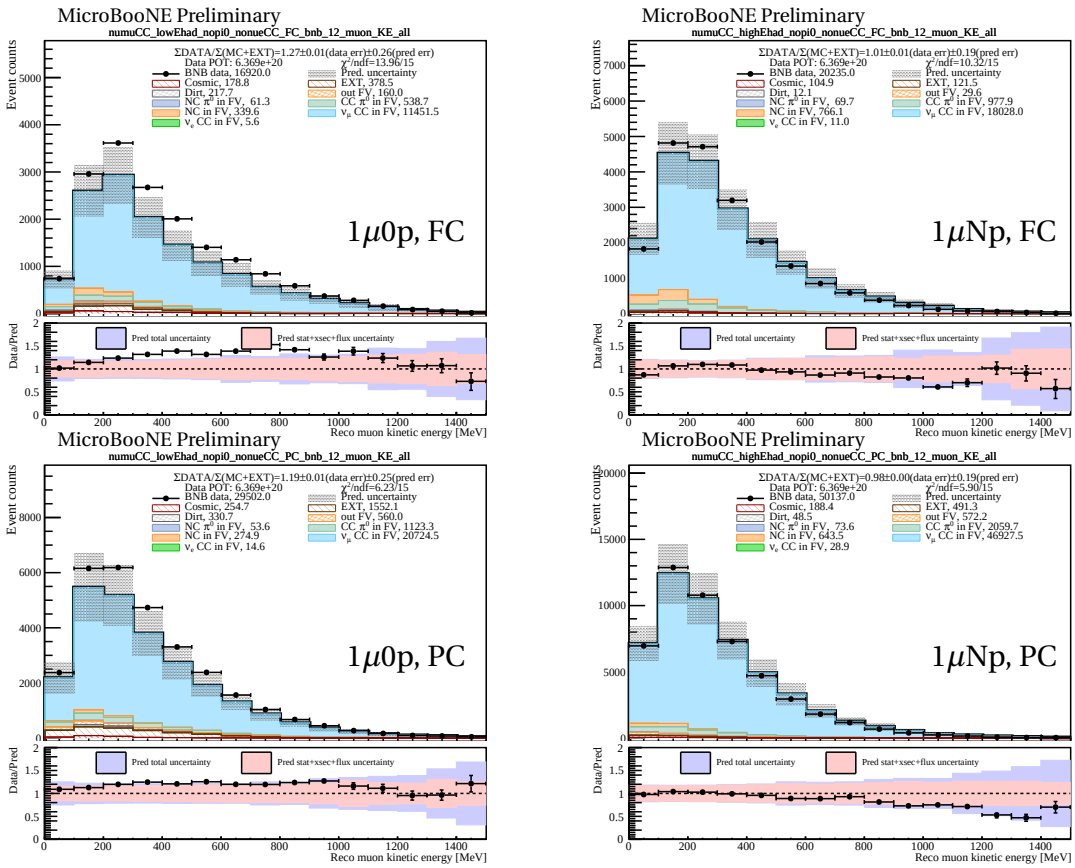

Figure 58: Distribution of reconstructed muon kinematic energy for ν_μ CC candidate events. Left: without protons. Right: with one or more protons. Top: fully contained events. Bottom: partially contained events.

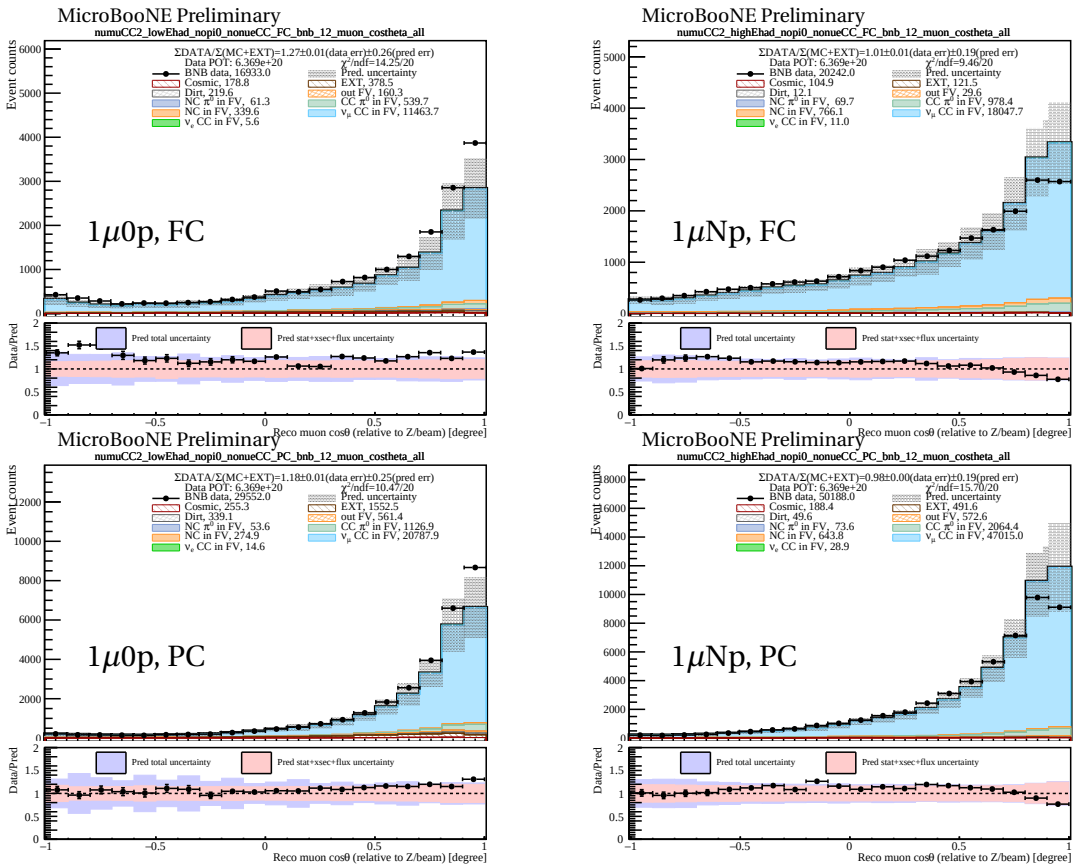

Figure 59: Distribution of cosθ of reconstructed muons for ν_μ CC candidate events. θ is the polar angle relative to the neutrino beam/incoming direction. Left: without protons. Right: with one or more protons. Top: fully contained events. Bottom: partially contained events.

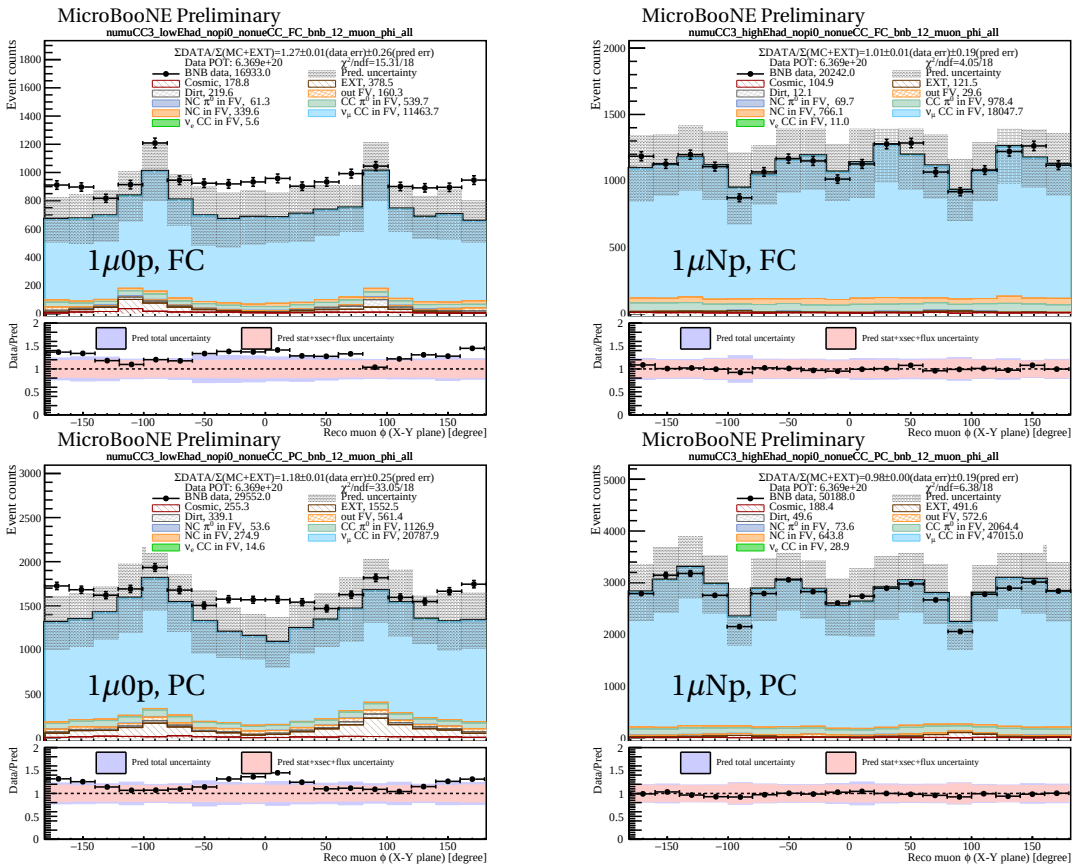

Figure 60: Distribution of ϕ of reconstructed muons for ν_μ CC candidate events. ϕ is the azimuth angle on the transverse plane w.r.t. to the neutrino beam direction. Left: without protons. Right: with one or more protons. Top: fully contained events. Bottom: partially contained events.

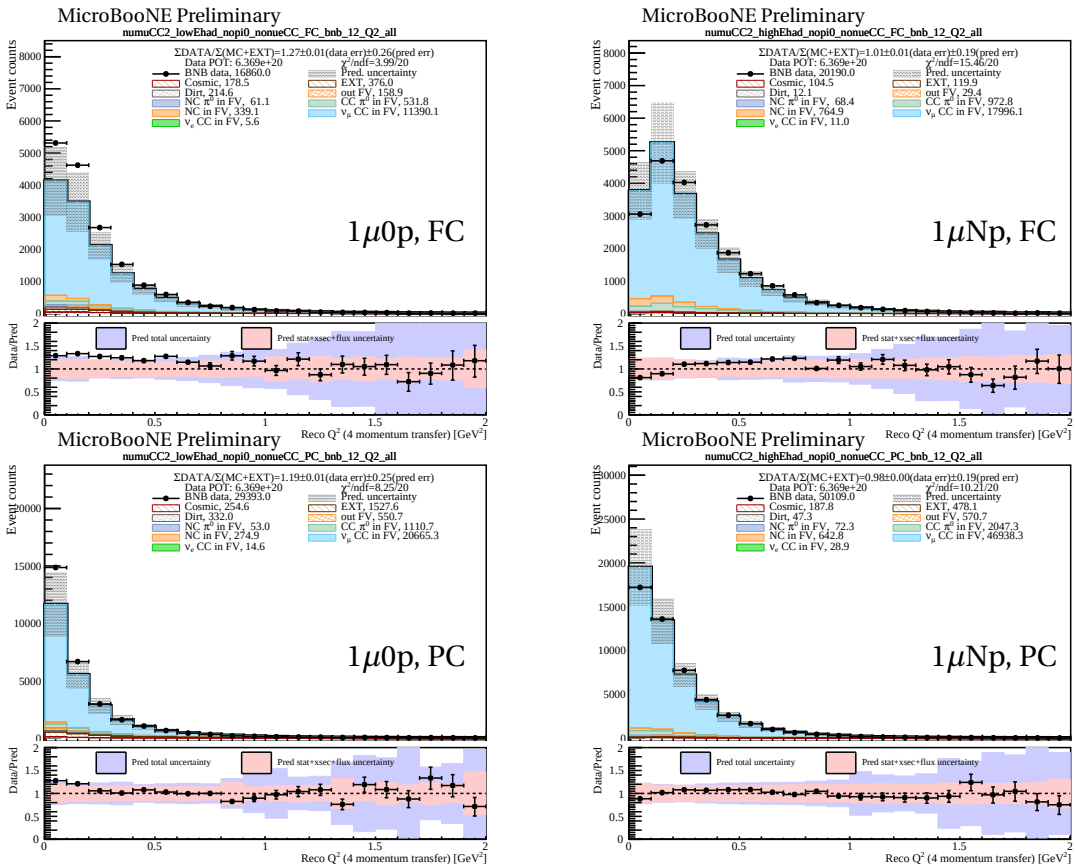

Figure 61: Distribution of the reconstructed four-momentum transfer Q^2 for ν_μ CC candidate events. Left: without protons. Right: with one or more protons. Top: fully contained events. Bottom: partially contained events.

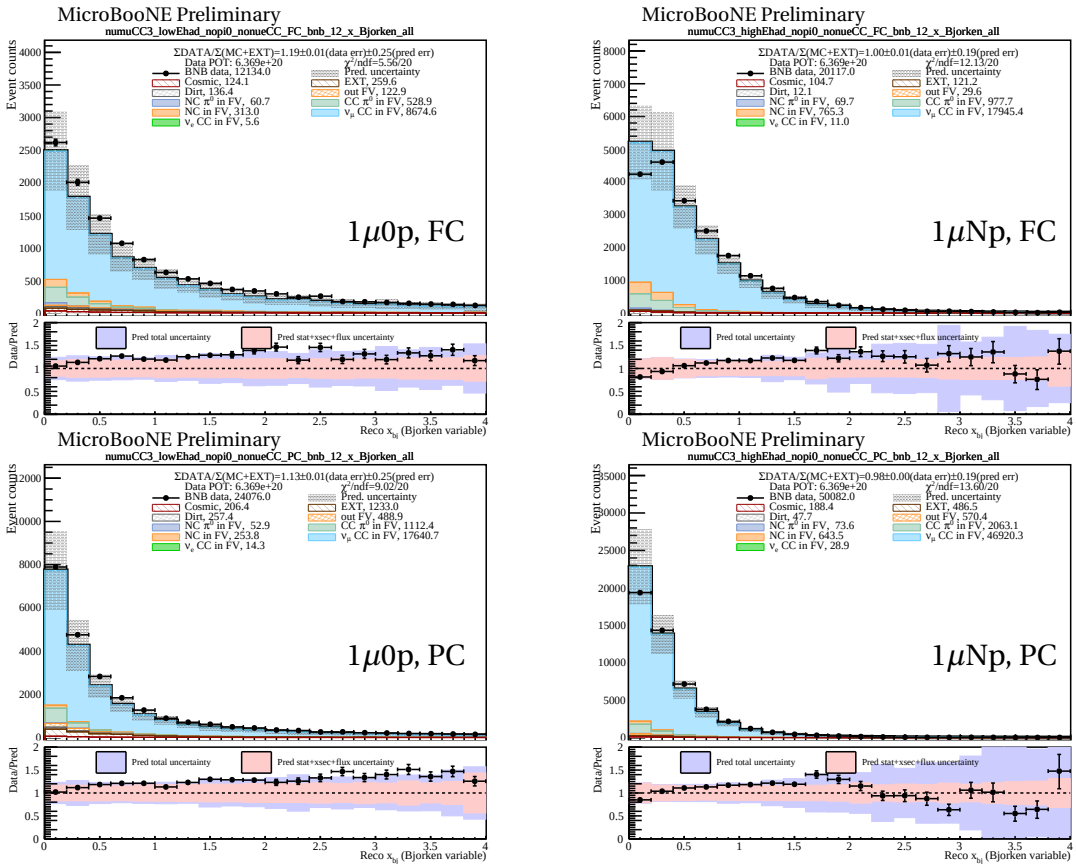

Figure 62: Distribution of the reconstructed Bjorken variable for ν_μ CC candidate events. Left: without protons. Right: with one or more protons. Top: fully contained events. Bottom: partially contained events.

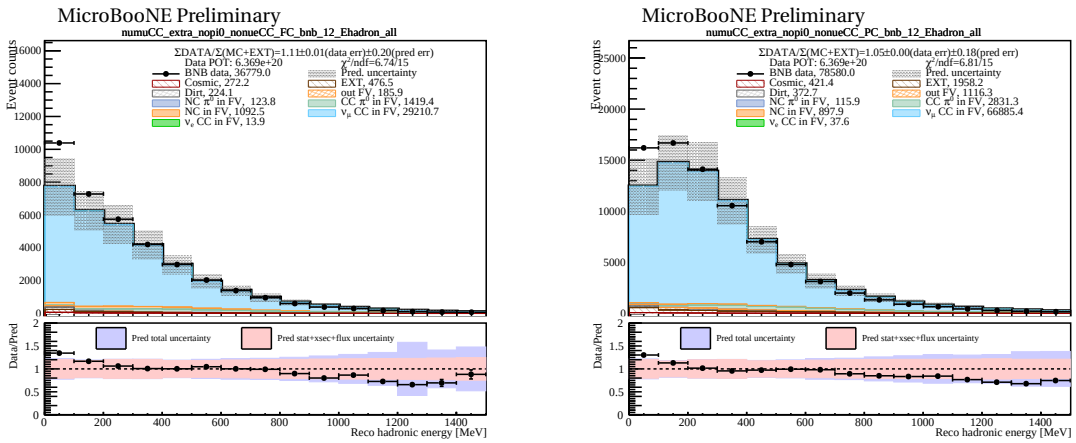

Figure 63: Distribution of reconstructed hadronic energy (energy transfer/difference between reconstructed neutrino energy and primary muon energy) for ν_μ CC candidate events. Left: fully contained events. Right: partially contained events.

`bnl.gov/twister/bee/set/c151f1ec-23cc-4561-b6a1-da1d3c5d88d4/event/list/` (Monte-Carlo).

8.4.1 Validation of the Overall Model with Goodness-of-Fit Tests

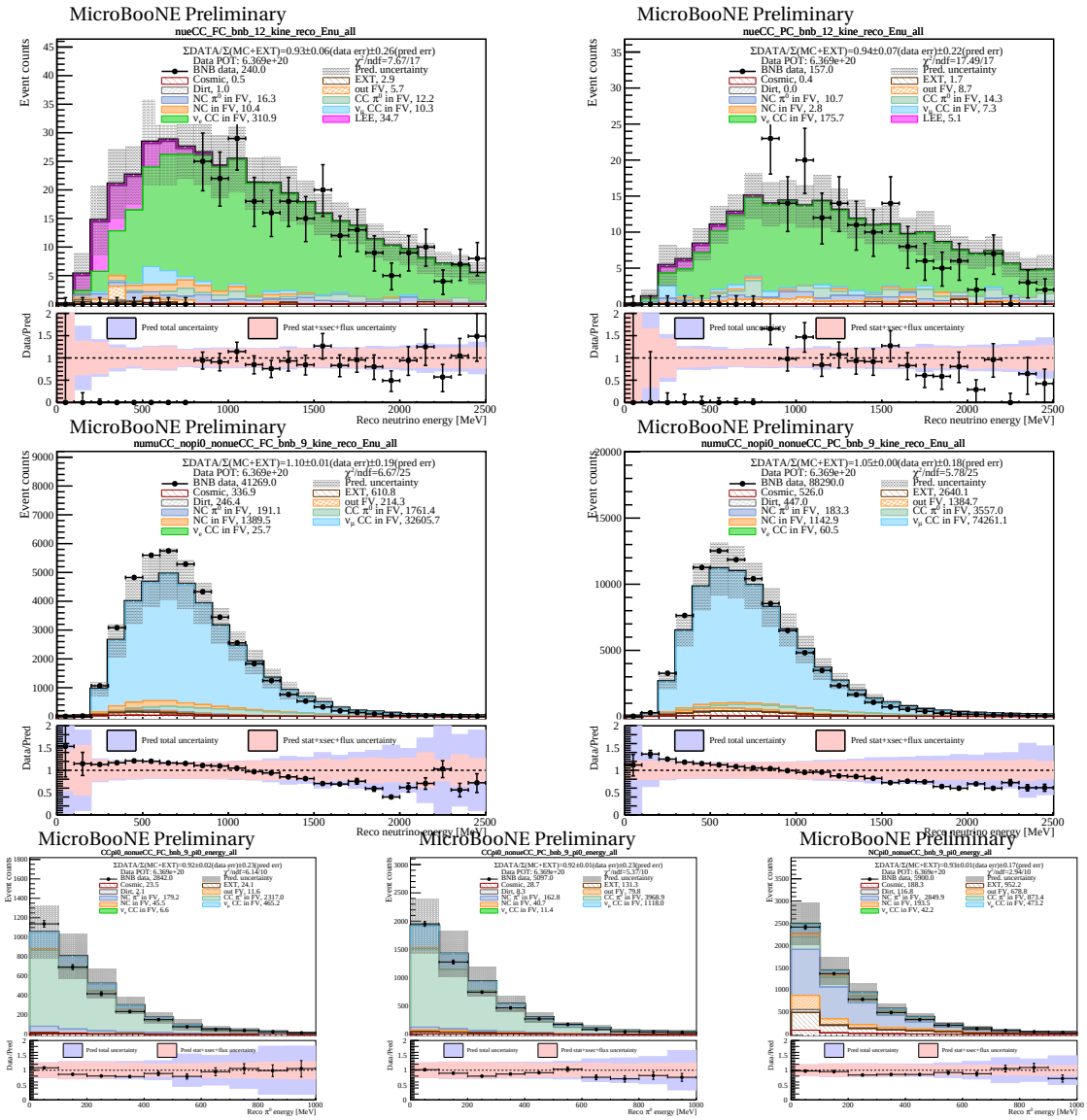

Figure 64: Distribution of 7-channel selection results from far sideband assuming SM ($LEEx = 1$): (from left to right, top to bottom) fully contained ν_e CC, partially contained ν_e CC, fully contained ν_μ CC, partially contained ν_μ CC, fully contained CC π^0, partially contained CC π^0, and NC π^0. The bottom panels in each sub-figure present the data/pred ratios and the systematic uncertainties. The pink band represents the MC stat, flux, and cross section uncertainties, and the purple band represents an addition of detector systematic uncertainty.

Figure 64 shows the Distribution of 7-channel selection results from far sideband assuming SM ($LEEx = 0$). The data points of ν_eCC channels below 800 MeV are blinded. The goodness-of-fit (GoF) test for the ν_μCC channels is shown in Fig. 65. The GoF value demonstrates that the data is consistent with MC prediction within uncertainties. The GoF test for the three π^0 channels are shown in Fig 66. The GoF values demonstrate that the data is consistent with MC prediction within uncertainties after applying constraints from ν_μCC channels. The GoF tests for the two ν_eCC channels are shown in Fig. 67 (separate GoF test) and Fig. 68 (combined GoF test). The GoF values demonstrate that the data is consistent with MC prediction within uncertainties after applying constraints from ν_μCC channels.

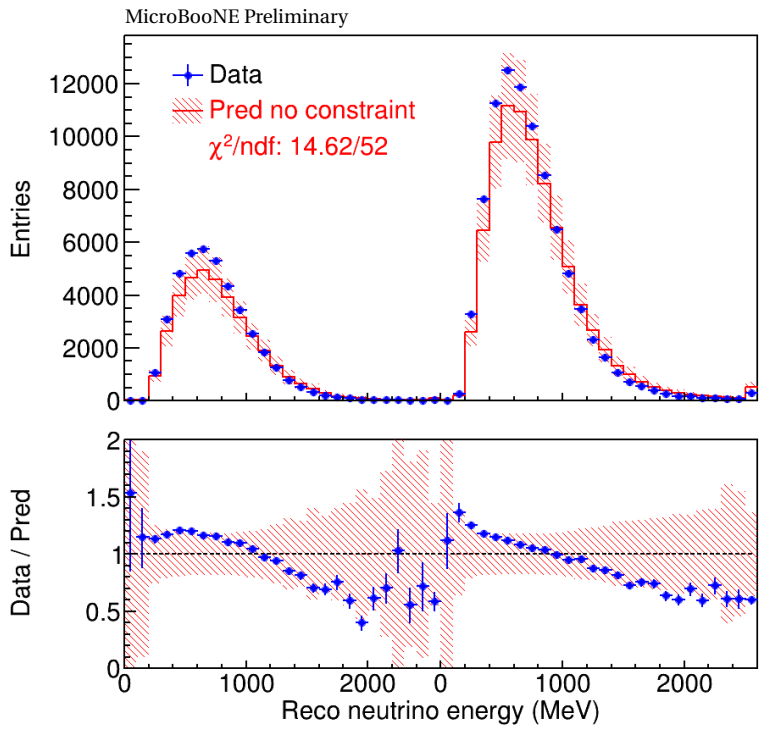

Figure 65: Goodness-of-fit test of ν_μCC channels.

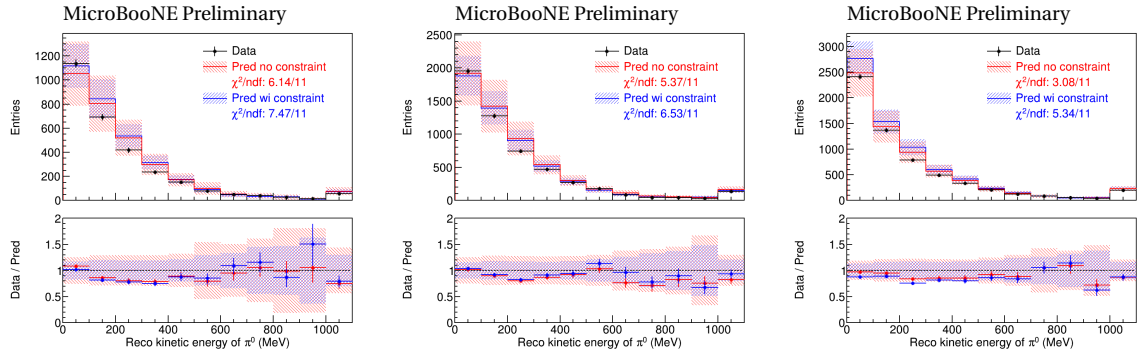

Figure 66: Goodness-of-fit test of π^0 channels (left: CCπ^0 FC, middle: CCπ^0 PC, right: NCπ^0) before and after ν_μCC constraints. The red (blue) histogram and red (blue) error band represent the MC prediction and its uncertainties before (after) applying ν_μCC constraints.

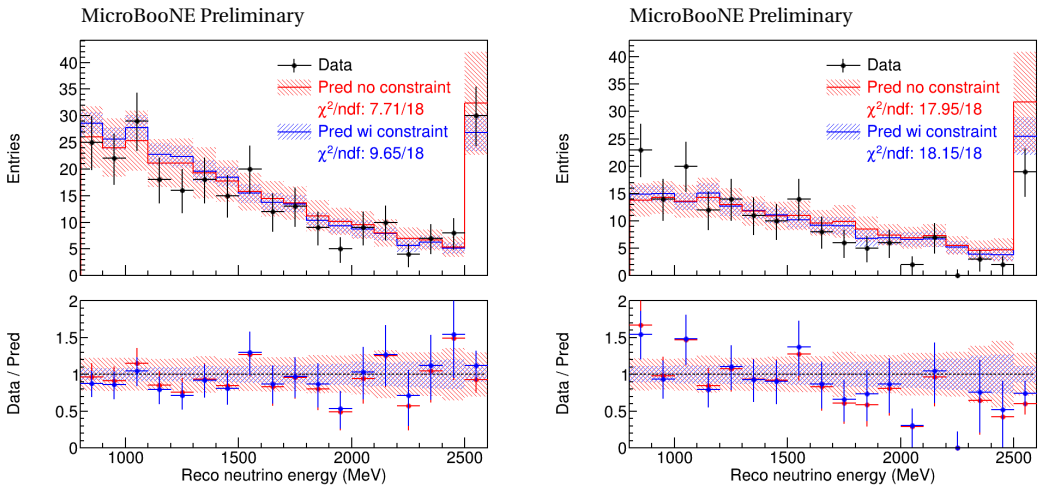

Figure 67: Goodness-of-fit tests of FC ν_eCC (left) and PC ν_eCC (right) channels. The red (blue) histogram and red (blue) error band represent the MC prediction and its uncertainties before (after) applying ν_μCC and π^0 constraints.

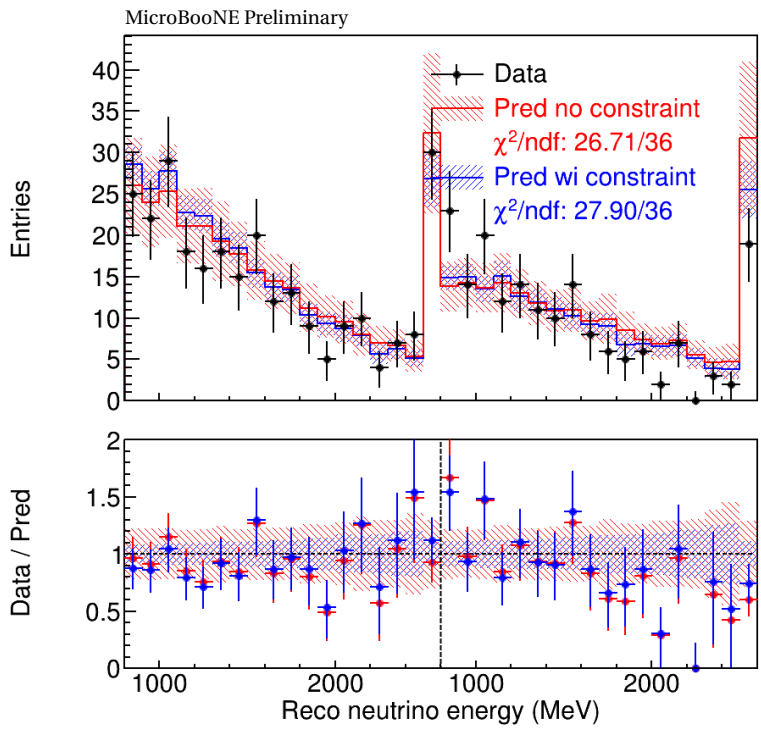

Figure 68: Goodness-of-fit tests of combined FC ν_eCC (left) and PC ν_eCC (right) channels. The red (blue) histogram and red (blue) error band represent the MC prediction and its uncertainties before (after) applying ν_μCC and π^0 constraints.

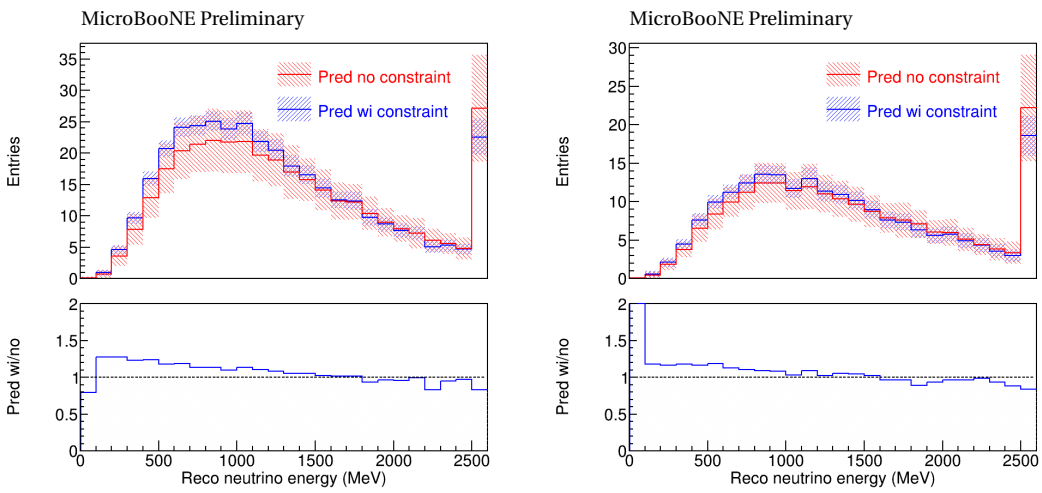

Figure 69: Constraint results of ν_eCC FC (left) and PC (right) signal only. The red (blue) histogram and red (blue) error band represent the MC prediction and its uncertainties before (after) applying ν_μCC, CCπ^0 and NCπ^0 constraints. The bottom panel shows the ratio before and after the constraint.

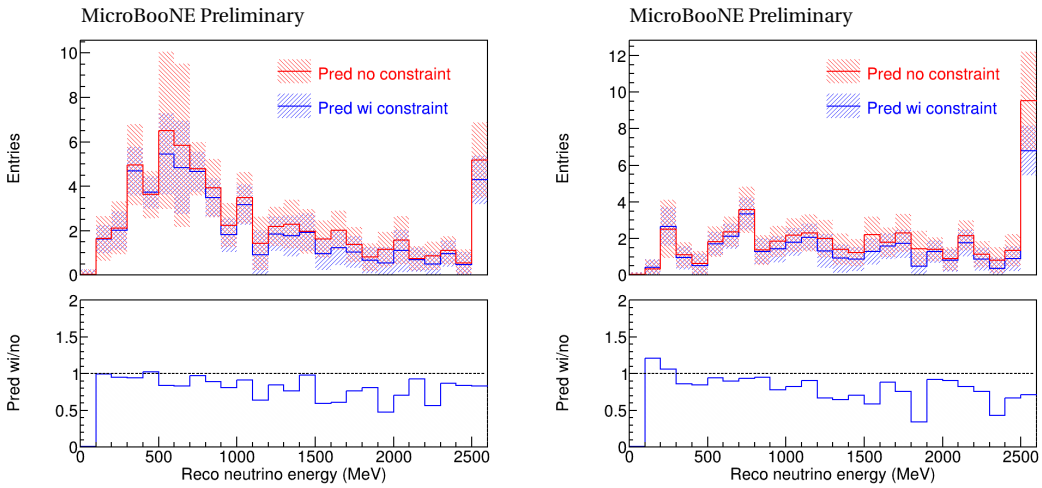

Figure 70: Constraint results of ν_eCC FC (left) and PC (right) background only. The red (blue) histogram and red (blue) error band represent the MC prediction and its uncertainties before (after) applying ν_μCC, CCπ^0 and NCπ^0 constraints. The bottom panel shows the ratio before and after the constraint.

We also look at the constraint results of ν_eCC for two scenarios: ν_eCC signal only; and the background only. The constraints are from the ν_μCC, CCπ^0 and NCπ^0 channels. Figure 69 shows the results of ν_eCC signal only. At the low energy region, the MC prediction is enhanced after the constraints, which is consistent with the fact that ν_μCC data is higher than the MC prediction at the low energy region. Figure 70 shows the results of (ν_eCC) background only. Generally, the MC prediction is suppressed after the constraint, which is consistent with the π^0s observation where the data is systematically lower than the the MC prediction. These results are used in Sec. 9 to estimate the LEE physics sensitivity.

8.5 Validations of neutrino energy reconstruction

Beside the general data/MC comparison, for the eLEE search, another important validation is on the modeling of the conversion from true to the reconstructed neutrino energy. Figure 71 shows the comparison between data and prediction as a function of the reconstructed muon energy E_μ^{rec} for both fully contained (FC) and partially contained (PC) inclusive ν_μCC candidate events. The GoF (χ^2/NDF) is below unity in both cases showing good agreement between data and model prediction.

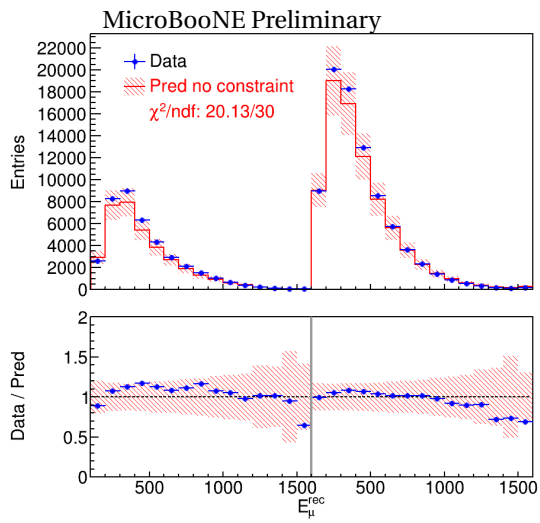

Figure 71: Comparison between data and prediction as a function of E_μ^{rec}: The statistical, cross section, flux, and detector systematic uncertainties are included in the bands. The first 15 bins with 100 MeV per bin correspond to the fully contained events from 0.1 GeV to 1.6 GeV. The 16th bin is the overflow bin corresponding to fully contained events above 1.6 GeV. The next 15 bins with 100 MeV per bin correspond to the partially contained events from 0.1 GeV to 1.6 GeV. The last bin is the overflow bin corresponding to the partially contained events above 1.6 GeV.

Figure 72 shows the comparison between data and prediction as a function of the reconstructed muon angle $\cos\theta_\mu^{rec}$ for both fully contained (FC) and partially contained (PC) channels. The GoF is below unity showing good agreement between data and model prediction. Note, we observed an overall data excess in the $1\mu 0pX\pi$ channel and a data deficit in the $1\mu NpX\pi$ forward-going $\cos\theta_\mu^{rec}$ ~1 region, and the observation in inclusive ν_μCC selection is a result from different proportions of $1\mu 0pX\pi$ and $1\mu NpX\pi$ components in the FC and PC samples.

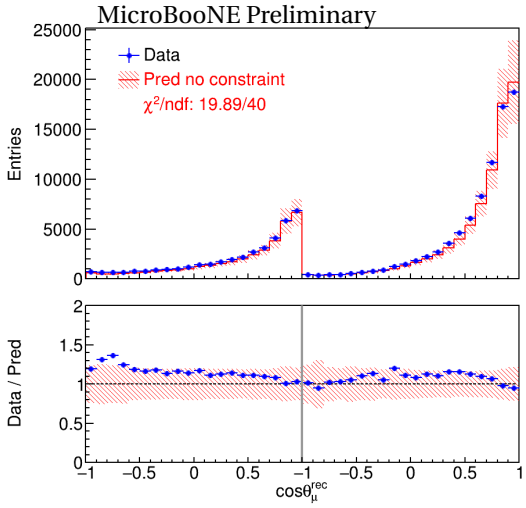

Figure 72: Comparison between data and prediction as a function of $\cos\theta_{\mu}^{rec}$ (relative to Z/beam). The statistical, cross section, flux, and detector systematic uncertainties are included in the bands. The first 20 bins correspond to the fully contained events covering from -1 to 1. The next 20 bins correspond to the partially contained events covering from -1 to 1.

Figure 73 shows the comparison between data and prediction as a function of the reconstructed energy of the hadronic system E_{had}^{rec}. The GoF is below unity showing good agreement between data and model prediction. We should further note that the data of the lowest E_{had}^{rec} bin is above the prediction and outside the uncertainty band. This difference is consistent with the fact that data are systematically higher than the prediction at $1\mu 0p$ channel. Since the E_{had}^{rec} is low for these events, it is natural to raise the question whether the model describes the missing energy because of neutrons or low-energy gammas well. We will show the current model is sufficient in describing the observations in data with conditional covariance matrix in the following.

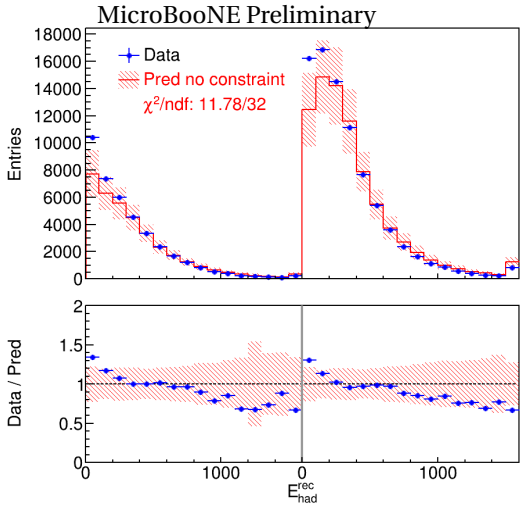

Figure 73: Comparison between data and prediction as a function of E_{had}^{rec}. The statistical, cross section, flux, and detector systematic uncertainties are included in the bands. The first 15 bins with 100 MeV per bin correspond to the fully contained events from 0 GeV to 1.5 GeV. The 16th bin is the overflow bin corresponding to fully contained events above 1.5 GeV. The next 15 bins with 100 MeV per bin correspond to the partially contained events from 0 GeV to 1.5 GeV. The last bin is the overflow bin corresponding to the partially contained events above 1.5 GeV.

Using the conditional covariance matrix (introduced in Sec. 6), we demonstrate that the difference between the modeling of the missing energies (because of neutrons or low-energy gammas or activities outside TPC) and that in real data is within the quoted cross section systematic uncertainties.

For PC events, the reconstructed (neutrino, muon, hadronic) energy only takes into account the visible part of the system inside the active TPC volume. The conversion between the true energy and the reconstructed energy thus has stronger dependence on the overall model. Therefore, it is crucial to perform dedicated validations on the modeling of missing energy. Since the missing energy is invisible by definition, the validation can only be performed on the reconstructed energy. As shown in the previous section, the direct comparison of the PC distributions with the overall model yields good GoF values indicating consistent results. However, these tests include all sources of systematics, which may hide the potential discrepancies on the modeling of missing energy for the PC events. To validate the modeling of the missing energy for the PC events, we perform a more stringent test: calculate GoF of the PC ν_μCC distributions after constraining the FC ν_μCC distributions. In this case, the common systematic uncertainties to the PC and FC channels are largely cancelled, and a more stringent validation on the modeling of missing energy of PC events can be achieved.

Figure 74 shows the comparison between data and prediction as a function of E_μ^{rec} for

the PC events. After applying the constraints from the FC sample, the uncertainties of the prediction are significantly reduced. Nevertheless, the GoF values are still reasonable, indicating that the model describes the difference between FC and PC events very well. Figure 75 shows the comparison between data and prediction as a function of $\cos\theta_{\mu}^{rec}$ for the PC events. The GoF values (e.g. GoF = 15.09/20 with a p-value of 0.23) after applying constraints are still reasonable, indicating that the model describes the difference between FC and PC events well. We should note at the most forward muon angle, the prediction after constraints is enhanced, which slightly increase the difference between data and prediction. This change is the result of the fact that the data is higher than prediction in this bin for the FC events. Figure 76 shows the comparison between data and prediction as a function of E_{had}^{rec} for the PC events. The GoF values after applying constraints are still reasonable. In particular, we should note the prediction at the lowest bin of E_{had}^{rec} is enhanced after applying the constraints from the FC sample. This is expected since a similar behaviour is observed in the FC sample.

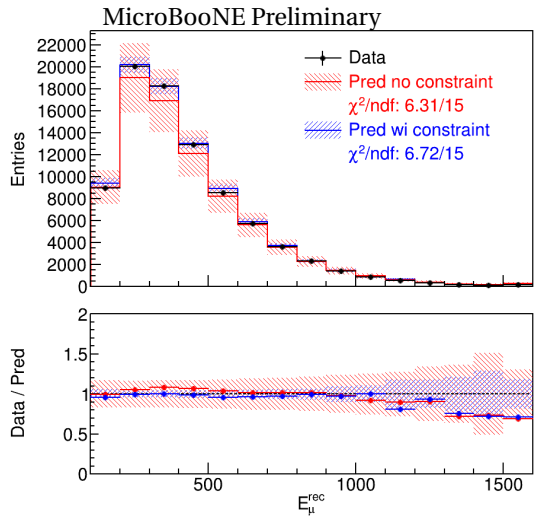

Figure 74: Comparison between data and prediction as a function of E_{μ}^{rec} for the partially contained events. The red (blue) lines and bands show the prediction without (with) the constraints from the fully contained event sample. The statistical, cross section, flux, and detector systematic uncertainties are included in the bands. The first 15 bins for 100 MeV per bin covers from 0.1 GeV to 1.6 GeV. The last bin is the overflow bin for events above 1.6 GeV.

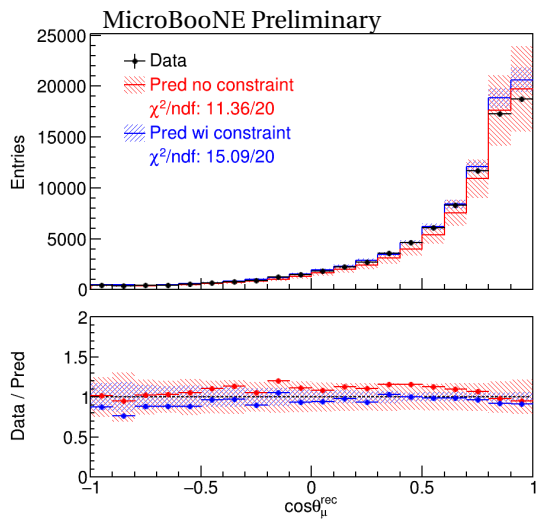

Figure 75: Comparison between data and prediction as a function of reconstructed muon angle $\cos\theta_{\mu}^{rec}$ (relative to Z/beam). The red (blue) lines and bands show the prediction without (with) the constraints from the fully contained event sample. The statistical, cross section, flux, and detector systematic uncertainties are included in the bands. The 20 bins covers from -1 to 1.

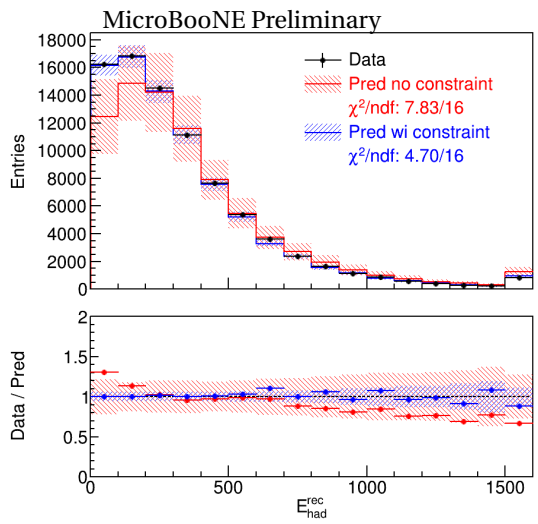

Figure 76: Comparison between data and prediction as a function of the E_{had}^{rec}. The red (blue) lines and bands show the prediction without (with) the constraints from the fully contained event sample. The statistical, cross section, flux, and detector systematic uncertainties are included in the bands. The first 15 bins correspond to 0 GeV to 1.5 GeV. The last bin correspond to overflow bin above 1.5 GeV.

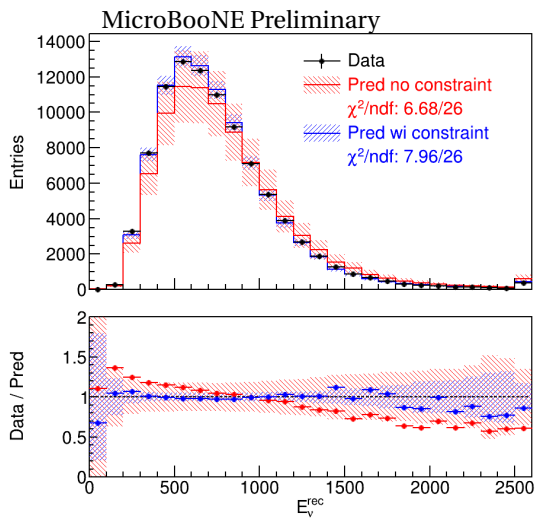

Figure 77: Comparison between data and prediction as a function of E_ν^{rec}. The red (blue) lines and bands show the prediction without (with) the constraints from the fully contained event sample. The statistical, cross section, flux, and detector systematic uncertainties are included in the bands. The first 25 bins with 100 MeV per bin correspond to the fully contained events from 0 GeV to 2.5 GeV. The 26th bin is the overflow bin corresponding to fully contained events above 2.5 GeV.

Finally, Fig. 77 shows the comparison between data and prediction as a function of E_ν^{rec} for the PC events. After applying the constraints from the FC sample, the uncertainties of the prediction are significantly reduced. Nevertheless, the GoF values are still reasonable, indicating that the model describes the difference between FC and PC events very well. With these results, we demonstrate that the model with its associated uncertainties can describe the difference between the PC and FC events (i.e. the missing energy that are outside the TPC active volume) well.

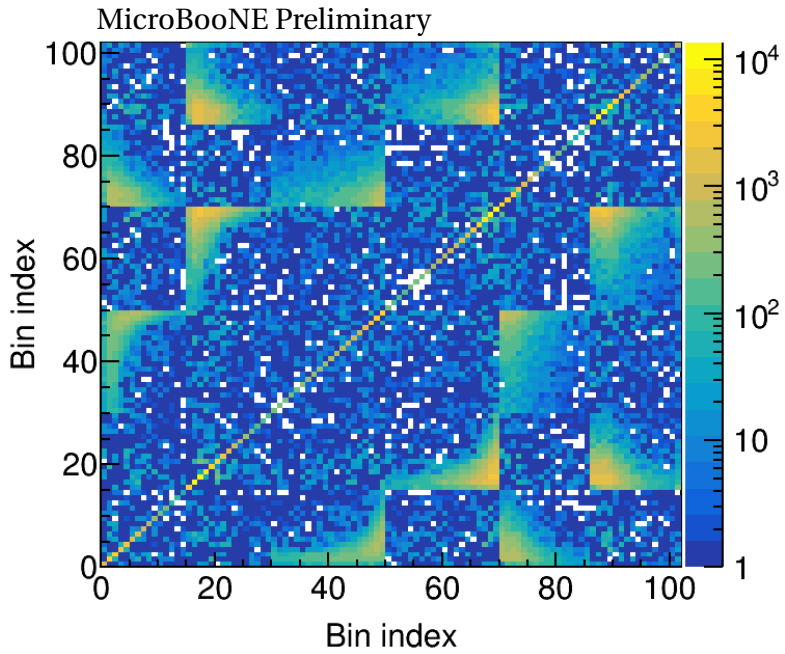

Figure 78: Statistical covariance matrix constructed with the bootstrapping method [37]. Six blocks corresponding to i) FC ν_μCC E_μ distribution, ii) PC ν_μCC E_μ distribution, iii) FC ν_μCC $\cos\theta_\mu$ distribution, iv) PC ν_μCC $\cos\theta_\mu$ distribution, v) FC ν_μCC E_{had} distribution, and vi) PC ν_μCC E_{had} distribution are shown. 5000 universes are used. There is no clear correlation between the FC and PC channels. For the same FC (PC) events, there is a strong correlation between different kinematic variables.

Similar to the situation of PC events, the reconstructed energy of the hadronic system E^{rec}_{had} cannot be directly mapped to the energy transfer to the Argon system, since some of the energy going into neutrons or low energy photons can be lost. In this case, the mapping of reconstructed to true hadronic energy would rely on the overall model, particularly the cross section model. To study the impact of such missing energy, a similar strategy using the conditional covariance matrix is adopted. We examine the E^{rec}_{had} distribution after constraining the muon kinematics. In particular, we consider two one-dimensional muon kinematics: E^{rec}_{μ} and θ^{rec}_{μ}. If there is a new mechanism changing the behaviour of the missing energy in the hadronic system beyond the current model, a constraint in the muon kinematics (or distribution) will not change the data/MC difference in the distribution on E^{rec}_{had}, and the GoF will become much worse. For this examination, we use the bootstrapping method to estimate the correlated statistical uncertainties since the E^{rec}_{had} and $E^{rec}_{\mu}/\theta^{rec}_{\mu}$ distributions are from the same set of events. Figure 78 shows the statistical covariance matrix constructed with the bootstrapping method.

Figure 79 shows the comparison between data and prediction as a function of E^{rec}_{had} for both FC and PC events. After applying the constraints from the E^{rec}_{μ} distribution, the uncertainties of the prediction are significantly reduced. Nevertheless, the GoF values improve,

indicating that the model describes the relation between E_{had}^{rec} and E_{μ}^{rec} very well. In particular, we note the prediction at the lowest bin of E_{had}^{rec} is enhanced after applying the constraints from the E_{μ}^{rec} distribution. In another word, the differences between data and prediction in the E_{had}^{rec} distributions are significantly reduced, once the differences between data and prediction in the E_{μ}^{rec} distributions are eliminated within the allowed range of the model predictions.

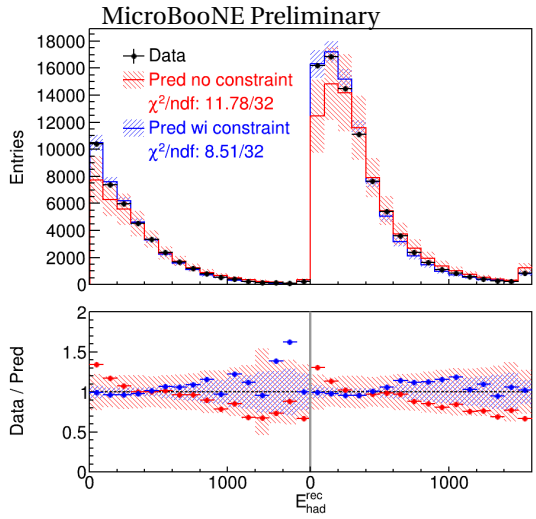

Figure 79: Comparison between data and prediction as a function of E_{had}^{rec}. The red (blue) lines and bands show the prediction without (with) the constraints from the distributions as a function of E_{μ}^{rec}. The statistical, cross section, flux, and detector systematic uncertainties are included in the bands. The first 15 bins with 100 MeV per bin correspond to the fully contained events from 0 GeV to 1.5 GeV. The 16th bin is the overflow bin corresponding to fully contained events above 1.5 GeV. The next 15 bins with 100 MeV per bin correspond to the partially contained events from 0 GeV to 1.5 GeV. The last bin is the overflow bin corresponding to the partially contained events above 1.5 GeV.

To further examine the E_{had}^{rec} distributions, we apply the constraints from the distributions of reconstructed muon angle. First, Fig. 80 shows the comparison between data and prediction as a function of $\cos\theta_{\mu}^{rec}$ for both FC and PC events. After applying the constraints from the E_{μ}^{rec} distribution, the uncertainties of the prediction are significantly reduced, and the GoF value is still reasonable indicating that the model describes the relation between θ_{μ}^{rec} and E_{μ}^{rec} very well. The differences between data and prediction in the $\cos\theta_{\mu}^{rec}$ distributions are significantly reduced, once the difference between data and prediction in the E_{μ}^{rec} distributions are eliminated within the allowed range of the model predictions.

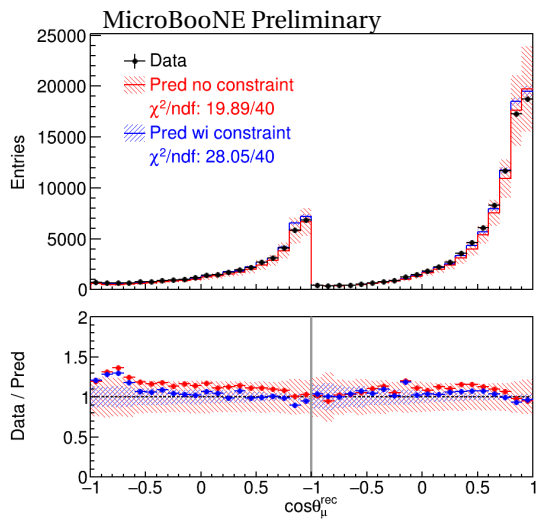

Figure 80: Comparison between data and prediction as a function of $\cos\theta_\mu^{rec}$ (relative to Z/beam). The red (blue) lines and bands show the prediction without (with) the constraints from the reconstructed muon energy E_μ^{rec}. The statistical, cross section, flux, and detector systematic uncertainties are included in the bands. The first 20 bins correspond to the fully contained events covering from -1 to 1. The next 20 bins correspond to the partially contained events covering from -1 to 1.

Next, we add the constraints from the distributions of reconstructed muon angle. Figure 81 shows the comparison between data and prediction as a function of E_{had}^{rec} for both FC and PC events. After applying the constraints from the E_μ^{rec} and $\cos\theta_\mu^{rec}$ distributions, the uncertainties of the prediction are significantly reduced. Nevertheless, the GoF values improve indicating that the model describes the relation between E_{had}^{rec} and the muon kinematics very well. In particular, we note the prediction at the lowest bin of E_{had}^{rec} is enhanced after applying the constraints.

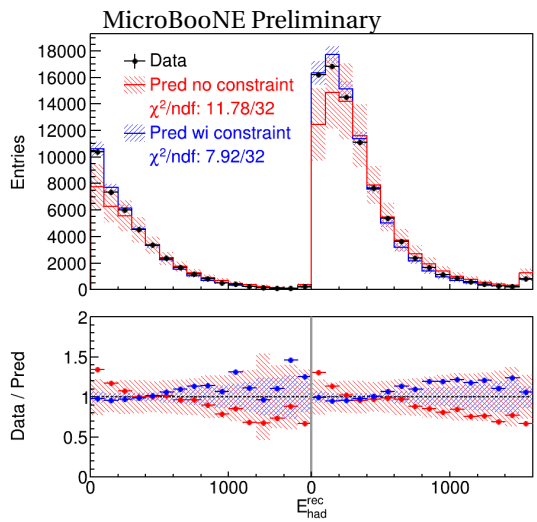

Figure 81: Comparison between data and prediction as a function of E_{had}^{rec}. The red (blue) lines and bands show the prediction without (with) the constraints from the reconstructed muon energy E_{μ}^{rec} and angle $\cos\theta_{\mu}^{rec}$. The statistical, cross section, flux, and detector systematic uncertainties are included in the bands. The first 15 bins with 100 MeV per bin correspond to the fully contained events from 0 GeV to 1.5 GeV. The 16th bin is the overflow bin corresponding to fully contained events above 1.5 GeV. The next 15 bins with 100 MeV per bin correspond to the partially contained events from 0 GeV to 1.5 GeV. The last bin is the overflow bin corresponding to the partially contained events above 1.5 GeV.

With these results, we demonstrate that the model with its associated uncertainties can describe the difference between the E_{had}^{rec} and the energy transfer to the argon nuclei $\nu = E_{\nu} - E_{\mu}$ (i.e. the missing energy associated with neutrons and low-energy gamma) well. We further elaborate on this point below. At a fixed true neutrino energy, the energy transfer to the Argon nuclei is associated with the muon kinematics. The difference between the energy transfer and the energy of the hadronic system is the missing energy. If the modeling of the missing energy with its uncertainties is incorrect, one would expect to see differences between data and predictions in the E_{had}^{rec} distributions after applying the constraints on the muon kinematics. Since we did not see such discrepancies in the E_{had}^{rec} distributions after applying constraints on the muon kinematics, we conclude that the current modeling of the missing energy because of neutrons and low-energy gammas is sufficient. These validations on the overall model provide a solid foundation in modeling the conversion from true neutrino energy to the reconstructed neutrino energy.

9 eLEE SENSITIVITIES

In this section, we present the eLEE sensitivities based on the Asimov data set following the procedure outlined in Ref. [38]. 6.37e+20 POT dataset is considered, which is equivalent to Run1-3 results combined.

As mentioned in Sec. 1, the alternative hypothesis $eLEEx = 1$ for the sensitivity estimation is formed based on central value of a model of a potential anomalous enhancement in the rate of intrinsic ν_eCC events at true neutrino energies less than 800 MeV with a fixed spectral shape. The model is obtained by unfolding the observed excess of electron-like events in MiniBooNE to true neutrino energy under a CCQE hypothesis and applying that prediction directly to the rate of intrinsic ν_eCC events expected in MicroBooNE, and no systematic uncertainty is assumed on the model [14] while it shares the same uncertainty with intrinsic nue events considering a full correlation.

As shown in the analysis of the open data (Sec. 6) and the far side band data (Sec. 8), the ν_μCC result, which is not limited by statistics in data, is higher than that of the nominal prediction. Given the positive correlation between the ν_μCC and ν_eCC channels, we expect the prediction of ν_eCC is enhanced after applying the constraints of ν_μCC (see Fig. 69). Therefore, we estimate the physics sensitivity after enhancing (suppressing) the nominal ν_eCC signal (background) prediction by the ratio shown in Fig. 69 for signal (Fig. 70 for background). These results, tabulated in Table 1, represent the physics sensitivity after considering the observed data/MC channels in the ν_μCC and π^0 channels, with the systematic uncertainties described in Sec. 5

Data POT	Null hypothesis: SM	Null hypothesis $eLEEx = 1$
6.37e+20	4.7σ	3.3σ

Table 1: Sensitivity to reject SM (or $eLEEx = 1$) assuming $eLEEx = 1$ (or SM) being true using the Asimov data set and taking into account the current observation of ν_μCC in the BNB far side band data.

With the null hypothesis being SM ($eLEEx = 1$), the truth of $eLEEx = 1$ (SM) is assumed to be the Asimov data set. The ν_eCC signal to background ratio is higher when the truth is $eLEEx = 1$ than the case when the truth is SM. Therefore, it is expected that one would hit the limitation of background systematics quicker for the case of null hypothesis being $eLEEx = 1$.

10 SUMMARY

This technote summarizes the the current status of Wire-Cell eLEE analysis effort in MicroBooNE. With the BNB open data at 5.3e19 POT, BNB far side band data at 6.37e20 POT, and NuMI data at 2.10e20 POT, a good data/MC consistency has been demonstrated for both ν_μCC and ν_eCC events on various variables. The reconstruction of neutrino energy and the overall model including all systematic uncertainties are validated for the upcoming eLEE search and cross section extraction. The robustness and the validity of the MicroBooNE Wire-Cell eLEE analysis strategy and method are demonstrated. We expect to have a 4.7σ (3.3σ) physics sensitivity to reject SM ($eLEEx = 1$) hypothesis at 6.37e+20 POT data assuming $eLEEx = 1$ (SM) hypothesis being true.

A GLOSSARY OF VARIOUS FINAL STATES

- $1\mu 0p$: 1 muon and no proton, with any number of pions in a final state. This is equivalent to $1\mu 0pX\pi$, where X is X≥0.
- $1\mu Np$: 1 muon and 1 or more protons, with any number of pions in a final state. This is equivalent to $1\mu NpX\pi$, where X is X≥0.
- $1e0p$: 1 electron and no proton, with any number of pions in a final state. This is equivalent to $1\mu 0pX\pi$, where X is X≥0.
- $1eNp$: 1 electron and 1 or more protons, with any number of pions in a final state. This is equivalent to $1\mu NpX\pi$, where X is X≥0.

REFERENCES

[1] R. Acciarri et al. Design and Construction of the MicroBooNE Detector. *JINST*, 12(02):P02017, 2017.

[2] P. Abratenko et al. High-performance Generic Neutrino Detection in a LArTPC near the Earth's Surface with the MicroBooNE Detector. 12 2020.

[3] P. Abratenko et al. Cosmic Ray Background Rejection with Wire-Cell LArTPC Event Reconstruction in the MicroBooNE Detector. 1 2021.

[4] P. Abratenko et al. Neutrino Event Selection in the MicroBooNE Liquid Argon Time Projection Chamber using Wire-Cell 3-D Imaging, Clustering, and Charge-Light Matching. 11 2020.

[5] "Booster Neutrino Flux Prediction at MicroBooNE", MicroBooNE public-note 1031, `http://microboone.fnal.gov/wp-content/uploads/MICROBOONE-NOTE-1031-PUB.pdf`.

[6] "Supporting note: Cross-section model and uncertainties", `https://microboone-docdb.fnal.gov/cgi-bin/private/ShowDocument?docid=27018`.

[7] C. Adams et al. Ionization electron signal processing in single phase LArTPCs. Part I. Algorithm Description and quantitative evaluation with MicroBooNE simulation. *JINST*, 13(07):P07006, 2018.

[8] P. Abratenko et al. Measurement of space charge effects in the MicroBooNE LArTPC using cosmic muons. *JINST*, 15(12):P12037, 2020.

[9] C. Adams et al. Calibration of the charge and energy loss per unit length of the MicroBooNE liquid argon time projection chamber using muons and protons. *JINST*, 15(03):P03022, 2020.

[10] "Measurement of the Electronegative Contaminants and Drift Electron Lifetime in the MicroBooNE Experiment", MicroBooNE public note 1003, `http://microboone.fnal.gov/wp-content/uploads/MICROBOONE-NOTE-1003-PUB.pdf`.

[11] C. Adams et al. Ionization electron signal processing in single phase LArTPCs. Part II. Data/simulation comparison and performance in MicroBooNE. *JINST*, 13(07):P07007, 2018.

[12] R. Acciarri et al. Noise Characterization and Filtering in the MicroBooNE Liquid Argon TPC. *JINST*, 12(08):P08003, 2017.

[13] A. A. Aguilar-Arevalo et al. Significant Excess of ElectronLike Events in the MiniBooNE Short-Baseline Neutrino Experiment. *Phys. Rev. Lett.*, 121(22):221801, 2018.

[14] "MicroBooNE low-energy excess signal prediction from unfolding MiniBooNE Monte-Carlo and data", MicroBooNE public note 1043, `http://microboone.fnal.gov/wp-content/uploads/MICROBOONE-NOTE-1043-PUB.pdf`.

[15] Gary J. Feldman and Robert D. Cousins. A Unified approach to the classical statistical analysis of small signals. *Phys. Rev. D*, 57:3873–3889, 1998.

[16] P. Abratenko et al. Cosmic Ray Background Rejection with Wire-Cell LArTPC Event Reconstruction in the MicroBooNE Detector. 1 2021.

[17] PSTAR at NIST: `https://physics.nist.gov/PhysRefData/Star/Text/PSTAR.html`.

[18] P. Abratenko et al. Neutrino Event Selection in the MicroBooNE Liquid Argon Time Projection Chamber using Wire-Cell 3-D Imaging, Clustering, and Charge-Light Matching. 11 2020.

[19] Tianqi Chen and Carlos Guestrin. XGBoost: A Scalable Tree Boosting System. 3 2016.

[20] Monte Carlo Statistical Uncertainties, W. Gu et al., MicroBooNE doc-db 32714.

[21] Detector systematics internal note, A. Ashkenazi et al., MicroBooNE doc-db 27009.

[22] MicroBooNE Flux Uncertainty Implementation, Z. Pavlovich and J. Zennamo, MicroBooNE doc-db 8622.

[23] Cross-section model and uncertainties, K. Duffy, S. Dytman, and S. Gardiner, MicroBooNE doc-db 27018.

[24] A.A. Aguilar-Arevalo et al. The Neutrino Flux prediction at MiniBooNE. *Phys. Rev. D*, 79:072002, 2009.

[25] Geant4 systematics: eventweight module validation, Kirsty Duffy, MicroBooNE doc-db 27561.

[26] Xiangpan Ji, Wenqiang Gu, Xin Qian, Hanyu Wei, and Chao Zhang. Combined Neyman–Pearson chi-square: An improved approximation to the Poisson-likelihood chi-square. *Nucl. Instrum. Meth. A*, 961:163677, 2020.

[27] T. Hauschild and M. Jentschel. Comparison of maximum likelihood estimation and chi-square statistics applied to counting experiments. *Nucl. Instrum. Meth.*, A457:384–401, 2001.

[28] Morris L Eaton. Multivariate statistics: a vector space approach. *John Wiley and Sons*, pages 116–117, 1983.

[29] New Method for Applying the ν_μ Constraint on the ν_e Cov-Matrix and Prediction, X. Qian, M. Toups, and M. Shaevitz, MicroBooNE doc-db 32672.

[30] J. Neyman and E. S. Pearson. On the problem of the most efficient tests of statistical hypotheses. *Phil. Trans. R. Soc. Lond.*, A 231:289, 1933.

[31] "Wire-Cell Far sideband opening proposal", J. H. Jo, MicroBooNE doc-db 33293.

[32] P. Abratenko et al. First Measurement of Inclusive Muon Neutrino Charged Current Differential Cross Sections on Argon at E_ν ~0.8 GeV with the MicroBooNE Detector. *Phys. Rev. Lett.*, 123(13):131801, 2019.

[33] P. Abratenko et al. Measurement of Differential Cross Sections for ν_μ-Ar Charged-Current Interactions with Protons and no Pions in the Final State with the MicroBooNE Detector. *Phys. Rev. D*, 102(11):112013, 2020.

[34] P. Abratenko et al. First Measurement of Differential Charged Current Quasielastic-like ν_μ-Argon Scattering Cross Sections with the MicroBooNE Detector. *Phys. Rev. Lett.*, 125(20):201803, 2020.

[35] K. Abe et al. Measurement of the ν_μ charged current quasielastic cross section on carbon with the T2K on-axis neutrino beam. *Phys. Rev. D*, 91(11):112002, 2015.

[36] Adjusting Neutrino Interaction Models and Evaluating Uncertainties using NOvA Near Detector Data. *Eur. Phys. J. C*, 80, 2020.

[37] Bootstrapping (statistics). `https://en.wikipedia.org/wiki/Bootstrapping_(statistics)`. Accessed: 2021-02-17.

[38] Glen Cowan, Kyle Cranmer, Eilam Gross, and Ofer Vitells. Asymptotic formulae for likelihood-based tests of new physics. *Eur. Phys. J. C*, 71:1554, 2011. [Erratum: Eur.Phys.J.C 73, 2501 (2013)].